Review—Mn^{4+}-Activated Red and Deep Red-Emitting Phosphors

Sadao Adachi ⓘ^{z}

Division of Electronics and Informatics, Faculty of Science and Technology, Gunma University, Kiryu-shi, Gunma 376-8515, Japan

Mn^{4+}-activated phosphors are a new class of non-rare earth phosphors and are alternative to commercial Eu^{2+}-activated nitride/oxynitride phosphors with growing interest in various applications. In this review article, the structural and photoluminescence (PL) properties of various Mn^{4+}-activated phosphors have been discussed. The host materials considered here can be roughly classified into five groups; fluorides, oxides, oxyfluorides, and two fluorine compounds. Phosphors of each group can also be classified into totally eleven subgroups from their different PL spectral features, e.g., whether an appearance of the zero-phonon line (ZPL) emission peak or not. The ZPL emission and absorption energies of the Mn^{4+} ions have been determined from the PL and PL excitation spectra using the Franck–Condon analysis method within the configurational-coordinate (CC) model. These results are used to obtain reliable phosphor parameters, i.e., the crystal-field (Dq) and Racah parameters (B and C), of the Mn^{4+} ions in the various host materials. The PL intensity vs temperature data, together with those of the luminescence lifetimes, are modeled on the basis of the CC model, and an excellent agreement has been achieved if not only the optical phonon but also the acoustic phonon contribution is taken into consideration in the conventional thermal quenching model. Effects of the hydrostatic pressure and dopant concentration on the PL spectral features are also discussed. Finally, key properties of the Mn^{4+}-activated phosphors are discussed for use of such red and deep red-emitting phosphor systems in warm w-LED and indoor plant cultivation applications.
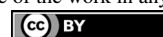
Over the past decade, white light-emitting diodes (w-LEDs) have been extensively employed because of their lifespan many times longer than equivalent incandescent lamp and significantly more efficient than most fluorescent lamps. However, the conventional w-LED devices with a yellow Y$_3$Al$_5$O$_{12}$ (YAG):Ce^{3+} phosphor excited by a blue InGaN chip suffer from a high correlated color temperature (CCT > 6000 K), and a low color-rendering index (CRI < 80) because of a lack of the red light component.

Addition of a red-emitting phosphor to such a cold w-LED device is a method to overcome its problem.[1,2] Searching for new red-emitting phosphors or those containing a red emission component has, therefore, become an important approach to the realization of warm w-LED applications. Apart from this, about 15 years ago the present author stated to investigate synthesis method of visible light-emitting porous Si layers on the Si(100) substrates by chemical etching in a HF solution with the addition of oxidizing agents, such as KIO$_3$,[3] I$_2$,[4] FeCl$_3$,[5] and H$_2$O$_2$,[6] under Xe lamp illumination (i.e., photochemical etching). The synthesized porous Si layers were in thin film with a few μm thickness and yellowish color. Such porous SI layers were emitted a broad-band orange light under UV excitation.[3–6]

Strangely, an oxidizing agent KMnO$_4$ produced only a yellowish fine particle, but not any thin porous Si film, on the Si(100) surface, regardless of Xe lamp illumination or not.[7] Photoluminescence (PL) measurements under UV excitation of such yellowish particles resulted in a very strong red emission with atomic-like spectrum. Subsequent chemical and X-ray diffraction (XRD) analyses suggested that such yellowish particles are Mn^{4+}-activated hexafluorosilicate salt, K$_2$SiF$_6$:Mn^{4+}, given by the following chemical reaction:[8,9]

$$6HF + 2KMnO_4 + (1-x)Si \rightarrow K_2(Si_{1-x}Mn_x)F_6 + (2-x)MnO_2$$
$$+ 3H_2O + \frac{1}{2}(2x+1)O_2 \qquad [1]$$
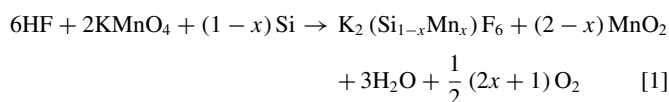
In Eq. 1, K$_2$(Si$_{1-x}$Mn$_x$)F$_6$ represents the K$_2$SiF$_6$:Mn^{4+} red-emitting phosphor. Some manganese oxides as the fate of surplus Mn were completely removed by rinsing in organic solvents.

The electronic configuration of Cr^{3+} ($3d^3$) is the same as that of Mn^{4+} and enables to emit red light when it was efficiently doped into some fluoride and oxide host materials.[10] From an analogy to K$_2$SiF$_6$:Mn^{4+} synthesis using KMnO$_4$ oxidation agent solution, we tried to synthesize Cr^{3+}-activated K$_2$SiF$_6$ phosphor by chemical etching of Si using a K$_2$Cr$_2$O$_7$ oxidation agent solution, but still have not yet succeeded at present. (Only a stain-etched Si layer emitting a broad yellow light at ∼ 1.9 eV was formed on the Si substrate immersed in the HF/K$_2$Cr$_2$O$_7$ mixed solution.) Ruby laser uses a synthetic ruby (Al$_2$O$_3$) doped with Cr^{3+}. Because of an extremely bright red emission from K$_2$SiF$_6$:Mn^{4+} phosphor, we also tried to fabricate K$_2$SiF$_6$:Mn^{4+} laser by optical pumping, but still have not yet succeeded at present. Instead of laser fabrication, however, we succeeded in a micronization of K$_2$SiF$_6$:Mn^{4+} powder by pulsed laser irradiation in liquid with its particle size from ∼ 110 μm to ∼ 2 μm.[11]

After publishing the above literature,[7,8] various Mn^{4+}-activated fluoride and oxide phosphors have been extensively investigated for developing a new phosphor material, a new synthesis method, deep understanding red-emitting phosphor properties, and applying to warm w-LEDs and others.[1,2] New Mn^{4+}-activated red-emitting phosphors based on "oxyfluoride" and "fluorine" compound hosts have also been demonstrated to meet the efficacy and color-quality targets of future warm w-LDE devices.

The purpose of this review article is to report the structural and PL properties of various Mn^{4+}-activated phosphors using the different host materials, such as fluorides, oxides, oxyfluorides, and some fluorine compounds like BaNb(OH)$_{1.5}$F$_{5.5}$ and NaHF$_2$. Key properties of the various Mn^{4+}-activated phosphors for use in research works and a variety of red and deep red-emitting phosphor applications are also discussed in this review article.

Theoretical Basis

Tanabe–Sugano energy-level diagram for Mn^{4+} ion.—Figure 1a shows the influence of the crystal field on the energy levels of the $3d^n$ system obtained based on the Tanabe–Sugano energy-level diagram.[12,13] The optical properties of some transition metal ions (Mn^{4+}, Cr^{3+}, V^{2+}, etc.) with $3d^3$ ($n = 3$) configuration have been investigated in terms of this type of energy-level diagram with considerable success. The parabolic bands in Fig. 1b are schematically shown based on the configurational-coordinate (CC) model with $^4A_{2g}$ as the ground state. The PL and PL excitation (PLE) spectra in Fig. 1c correspond to those for Mn^{4+}-activated "oxyfluoride" phosphors, Cs$_2$WO$_2$F$_4$:Mn^{4+} (left-hand side) and magnesium fluorogermanate (MFG):Mn^{4+} (right-hand side), obtained at room temperature (see Table V below). The readers can also find the same energy-level diagrams and schemes as
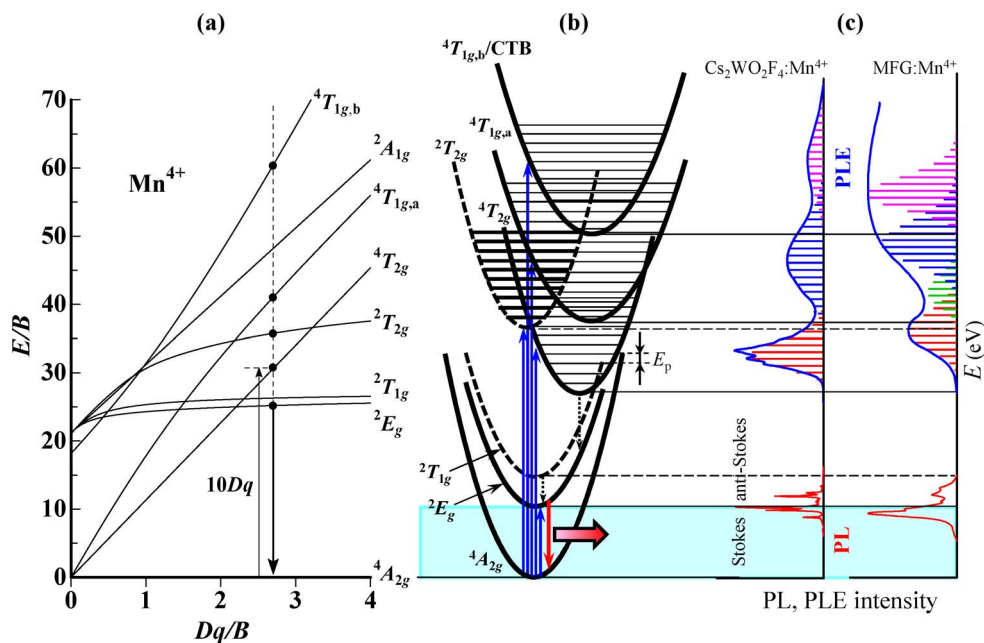
^{z}E-mail: adachi@gunma-u.ac.jp

Figure 1. (a) Tanabe–Sugano energy-level diagram for a $3d^3$ system in octahedral symmetry (Mn^{4+}). (b) CC model representing PL and PLE processes. (c) Schematic PL and PLE spectral features for the Mn^{4+}-activated oxyfluoride phosphors: $Cs_2WO_2F_6$:Mn^{4+} (type OF-A) and MFG:Mn^{4+} (type OF-B). The horizontal bars in the PLE spectra [(c)] represent the theoretical fits using Eq. 4.

in Fig. 1, but for the Mn^{4+}-activated "fluoride" and "oxide" phosphors in Fig. 1 of Refs. 1 and 2, respectively.

Various phosphors activated with Mn^{4+} ions show a series of relatively sharp emission lines or several broad emission bands in the red to deep red spectral region (at $\sim$600−750 nm; see, e.g., Fig. 4 below). Such sharp emission lines or broad emission bands are attributed to the Stokes and anti-Stokes $^2E_g \rightarrow {}^4A_{2g}$ transitions in Mn^{4+}. At low temperatures, only the Stokes $^2E_g \rightarrow {}^4A_{2g}$ emission lines or broad emission bands have been observed as relatively strong lines or bands. This is in direct contrast to the case of optical absorption or excitation transitions in the PLE spectra, where the anti-Stokes transition peaks have never been observed regardless of temperatures low or high (see, e.g., Figs. 2 and 3 below). Note that the $^4A_{2g} \leftrightarrow {}^2E_g$ transitions are both parity and spin forbidden, but gain their intensities with activation by the lattice vibrations and, as a result, become observable.[1,2]

Because the $^4A_{2g} \leftrightarrow {}^2T_{1g}$ emission and absorption transitions are both parity and spin forbidden, any clear $^2T_{1g}$-related optical transition peaks cannot be clearly observed in PL or PLE spectra of many Mn^{4+}-activated phosphors. In that case, the origin of the $^2T_{1g}$ state cannot be definitely determined from any optical spectra, but is inferred to lie at $\sim$ 0.1 eV above the ^2E_g origin.[1,2] Such an energy proximity relationship promised that the $^4A_{2g} \rightarrow {}^2T_{1g}$ absorption peak should nearly coincide in energy with the $^4A_{2g} \leftrightarrow {}^2E_g$ transition peaks, so the $^2E_g \rightarrow {}^4A_{2g}$ red emission intensity in the Mn^{4+}-activated phosphors can be enhanced by the $^4A_{2g} \rightarrow {}^2T_{1g}$ absorption transitions followed by an electron charge transfer from $^2T_{1g}$ to ^2E_g ($^2T_{1g} \rightarrow {}^2E_g$) (Fig. 1b).

The remarkably strong absorption band may come from the spin-allowed $^4A_{2g} \rightarrow {}^4T_{2g}$ excitation transitions (Fig. 1c). The subsequent higher-lying excitation transitions $^4A_{2g} \rightarrow {}^2T_{2g}$ are both parity and spin forbidden. A peak due to such parity- and spin-forbidden absorption transitions of $^4A_{2g} \rightarrow {}^2T_{2g}$ has not been clearly observed in many Mn^{4+}-activated fluoride phosphors.[1] In the oxide phosphors, however, the parity- and spin-forbidden $^4A_{2g} \rightarrow {}^2T_{2g}$ transitions have been sometimes observed in the spectral region between the $^4A_{2g} \rightarrow {}^4T_{2g}$ and $^4A_{2g} \rightarrow {}^4T_{1g,a}$ (^4P) transitions as a clear band or a bump in the lower energy part of the $^4A_{2g} \rightarrow {}^4T_{1g,a}$ excitation transition band tail.[2] As we will see later, the Mn^{4+}-activated oxyfluoride phosphors exhibit the optical properties of either "fluoride" or "oxide" phosphor type. The PLE spectra in Fig. 1c are representative of the "fluoride-

type" ($Cs_2WO_2F_4$:Mn^{4+}) and "oxide-type" oxyfluoride phosphors (MFG:Mn^{4+}).

At energies above the $^4A_{2g} \rightarrow {}^4T_{1g,a}$ transitions, another excitation transitions, such as $^4A_{2g} \rightarrow {}^2A_{1g}$, $^4A_{2g} \rightarrow {}^2T_{2g}$, $^4A_{2g} \rightarrow {}^2T_{1g}$, and $^4A_{2g} \rightarrow {}^4T_{1g,b}$ (^4P), occur in various phosphor materials.[12–14] A charge-transfer band (CTB) can also be observed in such higher energy region. As a result, one observes the PLE peak above the $^4A_{2g} \rightarrow {}^4T_{1g,a}$ transitions as a very broad absorption band with several kinks in the oxide and oxide-type oxyfluoride phosphors (see Figs. 4c−4f below). On the other hand, most of the fluoride and fluoride-type oxyfluoride phosphors show only a well-separated single, broad peak or band in this spectral region (< 5.5 eV; see PLE spectrum of $Cs_2WO_2F_4$:Mn^{4+} in Fig. 1c). Note that such higher-lying excitation states located above $^4T_{1g,a}$ are very hard to distinguish from each other and, therefore, we marked those excitation or absorption transition bands simply by $^4T_{1g,a}$ ($^4A_{2g} \rightarrow {}^4T_{1g,a}$) and $^4T_{1g,b}$/CTB ($^4A_{2g} \rightarrow {}^4T_{1g,b}$/CTB) in Fig. 1b. Such complex or multiple band structure has never been observed in any fluoride,[1] fluoride-type oxyfluoride, or fluorine compound phosphors (see PLE spectra in Figs. 4a, 4b, 4g, 4h, 4j, and 4k below).

PL and PLE spectral analysis based on the CC model.—*CC model.*—The Franck−Condon analysis with the CC model can be used to explain the optical properties of solids. Here, the optical energies of absorption and emission lines in the CC model can be written as[1,2,15–17]

$$h\nu_{ex} = E_{ZPL} + kh\nu_{p,ex} \qquad [2]$$

$$h\nu_{em} = E_{ZPL} - lh\nu_{p,em} \qquad [3]$$

where h is the Planck constant, $h\nu_{p,ex}$ and $h\nu_{p,em}$ are the lattice vibronic quanta for the excited and ground states, respectively, and k and l are positive integers. The experimental absorption and emission bands can be regarded as envelopes of numerous lines; each is due to a transition between one vibrational level, k, of the excited electronic state and one vibrational level, l, of the ground electronic state.

Some of the optical spectra have a vibrational oscillation structure that makes it very difficult or, in a case, easily to exactly determine the zero-phonon line (ZPL) energy. An expression for the spectral
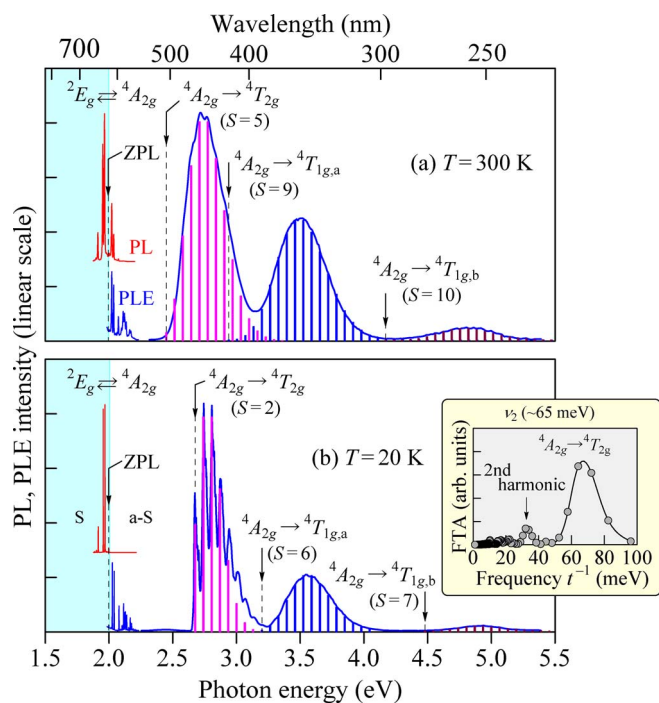
Figure 2. PL and PLE spectra for $K_2SiF_6:Mn^{4+}$ at (a) $T = 300$ K and (b) 20 K. The experimental data are taken from Ref. 9. The vertical bars in each PLE spectrum show the theoretical fits using Eq. 4 and $h\nu_{p,ex} = 65$ meV: (a) $E(^4T_{2g})_{ZPL} = 2.45$ eV ($S = 5$), $E(^4T_{1g,a})_{ZPL} = 2.94$ eV ($S = 9$), and $E(^4T_{1g,b})_{ZPL} = 4.17$ eV ($S = 10$); (b) $E(^4T_{2g})_{ZPL} = 2.68$ eV ($S = 2$), $E(^4T_{1g,a})_{ZPL} = 3.20$ eV ($S = 6$), and $E(^4T_{1g,b})_{ZPL} = 4.48$ eV ($S = 7$). The vertical arrows in each figure show the positions of $E(^2E_g)_{ZPL}$, $E(^4T_{2g})_{ZPL}$, $E(^4T_{1g,a})_{ZPL}$, and $E(^4T_{1g,b})_{ZPL}$. The inset in (b) represents FT amplitude (FTA) spectrum in the $^4A_{2g} \rightarrow ^4T_{2g}$ excitation transition region of the $K_2SiF_6:Mn^{4+}$ phosphor at 20 K. S = Stokes; a-S = anti-Stokes.
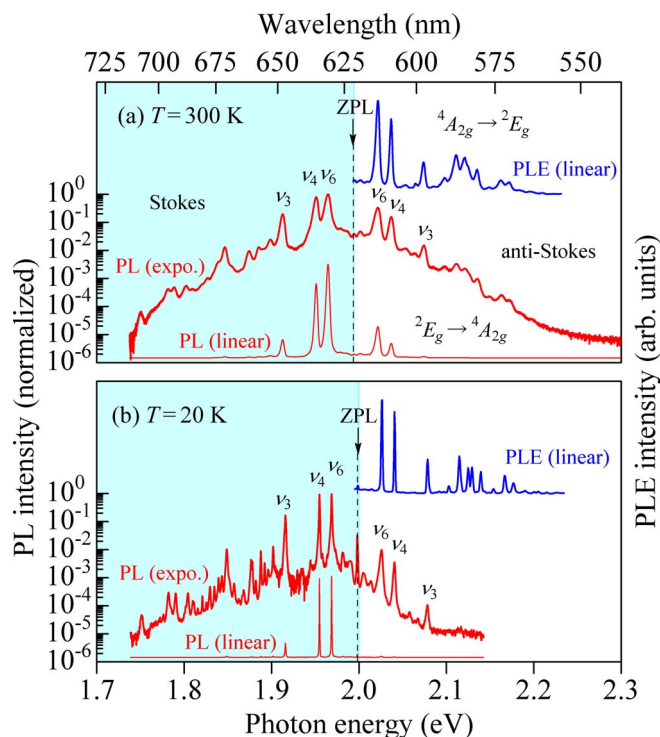

Figure 3. PL and PLE spectra of $K_2SiF_6:Mn^{4+}$ at (a) $T = 300$ K and (b) 20 K.[9]
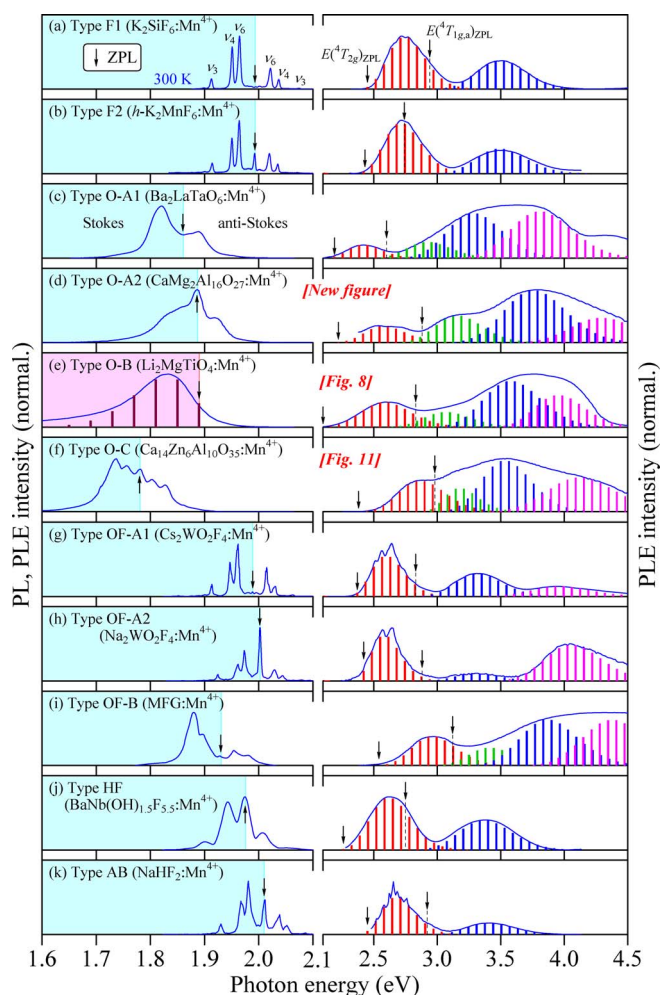

Figure 4. Representative PL and PLE spectra for the Mn^{4+}-activated phosphors measured at 300 K from different kinds of the host materials with exhibiting different PL spectral features: (a) type F1, (b) type F2 (F = fluoride), (c) type O-A1, (d) type O-A2, (e) type O-B, (f) type O-C (O = oxide), (g) type OF-A1, (h) type OF-A2, (i) type OF-B (OF = oxyfluoride), (j) type HF [HF = hydroxy fluoride ($BaNb(OH)_{1.5}F_{5.5}$)], and (k) type AB [AB = alkali bifluoride ($NaHF_2$)]. The experimental data are taken from Refs. 8, 20, 29−37. The vertical bars in each PLE spectrum show the theoretical fits using Eq. 4. The vertical arrows in each figure also show the positions of $E(^2E_g)_{ZPL}$ (PL), $E(^4T_{2g})_{ZPL}$, and $E(^4T_{1g,a})_{ZPL}$ (PLE). Some important parameters of these phosphors are listed in Tables II, IV, and V.

distribution of the excitation spectrum in the CC model is written as[1,2]

$$I_{PLE}(E) = \sum_n I_n^{ex}(n) \exp\left[-\frac{(E - E_{ZPL} - nh\nu_{p,ex})^2}{2\sigma_{ex}^2}\right] \quad [4]$$

with

$$I_n^{ex}(n) = I_0^{ex} \exp(-S)\frac{S^n}{n!} \quad [5]$$

where σ_{ex} is the broadening energy of each Gaussian component, I_0^{ex} is the ZPL intensity, and S is the mean local vibrational number (Huang−Rhys factor) defined by the Poisson statistics. The horizontal bars in Fig. 1c show the results calculated using Eq. 4 at the four different excitation absorption bands in the PLE spectrum.

An expression of the emission spectrum is given by almost the same form as Eq. 4:

$$I_{PL}(E) = \sum_n I_n^{em}(n) \exp\left[-\frac{(E - E_{ZPL} + nh\nu_{p,em})^2}{2\sigma_{em}^2}\right] \quad [6]$$

where $I_n^{em}(n)$ and σ_{em} have similar meanings as in Eq. 4. Equation 6 has explained the peculiar luminescence spectra observed in various semiconducting and insulating materials.[18–21]

Temperature dependence of optical spectra.—In principle, the temperature dependence of the PL intensity can be given by

$$I_{PL}(T) = c \sum_{i=3,4,6} \left| \langle \Psi_i | M_i | \Psi_f \rangle \right|^2 (E_{ZPL} \mp h\nu_i)^4 \left(n_i + \frac{1}{2} \pm \frac{1}{2} \right) \quad [7]$$

with

$$n_i = \frac{1}{\exp(h\nu_i / k_B T) - 1} \quad [8]$$

where c is a proportionality constant, $|<\Psi_i | M_i | \psi_f>|$ is an optical transition operator (Ψ_i = initial state; Ψ_f = final state; M_i = momentum matrix element), k_B is the Boltzmann constant, and ν_i is the lattice or local vibration frequency in a crystal or a complex with lattice vibronic mode i. The upper and lower signs in Eq. 7 correspond to the "Stokes" and "anti-Stokes" processes, respectively, and n_i is the Bose–Einstein occupation number given by Eq. 8.

Summation of the Stokes and anti-Stokes components in Eq. 7 simplifies

$$I_{PL}(T) = I_0 \left(1 + \frac{2}{\exp(h\bar{\nu}/k_B T) - 1} \right) \quad [9]$$

where $\bar{\nu}$ is the appropriately weight-averaged frequency of ν_i [in the case of fluoride (oxide) phosphors, Mn^{4+} ions are in the MnF_6^{2-} (MnO_6^{8-}) octahedron and thus $\nu_i = \nu_3$, ν_4, and ν_6; see "Vibration Frequencies of Mn^{4+} Ion in the Octahedron Molecule" below]. Here, values of $\bar{\nu}$ can be determined from the best-fit procedure with the experimental data. Introducing the conventional thermal quenching model into Eq. 9, we finally obtain an expression of $I_{PL}(T)$ by

$$I_{PL}(T) = \frac{I_0}{1 + \sum_i a_i \exp(-E_{qi}/k_B T)} \left(1 + \frac{2}{\exp(h\bar{\nu}/k_B T) - 1} \right) \quad [10]$$

where E_{qi} is the thermal quenching energy defined by each event i.

Racah and crystal-field splitting parameters.—*General model.*—The Racah parameters B and C can describe the effects of interelectronic repulsion. The sequence of the energy levels is then determined by the symmetry of ion sites, by the crystal-field strength $10Dq$, and by B and C. Determination of the crystal-field parameter Dq and some ZPL energies makes possible to estimate the Racah parameters B and C for Mn^{4+} ions in various host materials using the relation[22,23]

$$B = \frac{(\Delta E_T/Dq)^2 - 10(\Delta E_T/Dq)}{15(\Delta E_T/Dq - 8)} Dq \quad [11]$$

$$C \approx 0.328\Delta E_E - 2.59B + 0.59\frac{B^2}{Dq} \quad [12]$$

where ΔE_T is the difference in the ZPL energies of the $^4T_{1g,a}$ and $^4T_{2g}$ states and ΔE_E is the ZPL energy of the ^2E_g state. These quantities are given by

$$DE_T = E(^4A_{2g} \rightarrow {}^4T_{1g,a})_{ZPL} - E(^4A_{2g} \rightarrow {}^4T_{2g})_{ZPL}$$
$$= E(^4T_{1g,a})_{ZPL} - E(^4T_{2g})_{ZPL} \quad [13]$$

$$DE_E = E(^4E_g \rightarrow {}^4A_{2g})_{ZPL} = E(^2E_g)_{ZPL} - E(^4A_{2g})_{ZPL}$$
$$= E(^2E_g)_{ZPL} \quad [14]$$

with $E(^4A_{2g})_{ZPL}$ as a reference level (i.e., 0 eV). The crystal-field parameter Dq can also be written as

$$Dq = \frac{1}{10} E(^4A_{2g} \rightarrow {}^4T_{2g})_{ZPL} = \frac{1}{10} E(^4T_{2g})_{ZPL} \quad [15]$$

The $E(^4A_{2g} \rightarrow {}^4T_{2g})_{ZPL}$ and $E(^4A_{2g} \rightarrow {}^4T_{1g,a})_{ZPL}$ terms in Eq. 13 correspond to the first and second excitation bands usually observed at the peak wavelengths of ∼460 and ∼360 nm in various Mn^{4+}-activated fluoride phosphors, respectively.[1] The $E(^2E_g \rightarrow {}^4A_{2g})_{ZPL}$ term in Eq. 14 defines the ZPL energy of red emission (E_{ZPL} in Eqs. 3, 6, and 7). Such ZPL energies are known to depend on both the lattice temperature (Refs. 9 and 24; see also "Effects of Temperature on PL Spectral Feature" below) and pressure (Refs. 24 and 25; see also "Effects of Pressure on PL Spectral Feature" below).

Advanced model for Racah parameter determination.—It should be noted that the ZPL energy of the ^2E_g state can be relatively easily determined from experimental PL spectra. However, those of the higher-lying excited states like $^4T_{2g}$, $^4T_{1g,a}$, and $^4T_{1g,b}$ are very difficult to exactly determine from experimental PLE spectra. The main reason for this is due to the complex nature in such excitation spectral region. Therefore, a peak energy of each excitation band was previously regarded simply as its "ZPL" energy.[26] Then, ΔE_T in Eq. 13 can be written as

$$\Delta E_T = E(^4T_{1g,a})_{ZPL} - E(^4T_{2g})_{ZPL} \sim \overline{E}(^4T_{1g,a}) - \overline{E}(^4T_{2g}) \quad [16]$$

where $\Delta\overline{E}(^4T_{2g})$ and $\Delta\overline{E}(^4T_{1g,a})$ represent the peak energies of the $^4A_{2g} \rightarrow {}^4T_{2g}$ and $^4A_{2g} \rightarrow {}^4T_{1g,a}$ excitation transition bands, respectively. The above and $^4A_{2g} \rightarrow {}^4T_{1g,b}$ transition energies can be written approximately as

$$\overline{E}(^4T_{2g}) \sim E(^4T_{2g})_{ZPL} + S_1 h\nu_{p,ex} \quad [17]$$

$$\overline{E}(^4T_{1g,a}) \sim E(^4T_{1g,a})_{ZPL} + S_2 h\nu_{p,ex} \quad [18]$$

$$\overline{E}(^4T_{1g,b}) \sim E(^4T_{1g,b})_{ZPL} + S_3 h\nu_{p,ex} \quad [19]$$

with S_i given in Eq. 5. Equations 17−19 give good approximations in obtaining peak energy of each excitation band from its ZPL energy, or vice versa, in estimating ZPL energy from its peak energy of each excitation transition band.[2]

Let us consider an error in the crystal-field and Racah parameter determinations using $\Delta\overline{E}(^4T_{2g})$ and $\Delta\overline{E}(^4T_{1g,a})$, instead of using $E(^4T_{2g})_{ZPL}$ and $E(^4T_{1g,a})_{ZPL}$. Introducing Eq. 17 into Eq. 15, we obtain

$$Dq \sim \frac{1}{10} \overline{E}(^4T_{2g}) \sim \frac{1}{10} E(^4T_{2g})_{ZPL} - \frac{1}{10} S_1 h\nu_{p,ex} \quad [20]$$

An error in this expression gives $\delta Dq \sim (1/10)S_1 h\nu_{p,ex} \sim 52 S_1$ cm^{-1} with $h\nu_{p,ex} \sim 65$ meV. Dominant errors in determining B (Eq. 11) and C (Eq. 12) come from ΔE_T and Dq, respectively. Introducing Eqs. 17 and 18 into Eq. 13, we obtain

$$\Delta E_T \sim \overline{E}(^4T_{1g,a}) - \overline{E}(^4T_{2g}) \sim \left[E(^4T_{1g,a})_{ZPL} - E(^4T_{2g})_{ZPL} \right]$$
$$- (S_1 - S_2) h\nu_{p,ex} \quad [21]$$

An error of ΔE_T can then be given by $\delta\Delta E_T = (S_1 - S_2)h\nu_{p,ex}$.

The Racah parameters B and C are calculated using Eqs. 11 and 12. We must note, however, that the spin-forbidden $^4A_{2g} \rightarrow {}^2T_{2g}$ transitions take place at energies near or below the $^4A_{2g} \rightarrow {}^4T_{1g,a}$ [$E(^4T_{1g,a})_{ZPL}$] transitions (see, e.g., Fig. 1c). The intensities of these forbidden transitions in various Mn^{4+}-activated fluoride phosphors (Ref. 1) were observed to be much weaker than those in the oxide phosphors (Ref. 2) From an analogy to the oxide phosphors, we can also expect an overlap of the spin-forbidden $^4A_{2g} \rightarrow {}^2T_{2g}$ component with the $^4A_{2g} \rightarrow {}^4T_{2g}$ and $^4A_{2g} \rightarrow {}^4T_{1g,a}$ components even in the various fluoride phosphors. The $^4A_{2g} \rightarrow {}^4T_{1g,a}$ [$E(^4T_{1g,a})_{ZPL}$] energies in the oxide phosphors can, therefore, be more exactly determined by considering not only the $E(^4T_{2g})_{ZPL}$- and $E(^4T_{1g,a})_{ZPL}$-related components but also the parity- and spin-forbidden $E(^2T_{2g})_{ZPL}$ component (see its contribution represented by the green horizontal or vertical bars in Figs. 1c, 4c−4f, etc.).

In the fluoride phosphors, it is very difficult to reasonably separate the $E(^4T_{1g,a})_{ZPL}$ component from the $E(^2T_{2g})_{ZPL}$ one by the conventional best-fit procedure as used in the oxide phosphors. Therefore, we must carry out a correction of the $E(^2T_{2g})_{ZPL}$ transition component in

the ZPL energy determination of the $^4A_{2g} \rightarrow {}^4T_{1g,a}$ [$E(^4T_{1g,a})_{ZPL}$] transitions for the fluoride phosphors in the following manner and using a value of $E(^4T_{1g,a})_{ZPL,m}$, instead of $E(^4T_{1g,a})_{ZPL}$, in the Racah parameter determination from Eqs. 11 and 12:

$$E(^4T_{1g,a})_{ZPL,m} = E(^4T_{1g,a})_{ZPL} + mh\nu_{p,ex} \qquad [22]$$

The index value m used in Eq. 22 is 4 for I$_x$−IV$_y$−F$_{x+4y}$ ($x = 2$, $y = 1$) "fluoride" phosphors (K$_2$SiF$_6$:Mn^{4+}, Cs$_2$GeF$_6$:Mn^{4+}, etc.), otherwise 5 (Table II). The reason for the smaller m (= 4) value in the former phosphors comes from the fact that the MnF$_6^{2-}$ octahedron in this type of phosphors is more highly symmetric and/or lowly distorted than those in the other phosphors like KTeF$_5$:Mn^{4+} [I$_x$−IV$_y$−F$_{x+4y}$ ($x = 1$, $y = 1$); see Table II] and Cs$_2$KAlF$_6$:Mn^{4+} [I$_x$−III$_y$−F$_{x+3y}$ ($x = 3$, $y = 1$); see Table II].[1] In the present article, the best-fit analyses of the PLE spectra for the oxide phosphors were performed with properly taking into account the effects of the parity- and spin-forbidden $^4A_{2g} \rightarrow {}^2T_{2g}$ transition contribution (see its contribution represented by the green horizontal bars in Fig. 1c). Such fit-determined $E(^4T_{1g,a})_{ZPL}$ values were then inserted into Eqs. 11 and 12 in the Racah parameter determination of the oxide phosphors (i.e., $m = 0$ in Eq. 22). For the "oxyfluoride" phosphors, a group of the fluoride-type phosphors were regarded as the fluoride ones and therefore we put $m = 5$ into Eq. 22, whereas a group of the oxide-type phosphors were regarded as the oxide ones and therefore we put $m = 0$ into Eq. 22.

Representative Red-Emitting Phosphor Properties: K$_2$SiF$_6$:Mn^{4+}

K$_2$SiF$_6$:Mn^{4+} is a representative phosphor system for better understanding the Mn^{4+}-activated phosphor properties in the red spectral region.[8,9] Figure 2a shows the PL and PLE spectra of K$_2$SiF$_6$:Mn^{4+} in the 1.5−5.5 eV spectral region measured at $T = 300$ K.[9] The PLE spectrum in Fig. 2a exhibits the three broad excitation bands peaking at ∼ 2.7, ∼ 3.5, and ∼ 4.8 eV, together with several sharp excitation lines at energies very close to the red emission peaks at ∼ 2.0 eV. The ZPL energies of the higher-lying absorption bands, $^4A_{2g} \rightarrow {}^4T_{2g}$, $^4A_{2g} \rightarrow {}^4T_{1g,a}$, and $^4A_{2g} \rightarrow {}^4T_{1g,b}$, are marked by the vertical arrows in Fig. 2a. These higher-lying absorption bands correspond to the anti-Stokes transitions, i.e., those observed at transition energies higher than their ZPL energies. In the $^4A_{2g} \leftrightarrow {}^2E_g$ transition region, an almost mirror image relationship can be found between the Stokes and anti-Stokes PL transitions and also a mirror image relationship between the Stokes PL and anti-Stokes PLE transitions.

Figure 2b shows the same results as in Fig. 2a, but at $T = 20$ K.[9] The low-temperature PL spectrum reveals very sharp emission lines on the Stokes spectral region; however, no remarkable PL peaks can be found in the anti-Stokes spectral region. A unique feature is also observed in the PLE spectrum at 20 K. This is an appearance of the multiple-peak structure in the first excitation band of $^4A_{2g} \rightarrow {}^4T_{2g}$. Such multiple-peak structure has never been observed in the second or other higher-lying excitation transition bands like $^4A_{2g} \rightarrow {}^4T_{1g,a}$, and $^4A_{2g} \rightarrow {}^4T_{1g,b}$.[1] The multiple-peak energy separation is about 65 meV. We also note that any multiple PLE peak structure has never been observed in all the Mn^{4+}-activated oxide phosphors at any kind of the excitation bands with any temperatures from cryogenic to higher than 300 K.[2]

The inset in Fig. 2b shows Fourier transform (FT) spectrum obtained using the Hamming window function for the PLE spectrum with a peak at ∼2.7 eV ($^4A_{2g} \rightarrow {}^4T_{2g}$; $T = 20$ K).[9] The FT analysis was performed by integrating Eq. 5 of Ref. 9 from $T_1 = 2.65$ eV to $T_2 = 3.20$ eV. The FT amplitude spectrum was plotted against $1/t$, i.e., in units of energy. We can see a peak at $1/t \sim 65$ meV, in agreement with the energy separation of $\nu_2 \sim 65$ meV observed in Fig. 2b. The peak at $1/t \sim 33$ meV is the second harmonic of the main peak at ∼ 65 meV. The FT analysis indicates that the clear multiple peaks observed in the $^4A_{2g} \rightarrow {}^4T_{2g}$ transition region are produced by the ν_2-assisted excitation process in the MnF$_6^{2-}$ octahedron. A Jahn − Teller effect in the $^4T_{2g}$ state is the major source of the intensity of the observed ν_2 progressions.[27,28]

Figure 3 shows the exponential and linear-scale PL spectra of the K$_2$SiF$_6$:Mn^{4+} phosphor in the $^4A_{2g} \rightarrow {}^2E_g$ transition region at (a) $T = 300$ and (b) 20 K.[9] The PLE spectra observed in this spectral region are also shown in Fig. 3. Each PL (PLE) peak corresponds to that activated by the local vibronic modes (ν_i) of the MnF$_6^{2-}$ octahedron in K$_2$SiF$_6$. Many vibronic combination modes of the internal vibrations like $\nu_3 + \nu_6$ and $\nu_3 + \nu_4$ have also been clearly observed at 300 K with energies lower (Stokes) and higher than the ν_3 sideband (anti-Stokes) emission line in Fig. 3 (see details in Ref. 8). Because of the extremely weak nature, the anti-Stokes peaks can be not clearly identified on the linear PL spectra at 20 K in Figs. 2b and 3b. This is because the PL intensity of the anti-Stokes sideband peak is simply proportional to the phonon occupation number n_i ($T \rightarrow 0$ K, $n_i \rightarrow 0$), but that of the Stoke sideband peak is proportional to ($n_i + 1$) (see Eq. 7).

Interestingly, the Stokes and anti-Stokes PL peak intensities in the vibronic combination regions [< 1.9 eV (Stokes) and > 2.1 eV (anti-Stokes)] are very weak, but the anti-Stokes PLE intensities are very strong (see PLE spectra in Fig. 3). The relatively strong anti-Stoke PLE peaks at such vibronic combination region of > 2.1 eV can also be clearly observed in the linear plots of Fig. 2. The general quantum theory promises that higher perturbation process may have lower transition probability. Evidently, the "vibronic combination" process is higher perturbation process than the "single-phonon" process of ν_3, ν_4, ν_6, or others. Thus, the results in Figs. 2 and 3 are inconsistent with this simple quantum-mechanical consideration. Further study needs to make clear this problem.

Classification of Mn^{4+}-Activated Phosphors from Different PL Spectral Features

Firstly, we classify the various Mn^{4+}-activated phosphors ever-reported from an aspect of different kinds of the host materials into five groups: (i) fluorides, (ii) oxides, (iii) oxyfluorides, (iv) hydroxy fluoride, and (v) alkali bifluoride. From different PL spectral features, we can also classify such five phosphor groups into eleven subgroups: (a) type F1, (b) type F2 (F = fluoride), (c) type O-A1, (d) type O-A2, (e) type O-B, (f) type O-C (O = oxide), (g) type OF-A1, (h) type OF-A2, (i) type OF-B (OF = oxyfluoride), (j) type HF [HF = hydroxy fluoride (BaNb(OH)$_{1.5}$F$_{5.5}$)], and (k) type AB [AB = alkali bifluoride (NaHF$_2$)]. The representative PL and PLE spectra for such different Mn^{4+}-activated subgroup phosphors are shown in Figs. 4a–4k in accord with the above-mentioned classification scheme. These PL and PLE spectra are taken from Refs. 8, 20, and 29−37. The corresponding enlarged PL spectra are also shown in Figs. 5a–5k.

Types F, O, and OF phosphors have been synthesized with the host materials of fluoride, oxide, and oxyfluoride compounds, respectively. The difference in types F1 and F2 of fluoride phosphors comes from whether the ZPL emission peak cannot be easily observed (F1; Figs. 4a and 5a) or clearly observed in PL spectrum at room temperature (F2; Figs. 4b and 5b). Almost all the oxide phosphors activated with Mn^{4+} ions include germinate, silicate, aluminate, titanate, perovskite, double perovskite phosphors, and so on. Such oxide phosphors have been classified into three independent subgroups, namely, types O-A, O-B, and O-C, from those of the different PL spectral features (see detailed classification scheme for types A, B, and C in Ref. 2).

Phosphors of type O-A promise to observe PL spectra with clearly resolved Stokes and anti-Stokes components on the lower and higher photon-energy sides of the ZPL emission peak, respectively, caused by the $^2E_g \rightarrow {}^4A_{2g}$ transitions in Mn^{4+} (Figs. 4c and 4d). This fact makes easy to identify the ZPL peak position from the measured PL spectra at room and/or cryogenic temperatures. Like types F1 and F2 phosphors, the difference in types O-A1 and O-A2 phosphors comes from whether the ZPL emission peak cannot be easily observed (type O-A1; Figs. 4c and 5c) or clearly observed in PL spectrum at room temperature (type O-A2; Figs. 4d and 5d).

The second subgroup, called type O-B phosphor, in the Mn^{4+}-activated oxide phosphors is that exhibiting no clear fine peak structure in a PL spectrum caused by the ZPL emission and/or its sideband
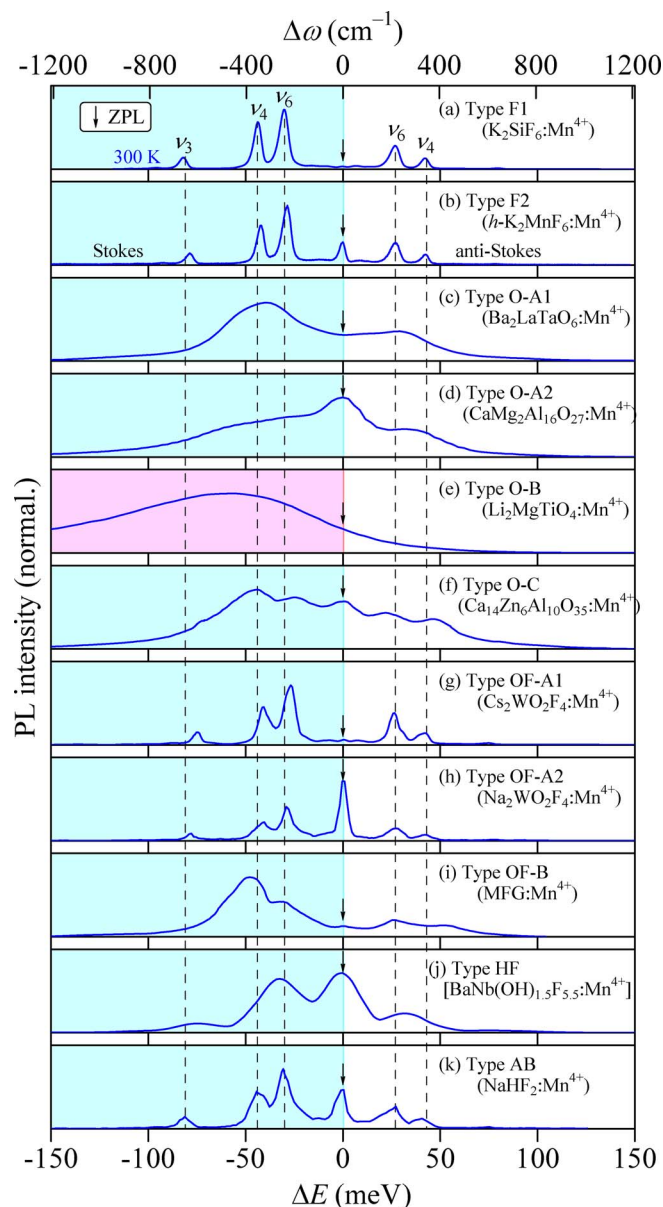
Figure 5. The same as in Fig. 4, but those only for the PL spectra were plotted against the difference in energy from each ZPL emission peak (vertical arrow).

peaks. As a result, its PL spectrum can be characterized only by a single broad emission band, which is usually asymmetric with emission intensity decreasing more steeply on the higher photon-energy side (Figs. 4e and 5e). Because of such unique PL spectral feature of type O-B phosphor, it is very hard or impossible to estimate an exact ZPL emission energy in this type of oxide phosphors. Therefore, we assume that the PL spectral feature can be characterized by the Franck−Condon model of Eq. 6. The vertical bars in the PL spectrum of Fig. 4e show such Franck−Condon model analysis using Eq. 6 with assuming an energy of $h\nu_{p,em} \sim 40$ meV. The ZPL energy, $E_{ZPL} = E(^2E_g)_{ZPL} \sim 1.890$ eV, obtained for this analysis is marked by the vertical arrows in Figs. 4e and 5e.

The third subgroup, called type O-C phosphor, is that exhibits a multiple-peak (or a multiple-step) structure in a PL spectrum with intensity tail along the higher photon-energy side (Figs. 4f and 5f). Unfortunately, no any PL measurement at a cryogenic temperature on a type O-C phosphor has been performed until recently. This fact makes impossible or very difficult to identify the ZPL emission energy in this type of phosphors.[2] However, recent PL measurements by Qin

et al.[38] (Wu et al.[39]) from $T = 10$ K (80 K) to higher temperatures than 300 K made possible which peak comes from or is the origin of the ZPL emission transitions (see Fig. 18i below).

The oxyfluoride phosphors can be classified into two subgroups, types OF-A and OF-B. The former phosphor promises to observe PL spectrum that is resemble of type F1 or F2 fluoride phosphor, whereas the latter one gives that is of O-A1 or O-A2 subgroup phosphor (type O-A phosphor). It should be noted that type OF-A phosphor, which is of the fluoride type, can be characterized by the well-resolved ZPL emission peak with a series of several sharp vibronic sideband peaks rather than a broad PL band. On the contrarily, type OF-B phosphor, which is of the oxide type rather than of the fluoride type, can provide a broad PL band rather than a series of the sharp emission peaks (see Figs. 4g–4i, 5g–5i; see also Fig. 1c). The difference in types OF-A1 and OF-A2 comes from whether the ZPL emission peak cannot be easily observed (type OF-A1; see Figs. 4g and 5g) or clearly observed in PL spectrum when measured at room temperature (type OF-A2; see Figs. 4h and 5h).

The luminescence properties of BaNb(OH)$_{1.5}$F$_{5.5}$:Mn^{4+} (type HF) and NaHF$_2$:Mn^{4+} phosphors (type AB) in Figs. 4 and 5 resemble those of the fluoride phosphors rather than of the oxide ones. Thus, the PL spectra from such phosphors can be characterized by a sharp ZPL emission peak with a series of its sharp vibronic sidebands. Such PL spectral feature can be easily recognized in Figs. 4k and 5k (NaHF$_2$:Mn^{4+}).

As briefly mentioned before, the PLE spectral feature in the spectral region below ~ 4 eV of the fluoride type can be fitted only by the well-resolved and nearly symmetric excitation transition bands, namely, the $^4A_{2g} \rightarrow {}^4T_{2g}$ and $^4A_{2g} \rightarrow {}^4T_{1g,a}$ transition bands (Fig. 4a). On the other hand, those of the oxide type require the additional spin-forbidden transition band, $A_{2g,b} \rightarrow {}^2T_{2g}$, between the lowest ($^4A_{2g} \rightarrow {}^4T_{2g}$) and second lowest ($^4A_{2g} \rightarrow {}^4T_{1g,a}$) spin-allowed excitation transition bands (Figs. 4c–4f). Since phosphors of OF-Al, OF-A2, HF, and AB types fall in a type of the fluoride phosphors, their PLE spectra can be fitted by considering only the two broad excitation transition bands, $^4A_{2g} \rightarrow {}^4T_{2g}$ and $^4A_{2g} \rightarrow {}^4T_{1g,a}$, in the spectral region below ~ 4 eV (Figs. 4g, 4h, 4j, and 4k).

It should be noted that a sharp multiple-peak structure caused by the Poisson statistics in Eq. 4 is clearly observed only for the fluoride phosphors and at cryogenic temperatures, but not at room temperature (Fig. 2). Thus, some oscillatory structures in the PLE spectra at room temperature of Figs. 4g, 4h, and 4k are understood to be exogenously produced by a Xe-lamp excitation source used in such PLE experiments.[1,2]

Vibration Frequencies of Mn^{4+} Ion in the Octahedron Molecule

Luminescence from Mn^{4+} ions could be activated only in the octahedral site of the host lattice. An octahedron molecule like MnF$_6$ (MnF$_6^{2-}$) or MnO$_6$ (MnO$_6^{8-}$) has $3N - 6 = 15$ ($N = 7$) normal vibronic modes with six coordinates required to describe the translational and rotational motions, and its crystallographic symmetry properties promise having six independent frequency modes ν_i from $i = 1$ to 6.[40,41] In Table I, we summarize the 300-K local vibration frequencies of the MnF$_6^{2-}$ and MnO$_6^{8-}$ octahedron molecules observed in phosphors of fluoride, oxide, and oxyfluoride hosts. These frequencies are taken from Fig. 5 (ν_3, ν_4, and ν_6) and Ref. 2 (ν_1, ν_2, and ν_5).

The IR-active (ν_3 and ν_4) and silent vibration frequencies (ν_6) can in principle be determined from analyzing PL spectra, whereas the Raman-active ν_1, ν_2, and ν_5 frequencies are obtained from Raman scattering measurements. The PL spectra for all types of the Mn^{4+}-activated phosphors discussed in "Classification of Mn^{4+}-Activated Phosphors from Different Luminescence Properties" are plotted in Fig. 5 against the differences in energy from the ZPL emission peak [ΔE in meV (lower axis) and $\Delta \omega$ in cm^{-1} (upper axis)].[8,20,29–37] As expected, the Stokes νi ($i = 3$, 4, and 6) energies are almost the same as the anti-Stokes ones. It is understood from Fig. 5 that the local vibronic energies of ν_i are not so largely dependent on a kind of the host lattice materials, i.e., types of O-F. O-A, O-B, O-C, OF-A, OF-B,

Table I. Vibronic frequencies of MnF_6^{2-} and MnO_6^{8-} molecules in fluoride, oxide, oxyfluoride, and other host materials at 300 K. R = Raman active; IR = infrared active. (1 eV = 8068 cm^{-1}).

Mode	Polarization	Motion	Activity	Frequency (cm^{-1})
ν_1	a_{1g}	Stretch	R	600[*1]
ν_2	e_{1g}	Stretch	R	510[*1]
ν_3	t_{1u}	Stretch	IR	655[*2]
ν_4	t_{1u}	Bend	IR	355[*2]
ν_5	t_{2g}	Bend	R	305[*1]
ν_6	t_{2u}	Bend	Silent	240[*2]

[*1]See Fig. 5.
[*2]See Ref. 2.

HF, and AB. The dashed lines on the left-hand side of Fig. 5 indicate their Stokes ν_3, ν_4, and ν_6 frequencies listed in Table I.

Figure 6 shows our measured Raman spectra in the $(NH_4)_2MF_6$:Mn^{4+} phosphors with M = Si, Ge, Sn, and Ti at 300 K.[42] A pair of ν_1, ν_2, or ν_5 peak can, in principle, be observed in the Raman spectra. For example, we can find two ν_1 peaks at ~ 650 and ~ 595 cm^{-1} in $(NH_4)_2SiF_6$:Mn^{4+} of Fig. 6a. The former and latter peaks correspond to the ν_1 vibronic mode of the SiF_6^{2-} and MnF_6^{2-} octahedrons in the $(NH_4)_2SiF_6$ host, respectively. In Fig. 6, the vibration frequencies of the metal complex MF_6^{2-} is strongly dependent on a kind of M (Si, Ge, Sn, or Ti). On the other hand, those of the local metal complex MnF_6^{2-} in the $(NH_4)_2MF_6$ host (Fig. 6) exhibit no remarkable dependence on a kind of the surrounding metal species M. This is because the Mn^{4+} ion in the MnF_6^{2-} octahedron feels a bond force, i.e., a spring constant, from the surrounding metal species M as it acts as a weak perturbation in the lattice dynamic process. Therefore, the vibration frequencies of the local MnF_6^{2-} octahedron are not so strongly dependent on a kind of the surrounding metal species M, as has been clearly observed in Fig. 6.

The multiple-peak structure in the PLE spectra for the Mn^{4+}-activated fluoride phosphors have been well explained by inserting an energy of $h\nu_{p,ex} \sim 65$ meV into Eq. 4 (Fig. 2b). As evidenced from Table I, this energy corresponds to the ν_2 "gerade" frequency of the MnF_6 (MnF_6^{2-}) octahedron very well. Unfortunately, such a sharp vibronic-related PLE peak structure has been observed only in the flu-

oride phosphors. Therefore, there has been no reliable $h\nu_{p,ex}$ values that can be used in the PLE analyses of the oxide, oxyfluoride, and other Mn^{4+}-activated phosphors. Therefore, we used the same vibration energies of $h\nu_{p,ex} \sim h\nu_2 \sim 65$ meV (~ 525 cm^{-1}) not only in the fluoride phosphors but also in other phosphors. This assumption can be justified from considering a simple linear chain model with a two-point basis (see Figs. 4.13 and 4.14 in Ref. 43) and the fact that the "oxygen" mass number (m_O) relative to the "manganese" mass number (m_{Mn}), m_O/m_{Mn}, is nearly the same as that of the "fluorine" mass number (m_F), m_F/m_{Mn} (i.e., $m_O/m_{Mn} \sim m_F/m_{Mn} \sim 0.3$). These lead to no strong dependence of ν_2 frequency among the different host materials.

In the PL spectral analysis using the Poisson statics model in Fig. 4e, we introduced a value of $h\nu_{p,em} \sim 40$ meV (~ 320 cm^{-1}) into Eq. 6. This value is obtained from

$$\nu_{p,em} = \frac{\sum_{i=3,4,6} I_{PL,i}\nu_i}{\sum_{i=3,4,6} I_{PL,i}} \qquad [23]$$

where $I_{PL,i}$ represents the PL intensity of the Stokes ν_i emission. Thus, $\nu_{p,em}$ is regarded as the vibration frequency averaged with the ν_i-mode PL intensities of the octahedral Mn^{4+} ions. Calculation of Eq. 23 promised obtaining a value of $h\nu_{p,em} \sim 35-45$ meV for almost all the Mn^{4+}-activated phosphors and a value of ~ 40 meV for K_2SiF_6:Mn^{4+} from the PL spectrum given in Fig. 5a. For simplicity, we used a constant value of $h\nu_{p,em} \sim 40$ meV in the PL spectral analysis of type O-B phosphors (see Fig. 17 below).

Room-Temperature PL Spectral Feature

Fluoride phosphors.—The difference in the room-temperature PL spectral feature of types F1 and F2 subgroup phosphors comes whether the ZPL emission peak can be clearly observed (type F1) or not (type F2). Table II summarizes the crystal structure and several important phosphor parameters of the Mn^{4+}-activated fluoride phosphors with types F1 and F2. Table III also summarizes the representative examples of type F1 and F2 phosphors belonging to the different crystal symmetry and chemical formula with the different crystal class and space group.

The ZPL emission intensity is sensitively dependent on the local symmetry of the environment of the Mn^{4+} ions in the host crystal. Similarly, the piezoelectric and optical rotation activities in the crystal are strongly dependent on the local symmetry of the host ions. In our earlier work on some Mn^{4+}-activated hexafluorometallate phosphors,[44] therefore, we considered that any piezoelectric or strain-related effect, such as a longitudinal electric field induced by piezo-electrically active phonons and/or q-dependent Fröhlich interaction, may activate the ZPL emission in phosphors of low crystal symmetry. Further work,[45] however, confirmed that the ZPL emission peak can be clearly observed at room temperature, regardless of whether the host crystal is in a symmetry of the piezoelectric active or not. A good example is the phosphor crystallizing in the cubic symmetry. In Table III, $(NH_4)_3AlF_6$:Mn^{4+} crystallizes in the piezoelectrically active space group of cubic $F\bar{4}3m$, but shows no strong ZPL emission at room temperature; conversely, K_3ZrF_7:Mn^{4+} crystallizes in the piezoelectrically inactive space group of cubic $Fm\bar{3}m$, but shows relatively strong ZPL emission at room temperature. Moreover, K_2NaAlF_6:Mn^{4+} and K_2SiF_6:Mn^{4+} crystallize in the piezoelectrically active space group of cubic $Fm\bar{3}m$, but the former (latter) shows relatively strong (not strong) ZPL emission. Thus, it is evident that strong correlation cannot be found between the ZPL emission intensity and crystal symmetry of the host lattice whether it is piezoelectrically and optical rotation active or not. Briefly summarizing Table III, we can say that the fluoride phosphors in the hexagonal, orthorhombic, and monoclinic structures promise to give the relatively strong ZPL emission at room temperature (type F2); however, those in the cubic, trigonal, and tetragonal structures show in any case no or, more rigorously saying, negligibly small ZPL emission intensity (type F1).
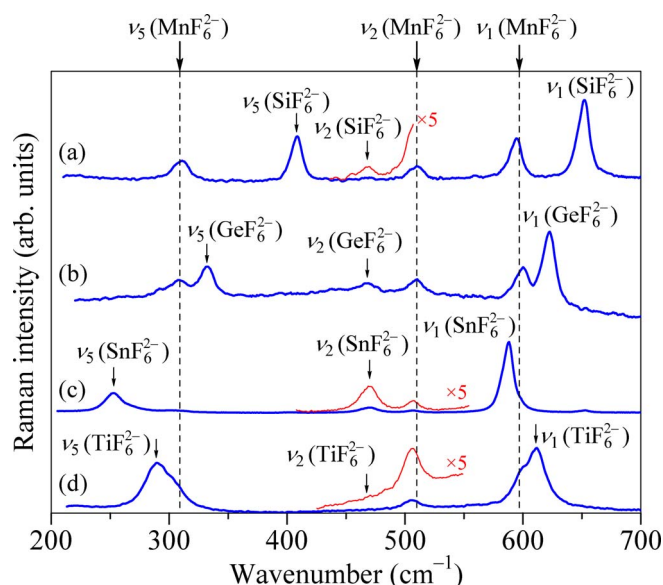

Figure 6. Raman spectra observed in the Mn^{4+}-activated $(NH_4)_2MF_6$ phosphors with (a) M = Si, (b) Ge, (c) Sn, and (d) Ti at 300 K.[42]

Table IIa. Summary of crystal class (CC), space group (SG), phosphor type (F1 or F2), ZPL emission energy [$^2E_g = E(^2E_g)_{ZPL}$], ZPL excitation absorption energies [$^4T_{2g} = E(^4T_{2g})_{ZPL}$; $^4T_{1g,a} = E(^4T_{1g,a})_{ZPL}$], crystal-field parameter (Dq), and Racah parameters (B and C) at 300 K for some Mn^{4+}-activated fluoride phosphors. The Racah parameters were calculated using Eqs. 11 and 12 with introducing values of $E(^4T_{1g,a})_{ZPL,m}$ into Eq. 22 instead of $E(^4T_{1g,a})_{ZPL}$. c = cubic; tr = trigonal; h = hexagonal; o = orthorhombic; m = monoclinic; t = tetragonal. (1 eV = 8068 cm^{-1}).

System	Formula	Fluoride host	CC	SG	Type	^2E_g (eV)	$^4T_{2g}$ (eV)	$^4T_{1g,a}$ (eV)	Dq (cm^{-1})	B (cm^{-1})	C (cm^{-1})	Ref.
$I_x-II_y-F_{x+2y}$	I–II–F$_3$	KZnF$_3$	c	$Pm\bar{3}m$ (221)	F1	1.987	2.45	2.83	1975	525	3975	46
$I_x-II_y-III_z-F_{x+2y+3z}$	I–II–III–F$_6$	LiSrAlF$_6$	tr	$P\bar{3}1c$ (163)	F2	2.003	2.50	2.89	2015	535	4000	212
		LiSrGaF$_6$	tr	$P\bar{3}1c$ (163)	F2	2.007	2.43	2.80	1960	520	4050	54
$I_x-III_y-F_{x+3y}$	I–III–F$_4$	NaYF$_4$	h	$P\bar{6}$ (174)	F2	2.007	2.45	2.91	1975	600	3870	55
		NaGdF$_4$	h	$P\bar{6}$ (174)	F2	2.007	2.50	2.86	2015	515	4060	55
	I$_2$–III–F$_5$	K$_2$AlF$_5$·H$_2$O	o	$Cmcm$ (63)	F2	2.007	2.46	2.92	1980	605	3860	56
	I$_3$–III–F$_6$	Na$_3$AlF$_6$	m	$P2_1/m$ (11)	F2	1.999	2.34	2.76	1880	575	3905	57
		Na$_3$GaF$_6$	m	$P2_1/m$ (11)	F2	2.000	2.34	2.78	1890	585	3890	213
		K$_3$AlF$_6$	t	$I4_1/a$ (88)	F2	2.008	2.33	2.64	1875	475	4160	56
		K$_3$GaF$_6$	t	$I4_1/a$ (88)	F2	2.005	2.33	2.72	1880	535	4010	58
		K$_3$ScF$_6$	c	$Fm\bar{3}m$ (225)	F2	1.991	2.41	2.89	1945	620	3780	162
		Rb$_3$AlF$_6$	c	$Fm\bar{3}m$ (225)	F2	2.004	2.44	2.83	1970	535	4000	214
		Cs$_3$AlF$_6$	c	$Fm\bar{3}m$ (225)	F2	1.984	2.40	2.89	1935	630	3740	215
		(NH$_4$)$_3$AlF$_6$	c	$F\bar{4}3m$ (216)	F1	1.998	2.41	2.75	1945	495	4080	47
		(Na$_{1.5}$Li$_{1.5}$)AlF$_6$	c	$Ia\bar{3}d$ (230)	F2	2.001	2.44	2.73	1970	450	4185	60
		(Na$_{1.5}$Li$_{1.5}$)GaF$_6$	c	$Ia\bar{3}d$ (230)	F2	1.997	2.43	2.72	1960	450	4175	216
		Na$_2$LiAlF$_6$	m	$P2_1/m$ (11)	F2	1.990	2.45	2.76	1975	470	4120	60
		K$_2$LiAlF$_6$	c	$Fm\bar{3}m$ (225)	F2	1.980	2.48	2.96	2000	615	3760	217
		K$_2$LiGaF$_6$	c	$Fm\bar{3}m$ (225)	F2	1.989	2.46	2.89	1980	575	3870	218
		K$_2$NaAlF$_6$	c	$Fm\bar{3}m$ (225)	F2	1.994	2.45	2.96	1975	645	3730	59
		K$_2$NaGaF$_6$	c	$Fm\bar{3}m$ (225)	F2	1.996	2.43	2.94	1960	645	3735	161
		K$_2$NaInF$_6$	c	$Fm\bar{3}m$ (225)	F2	1.991	2.28	2.75	1840	615	3795	219
		Rb$_2$KAlF$_6$	c	$Fm\bar{3}m$ (225)	F2	2.002	2.39	2.71	1930	480	4130	80
		Cs$_2$KAlF$_6$	c	$Fm\bar{3}m$ (225)	F2	1.988	2.23	2.42	1800	375	4335	80
		Cs$_2$RbAlF$_6$	c	$Fm\bar{3}m$ (225)	F2	1.994	2.31	2.54	1860	410	4270	80
		(NH$_4$)$_2$NaInF$_6$	c	$Fm\bar{3}m$ (225)	F2	1.989	2.26	2.75	1825	640	3745	164

Phosphors of the different crystal symmetry give rise to different XRD patterns. Figure 7 shows the XRD patterns, together with room-temperature PL spectra, of some fluoride phosphors of type F1.[8,46–53] All the phosphors in Fig. 7 are taken from a list in Table III. The cryogenic PL spectrum, if it is available, is also shown in the lower part of each room-temperature PL spectrum of Fig. 7. As easily expected, any strong PL intensity was not observed in the anti-Stokes spectrum region of the cryogenic PL spectra. Similarly, no clear ZPL emission peak can be found in these cryogenic PL spectra. A unique PL spectral feature observed in (NH$_4$)$_3$AlF$_6$:Mn^{4+} (Fig. 7b) is that each phonon-activated emission peak (ν_i) shows a very broad spectral width and, as a result, it is observed as a single, broad band in the Stokes and anti-Stokes spectral regions of the ZPL emission. No such broad emission band has been observed in hexafluoroammonium salt phosphors of a form of (NH$_4$)$_2$MF$_6$:Mn^{4+} with M = Si, Ge, Sn, and Ti.[42] Unfortunately, the cause of such spectral differences between the tri- and hexafluoroammonium salt phosphors cannot be completely understood at present.

The same figures as in Fig. 7, but those for phosphors of type F2 are shown in Figs. 8–10.[20,54–76] The cryogenic PL spectrum, if it is available, has also been plotted in the lower part of each room-temperature PL spectrum. In Fig. 9, that the peak energy of the ZPL emission at 300 K is observed at slightly longer wavelength than that at cryogenic temperature. Similarly, the spectral linewidth $\Delta\nu_{em}(T)$ of each PL peak in the Mn^{4+}-activated fluoride phosphors was observed to increase with increasing T, given by

$$\Delta\nu_{em}(T) = \Delta\nu_0 + \alpha_{BE}\left(1 + \frac{2}{e^{\theta_B/T} - 1}\right) \qquad [24]$$

where α_{BE} represents the electron−phonon interaction strength and θ_B describes the mean frequency of the phonons involved.[8] Figure 11 shows the results of $\Delta\nu_{em}(T)$ obtained from the PL spectra of Na$_2$TiF$_6$:Mn^{4+}.[50] The solid line represents the result calculated using Eq. 24 with $\Delta\nu_0 = 1.2$ meV, $\alpha_{BE} = 3.1$ meV, and $\theta_D = 220$ K. For comparison, the Raman linewidth ($\Delta\nu_R$) vs T data for GaAs reported by Chang et al.[77] are also plotted in Fig. 11.

In principle, θ_D is related to the Debye temperature. Equation 24 promises that $\Delta\nu_{em}(T)$ is relatively invariant against T at low temperatures and almost linearly increases with increasing T at > 50 K. In K$_2$SiF$_6$:Mn^{4+},[8] $\Delta\nu_{em}$ was observed to be relatively invariant among the different local vibronic modes, ∼3 meV, at $T \sim 20$ K and ∼ 6−7 meV at 300 K. Note that in semiconductor optics, the temperature-independent linewidth part $\Delta\nu_{em}(0) = \Delta\nu_0 + \alpha_{BE}$ is sensitive to crystalline quality mainly defined by the concentrations of foreign atoms and/or native lattice defects.[78] In the present intra-d-shell luminescence case, it is understood to be sensitive not only to the lattice defects but also to a delicate position or a site of the activator ions in the host lattice. As a result, an extremely broad emission band rather than a series of the sharp emission peaks can be observed in some Mn^{4+}-activated fluoride phosphors (see, e.g., Figs. 7b, 8a, 9i, 10c, and 10e).

In Figs. 8–10, some phosphors, especially LiSrGaF$_6$:Mn^{4+} (Fig. 8a), Na$_3$AlF$_6$:Mn^{4+} (Fig. 8d), KNaNbF$_7$:Mn^{4+} (Fig. 10b), Na$_3$TaF$_8$:Mn^{4+} (Fig. 10c), and Ba$_2$ZrF$_8$:Mn^{4+} (Fig. 10e), gave considerably strong ZPL emission intensities compared to their Stokes and anti-Stokes counterpart components. This unique PL spectral feature may be advantageous for use in an efficient warm w-LED device fabrication.

Figure 12 represents the plots of the ZPL emission energy vs crystal-field (Dq) and Racah parameters (B and C) for the Mn^{4+}-activated fluoride phosphors. All these parameters are calculated using Eq. 15 for Dq, Eq. 11 for B, and Eq. 12 for C and are listed in Table II. Note that $E(^4T_{1g,a})_{ZPL,m}$ given by Eq. 22, instead of $E(^4T_{1g,a})_{ZPL}$, was used in the B and C calculations. The apparent Racah parameters in a complex must be always less than the free ion values because the electrons on the metal can be delocalized into molecular orbitals covering both the met al. As a consequence of this delocalization or cloud expanding, the average inter-electronic repulsion should be reduced.

Table IIb. Summary of crystal class (CC), space group (SG), phosphor type (F1 or F2), ZPL emission energy [$^2E_g = E(^2E_g)_{ZPL}$], ZPL excitation absorption energies [$^4T_{2g} = E(^4T_{2g})_{ZPL}$; $^4T_{1g,a} = E(^4T_{1g,a})_{ZPL}$], crystal-field parameter (Dq), and Racah parameters (B and C) at 300 K for some Mn^{4+}-activated fluoride phosphors. The Racah parameters were calculated using Eqs. 11 and 12 with introducing values of $E(^4T_{1g,a})_{ZPL,m}$ into Eq. 22 instead of $E(^4T_{1g,a})_{ZPL}$. c = cubic; tr = trigonal; h = hexagonal; o = orthorhombic; m = monoclinic; t = tetragonal. (1 eV = 8068 cm^{-1}).

System	Formula	Fluoride host	CC	SG	Type	^2E_g (eV)	$^4T_{2g}$ (eV)	$^4T_{1g,a}$ (eV)	Dq (cm^{-1})	B (cm^{-1})	C (cm^{-1})	Ref.
$I_x-IV_y-F_{x+4y}$	I–IV–F$_5$	KTeF$_5$	o	*Pbcm* (57)	F2	1.998	2.45	2.93	1975	615	3805	61
	I$_2$–IV–F$_6$	Li$_2$SiF$_6$	tr	*P*321 (150)	F2	2.000	2.49	2.91	2010	505	4060	220
		Li$_2$ZrF$_6$	tr	*P$\bar{3}$1m* (162)	F1	2.005	2.22	2.63	1790	505	4080	48
		Na$_2$SiF$_6$	tr	*P*321 (150)	F2	2.007	2.44	2.90	1970	540	4000	62
		Na$_2$GeF$_6$	tr	*P*321 (150)	F2	2.008	2.38	2.86	1920	560	3960	221
		Na$_2$SnF$_6$	t	*P*4$_2$/*mnm* (136)	F1	2.005	2.39	2.83	1930	525	4030	49
		Na$_2$TiF$_6$	tr	*P*321 (150)	F2	2.006	2.49	2.97	2010	555	3960	50
		Na$_2$ZrF$_6$	m	*P*2$_1$/*c* (14)		Mn^{2+}-like PL spectrum						222
		K$_2$SiF$_6$	c	*Fm$\bar{3}$m* (225)	F1	1.993	2.45	2.94	1975	565	3900	8
		K$_2$GeF$_6$	tr	*P$\bar{3}$m1* (164)	F1	1.990	2.43	2.88	1960	530	3975	124
		K$_2$SnF$_6$·6H$_2$O	o	*Fddd* (70)	F2	1.998	2.42	2.87	1950	535	3995	63
		K$_2$TiF$_6$	tr	*P$\bar{3}$m1* (164)	F1	1.991	2.48	2.89	2000	495	4055	50
		K$_2$ZrF$_6$	m	*C*2/*c* (15)		A mixture with cubic K$_3$ZrF$_7$ (Mn^{4+}-related PL spectrum)						222
		K$_2$MnF$_6$	c	*Fm$\bar{3}$m* (225)	F1	1.993	2.57	2.90	2075	430	4215	223
		K$_2$MnF$_6$	h	*P*6$_3$*mc* (186)	F2	1.993	2.43	2.74	1960	415	4250	20
		Rb$_2$SiF$_6$	c	*Fm$\bar{3}$m* (225)	F1	1.992	2.48	2.93	2000	530	3980	197
		Rb$_2$GeF$_6$	h	*P*6$_3$*mc* (186)	F2	1.992	2.41	2.95	1945	615	3795	122
		Rb$_2$SnF$_6$	tr	*P$\bar{3}$m1* (164)	F1	1.999	2.36	2.80	1905	525	4015	224
		Rb$_2$TiF$_6$	tr	*P$\bar{3}$m1* (164)	F1	1.991	2.34	2.83	1890	570	3890	197
		Rb$_2$ZrF$_6$	tr	*P$\bar{3}$m1* (164)	F1	1.999	2.30	2.72	1855	510	4050	159
		Rb$_2$HfF$_6$	tr	*P$\bar{3}$m1* (164)	F1	1.994	2.27	2.74	1830	555	3935	225
		Cs$_2$SiF$_6$	c	*Fm$\bar{3}$m* (225)	F1	1.986	2.39	2.82	1930	515	4000	226
		Cs$_2$GeF$_6$	c	*Fm$\bar{3}$m* (225)	F1	1.987	2.43	2.87	1955	525	3985	226
		Cs$_2$SnF$_6$	tr	*P$\bar{3}$m1* (164)	F1	1.989	2.38	2.76	1920	475	4105	49
		Cs$_2$TiF$_6$	tr	*P$\bar{3}$m1* (164)	F1	1.994	2.42	2.82	1950	490	4080	50
		Cs$_2$ZrF$_6$	tr	*P$\bar{3}$m1* (164)	F1	1.992	2.21	2.51	1785	410	4260	227
		Cs$_2$HfF$_6$	tr	*P$\bar{3}$m1* (164)	F1	1.991	2.32	2.75	1870	520	4010	225
		Cs$_2$MnF$_6$	c	*Fm$\bar{3}$m* (225)	F1	1.987	2.58	2.69	2080	260	4605	81
		(NH$_4$)$_2$SiF$_6$	c	*Fm$\bar{3}$m* (225)	F1	1.987	2.51	2.94	2025	510	4005	42
		(NH$_4$)$_2$GeF$_6$	tr	*P$\bar{3}$m1* (164)	F1	1.986	2.45	2.88	1975	515	4000	42
		(NH$_4$)$_2$SnF$_6$	tr	*P$\bar{3}$m1* (164)	F1	1.985	2.38	2.81	1920	515	3995	42
		(NH$_4$)$_2$TiF$_6$	tr	*P$\bar{3}$m1* (164)	F1	1.986	2.38	2.80	1920	510	4020	42
		(Na$_{1.5}$Li$_{0.5}$)SiF$_6$	o	Unidentified	F2	2.000	2.43	2.78	1960	450	4195	228
		KNaSiF$_6$	o	*Pnma* (62)	F2	2.000	2.52	2.93	2035	495	4080	64
		KNaSnF$_6$	o	*Pna*2$_1$ (33)	F2	2.009	2.31	2.71	1865	495	4115	229
		CsNaGeF$_6$	o	*Pbcm* (57)	F2	2.003	2.41	2.71	1945	405	4295	66
		Na$_2$(Ge$_{0.5}$Si$_{0.5}$)F$_6$	tr	*P*321 (150)	F2	2.006	2.26	2.60	1825	445	4225	230
		Na$_2$(Ti$_{0.5}$Ge$_{0.5}$)F$_6$	tr	*P*321 (150)	F2	2.006	2.26	2.60	1825	445	4225	230
		K$_2$(Ge$_{0.5}$Si$_{0.5}$)F$_6$	h	*P*6$_3$*mc* (186)	F2	1.996	2.13	2.83	1715	810	3410	231
	I$_3$–IV–F$_7$	Na$_3$ZrF$_7$	t	*I*4/*mmm* (139)	F2	1.994	2.49	2.87	2010	525	3995	67
		K$_3$SiF$_7$	t	*P*4/*mbm* (127)	F1	2.002	2.46	2.53	1985	280	4600	51
		K$_3$ZrF$_7$	c	*Fm$\bar{3}$m* (225)	F2	1.999	2.29	2.68	1850	540	3980	68
		K$_3$HfF$_7$	c	*Fm$\bar{3}$m* (225)	F2	1.996	2.31	2.77	1865	605	3830	232
		Rb$_3$SiF$_7$	t	*P*4/*mbm* (127)	F1	1.994	2.46	2.83	1985	520	4015	233
		Cs$_3$SiF$_7$	t	*P*4/*mbm* (127)	F1	1.997	2.52	2.93	2035	550	3945	233
		CsRb$_2$SiF$_7$	t	*P*4/*mbm* (127)	F1	1.995	2.45	2.80	1975	500	4055	233
		Cs$_2$RbSiF$_7$	t	*P*4/*mbm* (127)	F1	1.997	2.48	2.91	2000	570	3905	233
	I$_4$–IV–F$_8$	K$_3$SnF$_8$	m	*C*2/*c* (15)	F2	2.008	2.33	2.61	1880	445	4220	69
		Na$_3$HTiF$_8$	o	*Cmcm* (63)	F2	1.999	2.18	2.69	1760	665	3715	70
	I$_5$–IV$_2$–F$_{13}$	Na$_5$Zr$_2$F$_{13}$	m	*C*2/*m* (12)	F2	2.011	2.45	2.86	1975	555	3980	71

The Racah parameters of the free Mn^{4+} ion are $B_0 = 1160$ cm^{-1} and $C_0 = 4303$ cm^{-1}.[79]

Unfortunately, our obtained C values for some phosphors, Cs$_2$KAlF$_6$:Mn^{4+},[80] Cs$_2$MnF$_6$ ($T = 77$ K),[81] and K$_3$SiF$_7$:Mn^{4+},[51] are larger than the free ion value (Table II). One reason for these large C values may come from insufficient correction of the $E(^4T_{1g,a})$ transition energy caused by the modification of neighboring $A_{2g} \rightarrow {}^2T_{2g}$ and $^4A_{2g} \rightarrow {}^4T_{1g,b}$/CTB) transitions via correction factor of m in Eq. 22. Indeed, an extremely large $A_{2g} \rightarrow {}^2T_{2g}$ excitation component has been observed in the PLE spectrum of K$_3$SiF$_7$:Mn^{4+} on the

higher energy side of the $A_{2g} \rightarrow {}^4T_{2g}$ excitation transition band (see Fig. S24 in Ref. 1). In Fig. 12, the ZPL emission energy (^2E_g) shows no strong dependence on Dq, B, or C and falls in the range of $^2E_g = 1.996 \pm 0.020$ eV.

Oxide phosphors.—*Type O-A phosphors.*—The PL spectral feature observed in the Mn^{4+}-activated oxide phosphors can be classified into three subgroups, namely, O-A (A), O-B (B), and O-C (C). All these oxide phosphors are summarized in Table IV. Among these phosphors, type O-A has been most popularly obtained from various

Table IIc. Summary of crystal class (CC), space group (SG), phosphor type (F1 or F2), ZPL emission energy [$^2E_g = E(^2E_g)_{ZPL}$], ZPL excitation absorption energies [$^4T_{2g} = E(^4T_{2g})_{ZPL}$; $^4T_{1g,a} = E(^4T_{1g,a})_{ZPL}$], crystal-field parameter (Dq), and Racah parameters (B and C) at 300 K for some Mn^{4+}-activated fluoride phosphors. The Racah parameters were calculated using Eqs. 11 and 12 with introducing values of $E(^4T_{1g,a})_{ZPL,m}$ into Eqs. 22 instead of $E(^4T_{1g,a})_{ZPL}$. c = cubic; tr = trigonal; h = hexagonal; o = orthorhombic; m = monoclinic; t = tetragonal. (1 eV = 8068 cm^{-1}).

System	Formula	Fluoride host	CC	SG	Type	^2E_g (eV)	$^4T_{2g}$ (eV)	$^4T_{1g,a}$ (eV)	Dq (cm^{-1})	B (cm^{-1})	C (cm^{-1})	Ref.
$I_x-V_y-F_{x+5y}$	I_2-V-F_7	K_2NbF_7	m	$P2_1/c$ (14)	F2	2.002	2.33	2.65	1880	475	4140	72
		K_2TaF_7	m	$P2_1/c$ (14)	F2	2.001	2.34	2.65	1890	465	4155	72
		$KNaNbF_7$	o	$P2_12_12_1$ (19)	F2	2.001	2.35	2.58	1895	405	4300	73
		$KNaTaF_7$	o	$P2_12_12_1$ (19)	F2	2.001	2.37	2.61	1910	410	4280	73
	I_3-V-F_8	Na_3TaF_8	m	$C2/c$ (15)	F2	2.002	2.43	2.83	1960	545	3980	74
$II_x-III_y-F_{2x+3y}$	$II_5-III-F_{13}$	Ba_5AlF_{13}	c	$Fm\bar{3}m$ (225)	F2	1.999	2.50	2.82	2015	475	4125	75
$II_x-IV_y-F_{2x+4y}$	$II-IV-F_6$	$BaSiF_6$	tr	$R\bar{3}m$ (166)	F1	1.987	2.43	2.86	1960	570	3875	52
		$BaGeF_6$	tr	$R\bar{3}m$ (166)	F1	1.985	2.43	2.84	1960	555	3910	234
		$BaSnF_6$	tr	$R\bar{3}m$ (166)	F1	1.990	2.38	2.83	1920	595	3840	235
		$BaTiF_6$	tr	$R\bar{3}m$ (166)	F1	1.980	2.42	2.84	1950	565	3875	125
		$ZnSiF_6\cdot6H_2O$	tr	$R\bar{3}$ (148)	F1	1.991	2.40	2.81	1935	555	3925	53
		$ZnGeF_6\cdot6H_2O$	tr	$R\bar{3}$ (148)	F1	1.994	2.34	2.76	1890	565	3910	44
		$ZnSnF_6\cdot6H_2O$	tr	$R\bar{3}$ (148)	F1	1.998	2.37	2.77	1910	550	3960	45
		$ZnTiF_6\cdot6H_2O$	tr	$R\bar{3}$ (148)	F1	1.996	2.37	2.80	1910	575	3895	236
	II_2-IV-F_8	Ba_2ZrF_8	o	$Pnma$ (62)	F2	1.991	2.49	2.90	2010	550	3930	76

Table III. Representative examples of fluoride phosphors belonging to the different crystal system and chemical formula with the different crystal class (CC), type (F1 or F2), and space group (SG). Here, " + " and " − " mean that the Mn^{4+}-related ZPL emission intensity (ZPL), piezoelectricity activity (PZ), and optical rotation activity (OR) are strong and weak (or forbidden in principle), respectively. The XRD patterns and PL spectra for these phosphors are shown in Fig. 7 (type F1 phosphors) and Figs. 8–10 (type F2 phosphors). c = cubic; tr = trigonal; h = hexagonal; o = orthorhombic; m = monoclinic; t = tetragonal.

| System	Formula	Fluoride host	CC	Type	SG	ZPL	PZ	OR
$I_x-II_y-F_{x+2y}$	$I-II-F_3$	$KZnF_3$	c	F1	$Pm\bar{3}m$ (221)	−	−	−
$I_x-II_y-III_z-F_{x+2y+3z}$	$I-II-III-F_6$	$LiSrGaF_6$	tr	F2	$P\bar{3}1c$ (163)	+	−	−
$I_x-III_y-F_{x+3y}$	$I-III-F_4$	$NaYF_4$	h	F2	$P\bar{6}$ (174)	+	+	−
	$I_2-III-F_5$	$K_2AlF_5\cdot H_2O$	o	F2	$Cmcm$ (63)	+	−	−
	$I_3-III-F_6$	Na_3AlF_6	m	F2	$P2_1/m$ (11)	+	−	−
		K_3GaF_6	t	F2	$I4_1/a$ (88)	+	−	−
		K_2NaAlF_6	c	F2	$Fm\bar{3}m$ (225)	+	−	−
		$(NH_4)_3AlF_6$	c	F1	$F\bar{4}3m$ (216)	−	+	−
		$Na_{1.5}Li_{1.5}AlF_6$	c	F2	$Ia\bar{3}d$ (230)	+	−	−
$I_x-IV_y-F_{x+4y}$	$I-IV-F_5$	$KTeF_5$	o	F2	$Pbcm$ (57)	+	−	−
	I_2-IV-F_6	Na_2SiF_6	tr	F2	$P321$ (150)	+	+	+
		Li_2ZrF_6	tr	F1	$P\bar{3}1m$ (162)	−	−	−
		Na_2SnF_6	t	F1	$P4_2/mnm$ (136)	−	−	−
		K_2SiF_6	c	F1	$Fm\bar{3}m$ (225)	−	−	−
		Cs_2TiF_6	tr	F1	$P\bar{3}m1$ (164)	−	−	−
		$K_2SnF_6\cdot6H_2O$	o	F2	$Fddd$ (70)	+	−	−
		K_2ZrF_6[*1]	m	F1	$C2/c$ (15)	−	−	−
		K_2MnF_6	h	F2	$P6_3mc$ (186)	+	+	−
		$(Na_{1.5}Li_{0.5})SiF_6$	o	F2	Unidentified	+		
		$KNaSiF_6$	o	F2	$Pnma$ (62)	+	−	−
		$KNaSnF_6$	o	F2	$Pna2_1$ (33).	+	+	+
		$CsNaGeF_6$	o	F2	$Pbcm$ (57)	+	−	−
	I_3-IV-F_7	Na_3ZrF_7	t	F2	$I4/mmm$ (139)	+	−	−
		K_3SiF_7	t	F1	$P4/mbm$ (127)	−	−	−
		K_3ZrF_7	c	F2	$Fm\bar{3}m$ (225)	+	−	−
	I_4-IV-F_8	K_3HSnF_8	m	F2	$C2/c$ (15)	+	−	−
		Na_3HTiF_8	o	F2	$Cmcm$ (63)	+	−	−
	$I_5-IV_2-F_{13}$	$Na_5Zr_2F_{13}$	m	F2	$C2/m$ (12)	+	−	−
$I_x-V_y-F_{x+5y}$	I_2-V-F_7	K_2NbF_7	m	F2	$P2_1/c$ (14)	+	−	−
		$KNaNbF_7$	o	F2	$P2_12_12_1$(19)	+	+	+
	I_3-V-F_8	Na_3TaF_8	m	F2	$C2/c$ (15)	+	−	−
$II_x-III_y-F_{2x+3y}$	$II_5-III-F_{13}$	Ba_5AlF_{13}	c	F2	$Fm\bar{3}m$ (225)	+	−	−
$II_x-IV_y-F_{2x+4y}$	$II-IV-F_6$	$BaSiF_6$	tr	F1	$R\bar{3}m$ (166)	−	−	−
		$ZnSiF_6\cdot6H_2O$	tr	F1	$R\bar{3}$ (148)	−	−	−
	II_2-IV-F_8	Ba_2ZrF_8	o	F2	$Pnma$ (62)	+	−	−

[*1] A mixture with cubic K_3ZrF_7.
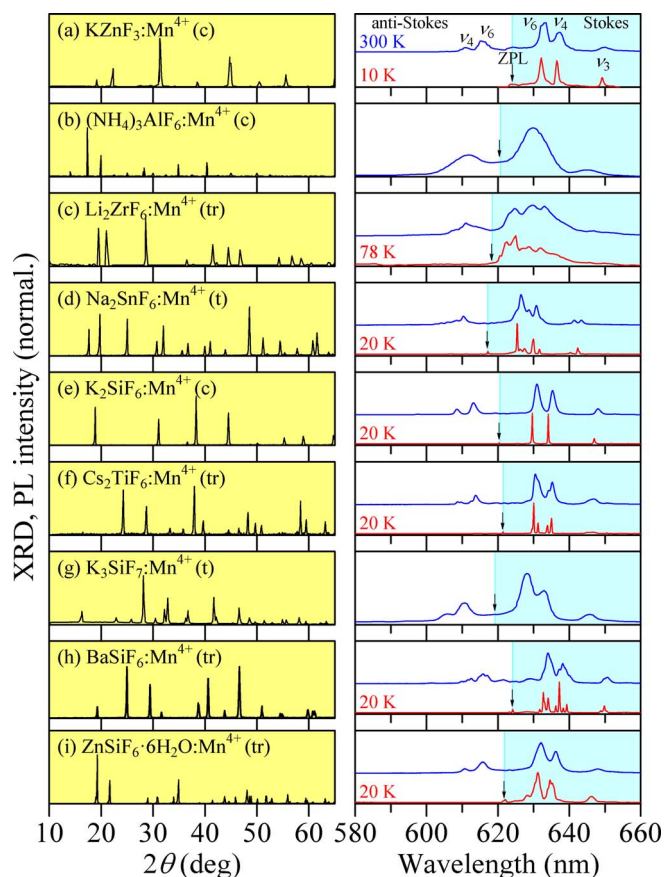
Figure 7. XRD patterns and PL spectra measured at 300 K of some fluoride phosphors of type F1.[8,46–53] If cryogenic-temperature PL spectrum is available, its spectrum is also plotted in the lower part of each figure. The crystal class of each host material is given in the parenthesis following after the phosphor name (Table III). The vertical arrow on the right-hand side of each figure shows the position of the $E(^2E_g)_{ZPL}$ emission energy (ZPL).
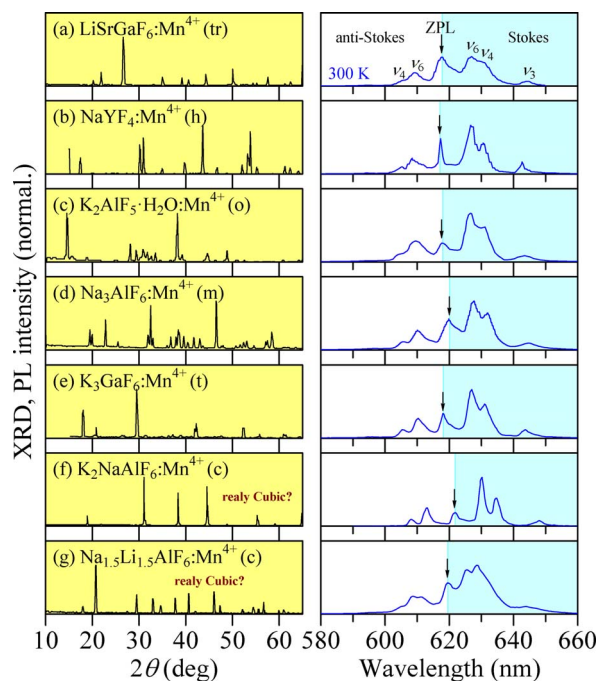

Figure 8. XRD patterns and PL spectra measured at 300 K of some fluoride phosphors of type F2 ($I_x-II_y-III_z-F_{x+2y+3z}$ and $I_x-III_y-F_{x+3y}$).[54–60] The crystal class of each host material is given in the parenthesis following after the phosphor name (Table III). The vertical arrow on the right-hand side of each figure shows the position of the $E(^2E_g)_{ZPL}$ emission energy (ZPL).

oxide hosts. This type of phosphors can also be divided into O-A1 and O-A2, where their room-temperature ZPL emission is weak (O-A1) or strong (O-A2). Some examples of type O-A phosphors are shown in Figs. 13 and 14.[29,82–94]

In Fig. 13, the ZPL emission energy can be estimated to locate in the middle between the strongest Stokes and next-strongest anti-Stokes broad emission bands. This is a simple method to reasonably estimate the ZPL emission energy in such type O-A1 phosphors only from room-temperature PL spectrum. On the other hand, the ZPL emission energy in type O-A2 phosphors can be more exactly determined from PL spectrum measured even at room temperature. This is because of the direct ZPL emission peak observation caused by its relatively sharp and strong peak nature even at room temperature (Fig. 14). Roughly speaking, the XRD patterns on the left-hand side of Fig. 14 are more complex than those in Fig. 13. This promises an observation of the relatively strong ZPL emission in type O-A2 oxide phosphors, reflecting more complex crystallinity of this type of phosphors. Like fluoride phosphors of type F2 (Tables II and III), all the hexagonal oxide phosphors in Fig. 14 belong to type O-A2 (i.e., relatively strong ZPL emission even at room temperature).

PL spectra of some oxide phosphors were examined at both room and cryogenic temperatures. We reproduce in Figs. 15 and 16 such room- and cryogenic-temperature PL spectra, together with the room-temperature PLE spectra.[95–106] As evidenced from Fig. 15, the low-temperature PL spectra make possible to more exactly determine the ZPL emission energies at room temperature. Because of no strong temperature dependence of the ZPL emission energies,[8] its cryogenic value can be safely recognized to be almost the same as the room

temperature value. We note, however, that the ZPL emission peak for type O-A1 phosphors in Fig. 15 is observed as a weak peak at cryogenic temperature. This is in direct contrast to the case of type O-A2 phosphors, where the strongest or strong ZPL emission peak can be usually observed regardless of temperatures low or high. As an extremely case, only one peak that is the ZPL emission peak is observed at cryogenic temperature (Fig. 16a). No clear difference in the PLE spectral feature has also been observed for phosphors of types O-A1 and O-A2.

Type O-B phosphors.—As can be understood from Fig. 4e (Fig. 5e), this type of phosphors promises to exhibit a PL spectrum having Poisson-like lineshape or, in other words, an asymmetric Gaussian-like lineshape. The host crystals of type O-B are limited to a family of Li−Mg−IV oxides with IV = Sn, Ti, and Zr (Table IV). They crystallize in the space groups of cubic $Fm\bar{3}m$ ($Li_2Mg_3SnO_6$, Li_2MgTiO_4), cubic $P4_132$ ($Li_2MgTi_3O_8$), and tetragonal $I4_1/amd$ (Li_2MgZrO_4).

Almost all the PL studies on type O-B phosphors were performed from room temperature up to 500 K, but not at any temperatures lower than room temperature.[107–110] These studies reported no clear change in the PL spectral feature from room temperature to 500 K and, as a result, did not enable to explicitly determine the ZPL emission energies in such phosphors. Only a study by Jin et al.[31] performed PL measurements from $T = 77$ to 500 K. However, any fine structure characterizing the ZPL emission transition of type O-B phosphor was not observed in the PL spectra even at 77 K. Therefore, we estimate the ZPL emission energies ^2E_g for type O-B phosphors by analyzing the room-temperature PL spectra and assuming a Poisson distribution function of Eq. 6. The results of these analyses are shown in Fig. 17.[107–110] The ZPL emission energies determined from the present analyses are listed in Table IV.

Type O-C phosphors.—The PL spectral feature of type O-C phosphors is clearly different from the other oxide phosphors in sense of exhibiting a multiple-peak structure. No any PL measurement at a cryogenic temperature has been performed on type O-C phos-

Table IVa. Summary of phosphor type (O-A, O-B, or O-C), ZPL emission energy [$^2E_g = E(^2E_g)_{ZPL}$], ZPL excitation absorption energies [$^4T_{2g} = E(^4T_{2g})_{ZPL}$; $^4T_{1g,a} = E(^4T_{1g,a})_{ZPL}$], crystal-field parameter (Dq), and Racah parameters (B and C) at 300 K for some Mn^{4+}-activated oxide phosphors. Blank in a column of "Type" means no available PL spectrum at 300 K. The Racah parameters were calculated using Eqs. **11** and **12** with introducing $m = 0$ into Eqs. **22.** (**1 eV = 8068 cm^{-1}**).

Oxide host	Type	^2E_g (eV)	$^4T_{2g}$ (eV)	$^4T_{1g,a}$ (eV)	Dq (cm^{-1})	B (cm^{-1})	C (cm^{-1})	Ref.
α-Al$_2$O$_3$		1.832 (R$_1$)	2.26	—	1825	—	—	237
		1.842 (R$_2$)						237
	O-A	1.836	2.13	2.96	1720	665	3290	238
BaAl$_2$Ge$_2$O$_8$	O-A	1.902	2.41	3.29	1945	690	3390	239
Ba$_2$GdNbO$_6$	O-A	1.831	2.21	2.84	1785	470	3700	174
Ba$_2$GdSbO$_6$	O-A	1.840	2.26	2.80	1825	395	3900	240
BaGe$_4$O$_9$	O-A	1.897	2.40	3.36	1935	775	3195	241
	O-A	1.861	2.25	3.00	1815	575	3540	99
Ba$_2$GeO$_4$	O-A	1.858	2.46	3.30	1985	650	3360	242
Ba$_2$LaNbO$_6$	O-A	1.867	2.22	2.69	1790	340	4100	95
Ba$_2$LaTaO$_6$	O-A	1.860	2.19	2.60	1765	295	4195	29
Ba$_2$LaSbO$_6$	O-A	1.870	2.21	2.74	1785	385	3995	178
BaMgAl$_{10}$O$_{17}$	O-A	1.878	2.34	2.95	1890	450	3870	243
	O-A	1.877	2.23	2.75	1800	380	4035	244
Ba$_2$MgGe$_2$O$_7$	O-A	1.929	2.73	3.75	2205	805	3190	82
BaMgLaNbO$_6$	O-A	1.785	2.02	2.56	1630	400	3745	245
BaMgLaSbO$_6$	O-A	1.778	2.15	2.85	1735	535	3415	170
BaMg$_6$Ti$_6$O$_{19}$	O-A	1.885	2.25	2.85	1815	445	3905	246
Ba$_2$TiGe$_2$O$_8$	O-A	1.858	2.54	3.15	2050	445	3820	247
Ba$_2$YNbO$_6$	O-A	1.835	2.07	2.74	1670	510	3625	83
Ba$_2$YSbO$_6$	O-A	1.832	2.17	2.72	1750	405	3855	248
BaZnAl$_{10}$O$_{17}$	O-A	1.867	2.25	3.10	1815	675	3345	249
BeAl$_2$O$_4$	O-A	1.826	2.60	No peak	2098	—	—	250

phors until recently. These facts make impossible to identify which peak comes from the ZPL emission peak, but not from its satellite peaks.[2,111–118] However, Qin et al.[38] recently measured the PL spectra of La$_2$LiNbO$_6$:Mn^{4+} from cryogenic temperature ($T = 10$ K) up to 473 K. It is known that a low-temperature PL spectrum usually shows only a sharp peak caused by the ZPL transition together with its Stokes counterpart peaks (see, e.g., Figs. 15 and 16). Thus, the highest emission peak in such PL spectrum should be rightly assigned as a ZPL transition peak. In fact, the 10-K PL spectrum measured by Qin et al.[38] revealed a clear "ZPL" emission peak at 1.783 eV (Fig. 18i). The 10- and 300-K PL spectra in Fig. 18i are used as a guideline for estimating the ZPL emission energies at 300 K of other phosphors of type O-C shown in Figs. 18a–18h (Refs. 111−118). The corresponding ZPL energies are indicated by the vertical dashed lines on the left-hand side of Figs. 18a–18h.

More recently, Wu et al.[39] examined the temperature dependence of PL spectra for Ca$_{14−x}$Sr$_x$Zn$_6$Al$_{10}$O$_{35}$:Mn^{4+} at temperatures from cryogenic ($T = 80$ K) to 580 K and observed a sharp peak at 1.792 eV as an abrupt tail-end peak in the $T = 80$ K PL spectrum. This abrupt tail-end peak can also be concluded to originate from the ZPL emission peak $^2E_g \rightarrow {}^4A_{2g}$ in Ca$_{14−x}$Sr$_x$Zn$_6$Al$_{10}$O$_{35}$:Mn^{4+}.

The red emission energies, $E(^2E_g)$ [$E(^2E_g)_{ZPL}$], together with the first and second spin-allowed PLE band energies, $E(^4T_{2g})_{ZPL}$ and $E(^4T_{1g,a})_{ZPL}$, for all the Mn^{4+}-activate oxide phosphors of types O-A, O-B, and O-C are listed in Table IV. The PLE band energy values were determined by fitting the experimental data with Eq. 4. The crystal-field parameter Dq for the Mn^{4+} ion can also be obtained from Eq. 15. Introducing such numeric phosphor parameters into Eqs. 11 and 12, the Racah parameters B and C for the Mn^{4+}-activated oxide phosphors can be successfully obtained. All these Mn^{4+}-activated oxide phosphor parameters are listed in Table IV.

Figure 12a plots the $E(^2E_g)_{ZPL}$ vs Dq values observed at room temperature for the Mn^{4+}-activated oxide phosphors of types O-A, O-B, and O-C (solid circles). The solid line in Fig. 12a represents the relation obtained by performing the least-squares fit, written as

$$E(^2E_g)_{ZPL} = 2.015 \times 10^{-4} Dq + 1.486 \text{ eV} \quad [25]$$

Similarly, the $E(^2E_g)_{ZPL}$ vs B and C plots for the oxide phosphors are shown in Figs. 12b and 12c, respectively. The least-squares fits gave the following linear relations:

$$E(^2E_g)_{ZPL} = -3.19 \times 10^{-5} B + 1.865 \text{ eV} \quad [26]$$

$$E(^2E_g)_{ZPL} = 6.87 \times 10^{-5} C + 1.597 \text{ eV} \quad [27]$$

It is noted that Mg$_4$Al$_{14}$O$_{25}$:Mn^{4+} exhibited considerably narrower $A_{2g} \rightarrow {}^4T_{2g}$ excitation band in its PLE spectrum than other oxide phosphors, and promised that this phosphor has considerably larger C value than the free ion value (Table IV).[119]

Oxyfluoride and some fluorine compound phosphors.—The phosphor properties of Mn^{4+}-activated oxyfluorides can be classified into two subgroups, namely, OF-A and OF-B. Type OF-A shows the spectroscopic phosphor properties akin to the fluoride phosphors and type OF-B akin to the oxide ones. Table V summarizes the Mn^{4+}-activated oxyfluoride phosphors and their important phosphor parameters, together with those for the fluorine compound phosphors, BaNb(OH)$_{1.5}$F$_{5.5}$:Mn^{4+} (type HF) and NaHF$_2$:Mn^{4+} (type AB).

Figure 19 shows the $E(^2E_g)_{ZPL}$ vs Dq, B, and C plots at 300 K for the oxyfluoride and fluorine compound phosphors listed in Table V. Because the PL spectral features of BaNb(OH)$_{1.5}$F$_{5.5}$:Mn^{4+} and NaHF$_2$:Mn^{4+} are very similar to that of type OF-A (or type F2), they are regarded as "type OF-A" in the plots of Fig. 19. The heavy and light solid lines in Fig. 19 represent tendencies of the fluoride and oxide phosphors observed in Fig. 12, respectively. As expected, the experimental data of type OF-A oxyfluoride phosphors in Fig. 19 can be well explained by the heavy solid lines ("fluoride" phosphors). Similarly, those of type OF-B oxyfluoride phosphors, though the experimental data are largely scatted, follow the "oxide" phosphor tendency reasonably well.

Nephelauxetic parameter and ZPL emission energy.—Brik et al.[23,120,121] derived the linear relation between a newly defined nephelauxetic parameter, β_1, and ZPL emission energy, ^2E_g [$E(^2E_g)_{ZPL}$], for various Mn^{4+}-activated fluoride and oxide phos-

Table IVb. Summary of phosphor type (O-A, O-B, or O-C), ZPL emission energy [$^2E_g = E(^2E_g)_{ZPL}$], ZPL excitation absorption energies [$^4T_{2g} = E(^4T_{2g})_{ZPL}$; $^4T_{1g,a} = E(^4T_{1g,a})_{ZPL}$], crystal-field parameter (*Dq*), and Racah parameters (*B* and *C*) at 300 K for some Mn^{4+}-activated oxide phosphors. Blank in a column of "Type" means no available PL spectrum at 300 K. The Racah parameters were calculated using Eqs. **11** and **12** with introducing *m* = 0 into Eqs. **22**. (1 eV = 8068 cm^{-1}).

Oxide host	Type	^2E_g (eV)	$^4T_{2g}$ (eV)	$^4T_{1g,a}$ (eV)	*Dq* (cm^{-1})	*B* (cm^{-1})	*C* (cm^{-1})	Ref.
CaAl$_2$O$_4$	O-A	1.883	2.32	2.93	1870	450	3880	167
CaAl$_4$O$_7$	O-A	1.892	2.33	2.95	1880	460	3885	100
	O-A	1.891	2.46	2.93	1985	335	4170	251
CaAl$_{12}$O$_{19}$	O-A	1.898	2.44	2.85	1970	290	4295	252
	O-A	1.890	2.22	—	1790	—	—	101
	O-A	1.904	2.36	2.88	1905	375	4110	88
Ca$_2$AlNbO$_6$	O-A	1.770	2.05	2.59	1655	400	3710	253
CaGdAlO$_4$	O-A	1.737	2.05	2.63	1655	435	3545	201
Ca$_2$GdNbO$_6$	O-A	1.834	2.27	2.78	1830	370	3940	254
Ca$_2$GdSbO$_6$	O-A	1.827	1.98	2.53	1595	410	3835	188
Ca$_2$LaNbO$_6$	O-A	1.813	2.05	2.58	1655	390	3840	255
Ca$_2$LaSbO$_6$	O-A	1.810	1.92	2.73	1550	665	3235	180
Ca$_2$LaTaO$_6$	O-A	1.815	1.96	2.70	1580	585	3410	29
	O-A	1.811	2.10	2.60	1695	365	3895	181
Ca$_3$La$_2$W$_2$O$_{12}$	O-A	1.750	2.03	2.73	1640	540	3335	166
	O-A	1.762	2.15	2.83	1735	515	3415	169
CaMg$_2$Al$_{16}$O$_{27}$	O-A	1.892	2.38	2.85	1920	335	4170	89
	O-A	1.886	2.22	2.88	1790	495	3785	30
Ca$_2$Mg$_2$Al$_{28}$O$_{46}$	O-A	1.890	2.05	2.76	1655	550	3685	30
CaMgLaNbO$_6$	O-A	1.782	2.11	2.67	1700	415	3705	256
CaMgLaSbO$_6$	O-A	1.783	2.11	2.65	1700	395	3745	205
CaMgLaTaO$_6$	O-A	1.782	2.11	2.67	1700	415	3705	256
Ca$_2$MgYAlSnSi$_2$O$_{12}$		1.857	2.01	2.82	1620	655	3375	257
CaMgYSbO$_6$	O-A	1.805	2.01	2.82	1620	655	3235	186
Ca$_3$ScGaSnSi$_2$O$_{12}$		1.879	2.13	2.82	1720	525	3705	257
CaTiO$_3$	O-A	1.753	2.24	3.02	1805	605	3190	258
CaYAlO$_4$	O-A	1.750	2.06	3.10	1660	940	2515	259
Ca$_3$YAl$_3$B$_4$O$_{15}$	O-A	1.828	2.46	3.04	1985	425	3795	260
CaY$_2$Al$_4$SiO$_{12}$	O-A	1.885	2.22	2.81	1790	435	3920	96
CaY$_2$Ga$_2$Al$_2$SiO$_{12}$	O-A	1.889	2.14	2.97	1725	665	3430	96
Ca$_2$YGa$_3$Sn$_2$O$_{12}$		1.848	2.06	2.82	1660	600	3470	257
Ca$_2$YGa$_3$SnSiO$_{12}$		1.862	2.22	2.84	1790	460	3800	257
Ca$_2$YSbO$_6$	O-A	1.850	2.07	2.78	1670	550	3580	261
CaY$_2$Sc$_2$Al$_2$SiO$_{12}$	O-A	1.883	2.11	2.92	1700	645	3455	96
Ca$_3$ZnAl$_4$O$_{10}$	O-C	1.776	2.26	2.92	1825	495	3500	111
Ca$_{14}$Zn$_6$Al$_{10}$O$_{35}$	O-C	1.784	2.26	2.92	1825	495	3520	112
	O-C	1.780	2.38	2.98	1920	440	3630	32
	O-C	1.789	2.17	2.92	1750	580	3345	39
Ca$_{14}$Zn$_6$Ga$_{10}$O$_{35}$	O-C	1.790	2.04	2.85	1645	650	3200	113
CaZrO$_3$		1.855	2.07	2.60	1670	390	3955	262

phors. Here, β_1 can be defined by

$$\beta_1 = \sqrt{\left(\frac{B}{B_0}\right)^2 + \left(\frac{C}{C_0}\right)^2} \qquad [28]$$

In Eq. 28, (B_0, C_0) and (B, C) represent the Racah parameter pairs for Mn^{4+} ions in free ($B_0 = 1160$ cm^{-1}, $C_0 = 4303$ cm^{-1}; Ref. 79) and in a host material, respectively.

Figure 20 shows the $E(^2E_g)_{ZPL}$ vs β_1 relation for the Mn^{4+}-activated fluoride, oxide, and oxyfluoride phosphors. The β_1 values were calculated using Eq. 28 with (B, C) listed in Tables II, IV, and V. It is found that each $E(^2E_g)_{ZPL}$ value follows the linear relation with β_1 reasonably well, given by

$$E(^2E_g)_{ZPL} = 1.900\beta_i + 0.020 \text{ eV} \qquad [29]$$

Equation 29 can, therefore, be used to predict an energy of the red emission or to check a validity of the experimentally determined Racah parameters for various kinds of Mn^{4+}-activated phosphors.

What we can notice in Fig. 20 is that the emitting ^2E_g levels in the fluorides are higher than those in the oxides, which indi-

cates a weaker nephelauxetic effect in the former phosphors, which are mostly ionic compounds if compared to the covalent oxides.[23] Brik et al.[23] also suggested that even if one considers *only* the oxides or *only* the fluorides, the degree in the Racah parameter change is different for the different representatives of the oxide or fluoride hosts. Such differences in the Racah parameters indicate that not only the nature of the ligands, but also the structural parameters, such as different interionic distances and angles between chemical bonds, may be an important factor in determining the nephelauxetic effect and, as a result, in the ^2E_g level of various phosphor materials. Further, the degree in the spectral linewidth of each emission peak should be influenced by such structural parameters in conjunction with a subtle location of the MnF$_6^{2-}$ or MnO$_6^{8-}$ octahedron in the host materials.

Effects of Temperature on PL Spectral Feature

PL spectra.—*Fluoride phosphors.*—As expected from Eq. 7, the PL intensity is strongly dependent on the lattice temperature *T*. We

Table IVc. Summary of phosphor type (O-A, O-B, or O-C), ZPL emission energy [$^2E_g = E(^2E_g)_{ZPL}$], ZPL excitation absorption energies [$^4T_{2g} = E(^4T_{2g})_{ZPL}$; $^4T_{1g,a} = E(^4T_{1g,a})_{ZPL}$], crystal-field parameter (Dq), and Racah parameters (B and C) at 300 K for some Mn^{4+}-activated oxide phosphors. Blank in a column of "Type" means no available PL spectrum at 300 K. The Racah parameters were calculated using Eqs. 11 and 12 with introducing $m = 0$ into Eqs. 22. (1 eV = 8068 cm^{-1}).

Oxide host	Type	^2E_g (eV)	$^4T_{2g}$ (eV)	$^4T_{1g,a}$ (eV)	Dq (cm^{-1})	B (cm^{-1})	C (cm^{-1})	Ref.
GdAlO$_3$	O-A	1.777	2.28	2.98	1840	530	3420	194
	O-A	1.774	2.27	2.68	1830	290	3965	90
Gd$_3$Ga$_5$O$_{12}$	O-A	1.852	2.23	2.79	1800	410	3890	102
	O-A	1.866	—	—	—	—	—	263
Gd$_3$Ga$_2$Al$_3$O$_{12}$	O-A	1.820	2.16	2.78	1745	465	3690	264
Gd$_2$MgTiO$_6$		1.821	2.34	2.90	1890	410	3815	265
Gd$_2$Sn$_2$O$_7$		1.896	2.33	2.95	1880	460	3895	97
Gd$_2$ZnTiO$_6$	O-A	1.808	2.10	2.75	1695	490	3595	103
K$_2$BaGe$_8$O$_{18}$	O-A	1.902	2.26	3.13	1825	695	3395	266
K$_2$Ge$_4$O$_9$	O-A	1.897	2.39	3.06	1930	500	3805	91
	O-A	1.897	2.39	3.06	1930	500	3805	267
K$_2$MgGeO$_4$	O-A	1.888	2.30	3.02	1855	545	3675	268
KMgLaTeO$_6$	O-A	1.780	2.07	2.90	1670	670	3135	269
KMgLaWO$_6$	O-A	1.782	2.10	2.80	1695	540	3425	270
LaAlO$_3$	O-A	1.735	2.21	2.79	1785	430	3545	194
		1.741	2.63	3.56	2120	725	2875	271
LaGaO$_3$	O-A	1.777	2.17	2.49	1750	225	4135	84
La$_3$GaGe$_5$O$_{16}$	O-A	1.880	2.38	2.93	1920	400	3990	104
LaInO$_3$		1.817	2.11	2.50	1700	280	4115	272
La$_2$LiNbO$_6$	O-C	1.783	2.26	2.85	1825	435	3655	38
La$_2$LiSbO$_6$	O-C	1.790	2.27	2.84	1830	420	3710	114
La$_2$LiTaO$_6$	O-C	1.788	2.21	2.85	1785	480	3565	115
LaMgAl$_{11}$O$_{19}$	O-A	1.875	2.41	2.97	1945	405	3955	182
La$_2$MgGeO$_6$	O-A	1.797	2.22	2.90	1790	515	3510	273
	O-A	1.799	2.36	2.92	1905	410	3755	274
La$_2$Mg$_2$SnO$_7$	O-C	1.798	2.13	2.73	1720	445	3670	116
La$_2$MgTiO$_6$	O-C	1.793	2.26	2.85	1825	435	3680	117
La$_2$ZnTiO$_6$	O-C	1.792	2.08	2.78	1680	540	3450	118
LiAlO$_2$	O-A	1.893	2.50	3.22	2015	540	3700	275
LiAlGe$_2$O$_6$	O-A	1.845	2.34	2.92	1890	425	3840	276
LiGa$_5$O$_8$			2.05	—	1655	—	—	277
LiGaGe$_2$O$_6$	O-A	1.852	2.28	2.96	1840	510	3660	276
LiGaTiO$_4$	O-A	1.856	2.16	2.84	1745	515	3665	278
Li$_2$Ge$_4$O$_9$	O-A	1.853	2.24	2.79	1805	405	3915	279
Li$_2$MgGeO$_4$	O-A	1.880	2.20	2.70	1775	365	4080	268
LiMgLaWO$_6$	O-A	1.776	2.11	2.89	1700	615	3240	280
Li$_3$Mg$_2$NbO$_6$	O-A	1.863	2.02	2.86	1630	685	3320	281
Li$_3$Mg$_2$SbO$_6$	O-A	1.894	2.19	2.77	1765	430	3965	179
	O-A	1.900	2.20	2.98	1775	610	3575	171
Li$_2$Mg$_3$SnO$_6$	O-B	(1.905)	1.98	2.99	1595	920	2975	107
Li$_2$MgTiO$_4$	O-B	(1.890)	2.03	2.83	1640	640	3485	31
	O-B	(1.892)	2.16	2.92	1745	590	3595	108
Li$_2$MgTi$_3$O$_8$	O-B	(1.809)	1.95	2.82	1575	730	3090	109
Li$_2$MgZrO$_4$	O-B	(1.912)	2.08	2.78	1680	540	3765	110
LiNaGe$_4$O$_9$	O-A	1.873	2.19	2.90	1765	540	3650	282
	O-A	1.874	2.23	2.90	1800	505	3735	283
Li$_3$RbGe$_8$O$_{18}$	O-A	1.859	2.38	2.92	1920	390	3950	284
Li$_2$SnO$_3$	O-A	1.883	2.08	2.65	1680	425	3950	92
LiSr$_3$SbO$_6$	O-A	1.880	2.23	3.05	1880	645	3440	172
Li$_2$TiO$_3$	O-A	1.823	1.89	2.61	1525	570	3470	285
Li$_2$ZnSn$_2$O$_6$	O-A	1.884	2.17	2.73	1750	410	3975	286
Lu$_3$Al$_5$O$_{12}$	O-A	1.902	2.36	2.98	1905	460	3915	85
	O-A	1.894	2.35	2.99	1895	475	3855	287
Lu$_3$Ga$_2$Al$_3$O$_{12}$	O-A	1.895	2.27	2.72	1830	320	4215	264
Lu$_2$Sn$_2$O$_7$		1.905	2.49	2.95	2010	330	4225	97

show in Fig. 21a the PL spectra at $T = 20-300$ K for K$_2$SiF$_6$:Mn^{4+} phosphor (type F1).[8] The corresponding anti-Stokes (a-S) /Stokes (S) intensity ratios, I_{a-S}/I_S, are plotted in Fig. 21b. In Fig. 21a, the ZPL peak position slightly red-shift from 20 K to 300 K. This shift was observed

to be $dE(^2E_g)_{ZPL}/dT \sim -8 \times 10^{-2}$ cm^{-1}/K, considerably smaller than the temperature shift of the fundamental energy gap dE_0/dT in various semiconductors, e.g., -3.5 cm^{-1}/K (-4.4×10^{-4} eV/K) near 300 K for GaN.[78]

Table IVd. Summary of phosphor type (O-A, O-B, or O-C), ZPL emission energy [$^2E_g = E(^2E_g)_{ZPL}$], ZPL excitation absorption energies [$^4T_{2g} = E(^4T_{2g})_{ZPL}$; $^4T_{1g,a} = E(^4T_{1g,a})_{ZPL}$], crystal-field parameter (Dq), and Racah parameters (B and C) at 300 K for some Mn^{4+}-activated oxide phosphors. Blank in a column of "Type" means no available PL spectrum at 300 K. The Racah parameters were calculated using Eqs. 11 and 12 with introducing $m = 0$ into Eqs. 22. (1 eV = 8068 cm^{-1}).

Oxide host	Type	^2E_g (eV)	$^4T_{2g}$ (eV)	$^4T_{1g,a}$ (eV)	Dq (cm^{-1})	B (cm^{-1})	C (cm^{-1})	Ref.
MgAl$_2$O$_4$	O-A	1.905	2.32	3.10	1870	600	3600	288
Mg$_4$Al$_{14}$O$_{25}$	O-A	1.890	2.60	2.95	2100	245	4385	119
Mg$_2$Al$_4$Si$_5$O$_{18}$	O-A	1.828	1.98	2.68	1595	545	3535	177
Mg$_3$Al$_2$TiO$_8*^1$	O-A	1.900	2.01	2.80	1620	635	3535	289
Mg$_6$As$_2$O$_{11}$	O-A	1.936	2.22	3.10	1790	710	3455	290
Mg$_3$Ga$_2$GeO$_8$	O-A	1.909	2.62	3.20	2115	420	4015	173
Mg$_7$Ga$_2$GeO$_{12}$	O-A	1.912	2.58	3.09	2080	365	4150	291
Mg$_2$GeO$_4$	O-A	1.928	2.54	3.22	2050	505	3870	292
	O-A	1.938	2.56	3.13	2065	415	4110	86
Mg$_4$GeO$_6$	O-A	1.928	2.54	3.12	2050	420	4060	35
	O-A	1.938	2.55	3.12	2055	415	4110	193
Mg$_{14}$Ge$_5$O$_{24}$	O-A	1.938	2.55	3.12	2055	415	4110	193
	O-A	1.924	2.55	3.15	2055	435	4015	209
	O-A	1.934	2.52	3.05	2035	380	4170	293
MgTiO$_3$	O-A	1.765	1.92	2.94	1550	955	2540	258
	O-A	1.768	1.87	2.86	1510	925	2615	294
MgTi$_2$O$_5$	O-A	1.769	1.98	2.62	1595	490	3505	294
Mg$_2$TiO$_4$	O-A	1.881	2.24	2.95	1805	540	3675	294
	O-A	1.882	2.14	2.74	1725	445	3890	289
	O-A	1.886	2.19	2.62	1765	310	4225	295
	O-A	1.885	2.23	2.67	1800	315	4205	296
Mg$_4$TiSnO$_8*^1$	O-A	1.870	1.92	2.80	1550	750	3220	289
Mg$_3$Y$_2$Ge$_3$O$_{12}$	O-A	1.933	2.72	3.38	2195	480	3930	98
MgY$_2$TiO$_6$	O-A	1.829	2.26	2.82	1825	410	3830	297
Mg$_6$ZnGa$_2$GeO$_{12}$	O-A	1.907	2.65	3.22	2140	410	4030	175

The Stokes and anti-Stokes intensities I_S and $I_{a\text{-}S}$ are given by Eq. 7. The ratio between $I_{a\text{-}S}$ and I_S can then be written as

$$\frac{I_{a\text{-}S}}{I_S} = \left(\frac{E_0 + h\nu_i}{E_0 - h\nu_i}\right)^4 \exp\left(-\frac{h\nu_i}{k_B T}\right) \qquad [30]$$

The solid lines in Fig. 21b show the results calculated using Eq. 30. Our measured anti-Stokes/Stokes ratios $I_{a\text{-}S}/I_S$ are understood to be reasonably well explained by the Maxwell–Boltzmann statistics of Eq. 8.

Figure 22a shows the temperature dependences of the PL intensities of I_S and $I_{a\text{-}S}$, together with that of the ZPL emission intensity I_{ZPL} in Rb$_2$GeF$_6$:Mn^{4+} phosphor (type F2).[122] Each emission component was obtained by integrating PL spectral peak. The inset shows the PL spectrum at $T = 300$ K. As expected, no strong temperature dependence was observed on the I_{ZPL} intensity below about 450 K. The gradual decreases in the I_S, $I_{a\text{-}S}$, and I_{ZPL} intensities vs T plots at $T \geq 450$ K come from the well-known thermal quenching phenomena (Eq. 10). The dashed lines in Fig. 22a represent the normalized luminescence intensities of the theoretically obtained Stokes and anti-Stokes components (see Eq. 7) that can be calculated from

$$I_{S,a\text{-}S}(T) = n_j(T) + \frac{1}{2} \pm \frac{1}{2} = \begin{cases} n_j(T) + 1 & (I_S) \\ n_j(T) & (I_{a\text{-}S}) \end{cases} \qquad [31]$$

with inputting $h\bar{\nu}(h\nu_j) = 31$ meV, where $\bar{\nu}$ is the appropriately weight-averaged vibration frequency used in Eq. 9. The theoretical emission intensities calculated using Eq. 31 reasonably well explain the experimental PL intensity dependence on T. However, there is a clear disagreement between the experimental data (open circles) and theoretical $I_{a\text{-}S}(T)$ curve (dashed line) at $T < 200$ K.

Optical transitions and resulting luminescence intensities are strongly influenced by the lattice vibronic quanta, especially by the optical phonons. Not only the optical phonons but also the acoustic phonons may act an important part in the usual optical transition phe-

nomena. Here, we add an acoustic phonon term, αT, to Eq. 31:[123]

$$I_{S,a\text{-}S}(T) = \begin{cases} n_j(T) + \alpha T + 1 & (I_S) \\ n_j(T) + \alpha T & (I_{a\text{-}S}) \end{cases} \qquad [32]$$

The solid lines in Fig. 22a show the results calculated using Eq. 32 with $h\bar{\nu} = 38$ meV and $\alpha = 5.0 \times 10^{-4}$ K^{-1}. An addition of the αT term to our model greatly improves the fit between the theoretical and experimental PL intensity data. Note that the acoustic phonon-related luminescence peaks are usually observed in PL spectra of various fluoride phosphors (see Refs. 8 and 124). All the calculated curves in Fig. 22a were taken into consideration the thermal quenching energy of $E_q = 0.80$ eV (see Eq. 10).

The same as Fig. 22a, but those for BaTiF$_6$:Mn^{4+} phosphor (type F1)[125] are shown in Fig. 22b. Because BaTiF$_6$:Mn^{4+} is of type F1, the ZPL emission peak was observed only in the limited temperature range ($T \leq 270$ K). The solid and dashed lines are calculated with $h\bar{\nu} = 43$ meV, $\alpha = 4.0 \times 10^{-4}$ K^{-1} (solid lines), and $\alpha = 0$ K^{-1} (dashed lines), together with considering the thermal quenching energy of $E_q = 0.80$ eV. Considering the additional acoustic phonon term (αT) and thermal quenching effect (E_q), we obtain good agreement between the theoretical and experimental temperature dependences of the Stokes and anti-Stokes PL data in the Mn^{4+}-activated fluoride phosphors over the entire temperature range from cryogenic to higher temperatures than 300 K.

Oxide phosphors.—We show in Fig. 23a the normalized PL intensities of I_S and $I_{a\text{-}S}$ vs T data, together with that of the ZPL emission intensity (I_{ZPL}) for SrLaAlO$_4$:Mn^{4+} phosphor (type O-A2).[126] The inset shows the PL spectrum at $T = 300$ K. The PL spectrum at 450 K is strongly thermally quenched. This phenomenon can be well explained by considering the thermal quenching energy of $E_q = 0.55$ eV in Eq. 10. The solid and dashed lines are calculated with $h\bar{\nu} = 55$ meV, $\alpha = 1.0 \times 10^{-4}$ K^{-1} (solid lines), and $\alpha = 0$ K^{-1} (dashed lines). By

Table IVe. Summary of phosphor type (O-A, O-B, or O-C), ZPL emission energy [$^2E_g = E(^2E_g)_{ZPL}$], ZPL excitation absorption energies [$^4T_{2g} = E(^4T_{2g})_{ZPL}$; $^4T_{1g,a} = E(^4T_{1g,a})_{ZPL}$], crystal-field parameter (Dq), and Racah parameters (B and C) at 300 K for some Mn^{4+}-activated oxide phosphors. Blank in a column of "Type" means no available PL spectrum at 300 K. The Racah parameters were calculated using Eqs. 11 and 12 with introducing $m = 0$ into Eqs. 22. (1 eV = 8068 cm^{-1}).

Oxide host	Type	^2E_g (eV)	$^4T_{2g}$ (eV)	$^4T_{1g,a}$ (eV)	Dq (cm^{-1})	B (cm^{-1})	C (cm^{-1})	Ref.
Na$_2$MgAl$_{10}$O$_{17}$	O-A	1.839	1.87	2.92	1510	1040	2600	244
NaMgGdTeO$_6$	O-A	1.785	1.83	2.85	1475	1000	2530	176
NaMgLaTeO$_6$		1.771	2.14	2.85	1725	545	3375	298
	O-A	1.777	1.96	2.86	1580	770	2935	183
NaMgLaWO$_6$	O-A	1.771	2.12	2.82	1710	535	3395	299
NZAO*^{2}	O-A	1.839	1.78	2.85	1435	1155	2425	87
Rb$_2$Ge$_4$O$_9$	O-A	1.889	2.29	2.95	1850	495	3800	91
	O-A	1.890	2.29	2.95	1850	495	3800	267
SrAl$_2$O$_4$	O-A	1.876	2.18	2.80	1760	465	3840	167
SrAl$_4$O$_7$	O-A	1.876	2.18	3.02	1760	670	3380	168
SrAl$_{12}$O$_{19}$	O-A	1.892	2.43	3.00	1960	415	3985	125
	O-A	1.887	2.31	3.00	1865	520	3735	300
Sr$_2$Al$_6$O$_{11}$	O-A	1.902	2.37	3.00	1910	465	3895	301
Sr$_4$Al$_{14}$O$_{25}$	O-A	1.904	2.36	2.88	1905	375	4110	301
	O-A	1.901	2.36	2.88	1905	375	4100	302
	O-A	1.902	2.35	2.85	1895	360	4140	105
	O-A	1.893	2.32	3.04	1870	545	3690	93
SrGe$_4$O$_9$	O-A	1.889	2.45	3.32	1975	680	3380	241
	O-A	1.889	2.47	3.27	1995	610	3525	303
	O-A	1.884	2.51	3.27	2025	575	3595	304
	O-A	1.890	2.58	3.38	2080	605	3535	305
	O-A	1.887	2.55	3.32	2055	580	3585	306
Sr$_2$Ge$_7$SiO$_{18}$	O-A	1.884	2.51	3.27	2025	575	3595	304
SrLaAlO$_4$	O-A	1.739	2.13	2.72	1720	440	3530	126
SrLaGaO$_4$	O-A	1.755	2.08	2.64	1680	415	3630	185
Sr$_2$LaNbO$_6$	O-A	1.790	2.13	2.85	1720	555	3405	307
SrLaScO$_4$	O-A	1.776	2.00	2.70	1615	545	3400	308
SrLa$_2$Sc$_2$O$_7$	O-A	1.785	1.94	2.62	1565	530	3460	189
Sr$_2$LaTaO$_6$	O-A	1.786	2.09	2.85	1685	595	3305	29
SrMgAl$_{10}$O$_{17}$	O-A	1.871	2.32	3.08	1870	580	3550	244
	O-A	1.880	2.14	2.91	1725	600	3540	309
SrMgAl$_{30}$O$_{17}$	O-A	1.887	2.29	2.90	1850	450	3890	94
Sr$_2$MgAl$_{22}$O$_{36}$	O-A	1.885	2.13	2.86	1720	565	3635	310
	O-A	1.881	2.13	2.89	1720	595	3560	311
Sr$_2$MgGe$_2$O$_7$	O-A	1.936	2.69	3.44	2170	560	3760	312
SrMgLaNbO$_6$	O-A	1.879	2.30	2.85	1855	400	3985	313
SrMgLaTaO$_6$	O-A	1.790	2.13	2.69	1720	415	3725	314
SrMg$_2$La$_2$W$_2$O$_{12}$	O-A	1.783	2.14	2.85	1725	545	3410	204
Sr$_3$NaSbO$_6$	O-A	1.820	2.00	2.74	1615	585	3430	184
	O-A	1.813	2.02	2.68	1630	505	3580	187
Sr$_3$SiAl$_{10}$O$_{20}$	O-A	1.874	2.10	2.98	1695	720	3270	26
	O-A	1.867	2.14	2.98	1725	675	3350	106
SrTiO$_3$		1.715	2.02	2.58	1630	415	3525	315
Sr$_2$TiO$_4$	O-A	1.742	1.97	2.53	1590	420	3590	195
Sr$_2$YNbO$_6$	O-A	1.823	2.27	2.87	1830	445	3740	316
Sr$_2$YSbO$_6$	O-A	1.858	2.26	2.85	1825	435	3850	248
Sr$_9$Y$_2$W$_4$O$_{24}$	O-A	1.817	2.07	2.74	1670	510	3575	206
Sr$_2$ZnMoO$_6$	O-A	1.798	2.16	2.51	1745	245	4140	317
Sr$_2$ZnWO$_6$	O-A	1.804	2.20	2.79	1775	435	3705	318

taking into consideration the acoustic phonon term (αT), an agreement between the theory and experiment becomes excellent over the entire temperature range from $T = 30$ to 480 K.

The same as Fig. 23a, but those for YAlO$_3$:Mn^{4+} oxide phosphor (type O-A1)[127] are shown in Fig. 23b. The PL spectra were examined from $T = 10$ to 440 K. The fit-determined parameters are $E_{q1} = 25$ meV, $E_{q2} = 0.70$ eV, $h\bar{\nu} = 25$ meV, $\alpha = 1.0 \times 10^{-4}$ K^{-1} (solid lines), and $\alpha = 0$ K^{-1} (dashed lines). As in the case of the fluoride phosphors, we obtain good agreement between the theoretical and experimental PL

data in the Mn^{4+}-activated oxide phosphors from cryogenic to higher temperatures than 300 K.

Oxyfluoride phosphors.—Figure 24a shows the normalized PL intensities of I_S and $I_{a\text{-}S}$ vs T data in Cs$_2$WO$_2$F$_4$:Mn^{4+} phosphor (type OF-A1).[33] The inset shows the PL spectrum at $T = 300$ K. Because of type OF-A1, no strong ZPL emission peak was observed for this phosphor even at 10 K. Beyond about 300 K, both the Stokes and anti-Stokes PL intensities decrease with increasing T. The solid and dashed

Table IVf. Summary of phosphor type (O-A, O-B, or O-C), ZPL emission energy [$^2E_g = E(^2E_g)_{ZPL}$], ZPL excitation absorption energies [$^4T_{2g} = E(^4T_{2g})_{ZPL}$; $^4T_{1g,a} = E(^4T_{1g,a})_{ZPL}$], crystal-field parameter (Dq), and Racah parameters (B and C) at 300 K for some Mn^{4+}-activated oxide phosphors. Blank in a column of "Type" means no available PL spectrum at 300 K. The Racah parameters were calculated using Eqs. 11 and 12 with introducing $m = 0$ into Eqs. 22. (1 eV = 8068 cm^{-1}).

Oxide host	Type	^2E_g (eV)	$^4T_{2g}$ (eV)	$^4T_{1g,a}$ (eV)	Dq (cm^{-1})	B (cm^{-1})	C (cm^{-1})	Ref.
YAlO$_3$	O-A	1.785	2.28	2.80	1840	375	3790	127
Y$_3$Al$_5$O$_{12}$	O-A	1.893	2.24	2.82	1805	425	3960	264
	O-A	1.904	2.35	2.85	1895	360	4145	287
Y$_3$Ga$_5$O$_{12}$	O-A	1.879	2.18	2.80	1760	465	3845	264
Y$_3$Ga$_2$Al$_3$O$_{12}$	O-A	1.883	2.21	2.60	1785	275	4290	264
Y$_2$Sn$_2$O$_7$		1.908	2.39	2.86	1930	335	4210	97
		1.913	2.38	2.86	1920	345	4205	319
Y$_2$Ti$_2$O$_7$		—	2.23	2.65	1800	—	—	319
YbAlO$_3$	O-A	1.833	2.35	2.95	1895	440	3770	320
ZnGa$_2$O$_4$	O-A	1.915	2.40	2.97	1935	415	4045	211
Zn$_2$TiO$_4$		1.833	2.26	2.78	1825	380	3920	321

[*1] Spinel-type solid solution.
[*2] Na$_{1.57}$Zn$_{0.57}$Al$_{10.43}$O$_{17}$.

lines in Fig. 24a are calculated with $h\bar{v} = 20$ meV, $\alpha = 3.0 \times 10^{-4}$ K^{-1} (solid lines), and $\alpha = 0$ K^{-1} (dashed lines). The thermally quenched PL intensities are well explained by considering $E_{q1} = 20$ meV and $E_{q2} = 0.58$ eV in Eq. 10.

The same as Fig. 24a, but those for MFG:Mn^{4+} phosphor (type OF-B)[35] are shown in Fig. 24b. The PL spectra were measured from $T = 10$ to 720 K. The theoretical curves are calculated with $h\bar{v} = 80$ meV, $\alpha = 3.0 \times 10^{-4}$ K^{-1} (solid lines), and $\alpha = 0$ K^{-1} (dashed lines). The thermal quenching energies are determined to be $E_{q1} = 55$ meV and $E_{q2} = 0.75$ eV. As in the fluoride and oxide phosphors (Figs. 22 and 23), we obtain good agreement between the theoretical and experimental $I_S(T)$ and $I_{a-S}(T)$ curves in the oxyfluoride phosphors with considering the acoustic phonon and thermal quenching terms in our calculation model over the wide temperature range from cryogenic to higher temperatures than 300 K. The overall luminescence intensity vs T data for the Mn^{4+}-activated fluoride, oxide, and oxyfluoride phosphors will be presented in the next section.

PL decay characteristics.—*Fluoride phosphors.—*Figure 25a shows our measured room-temperature PL decay curves for the Ce^{3+} emission in (Ce^{3+}, Mn^{2+})-codoped CaCO$_3$ phosphor[128] and that in KCl:Ce^{3+} phosphor.[129] Figure 25b also shows the room-temperature PL decay curves for the Mn^{2+} emission in (Ce^{3+}, Mn^{2+})-codoped CaCO$_3$ phosphor[128] and that for the Mn^{4+} emission in BaSiF$_6$:Mn^{4+} phosphor.[52] It should be noted that the $5d_1 \rightarrow 4f_1$ transitions in Ce^{3+} are dipole allowed, whereas the intra-d-shell transitions in Mn^{2+} and

Table V. Summary of phosphor type (OF-A1, OF-A2, OF-B, HF, or AB), ZPL emission energy [$^2E_g = E(^2E_g)_{ZPL}$], ZPL excitation absorption energies [$^4T_{2g} = E(^4T_{2g})_{ZPL}$; $^4T_{1g,a} = E(^4T_{1g,a})_{ZPL}$], crystal-field parameter (Dq), and Racah parameters (B and C) at 300 K for some Mn^{4+}-activated oxyfluoride and some fluorine compound phosphors. The Racah parameters were calculated using Eqs. 11 and 12 with introducing $m = 0$ (types OF-A1, OF-A2, HF, and AB) or $m = 5$ (type OF-B) into Eqs. 22. (1 eV = 8068 cm^{-1}).

| Oxyfluoride host	Type	^2E_g (eV)	$^4T_{2g}$ (eV)	$^4T_{1g,a}$ (eV)	Dq (cm^{-1})	B (cm^{-1})	C (cm^{-1})	Ref.
BaNbOF$_5$	OF-B	1.971	2.17	2.86	1750	525	3950	322
BaTiOF$_4$	OF-A1	1.990	2.38	2.88	1920	640	3735	323
Cs$_2$NbOF$_5$	OF-A1	1.990	2.20	2.70	1775	655	3720	324
	OF-A1	1.987	2.32	2.78	1870	605	3805	192
Cs$_2$WO$_2$F$_4$	OF-A1	1. 989	2.37	2.83	1910	600	3815	33
K$_3$HF$_2$WO$_2$F$_4$	OF-A2	2.006	2.28	2.72	1840	590	3895	196
K$_3$TaO$_2$F$_4$	OF-A2	2.002	2.39	2.83	1930	585	3890	325
LiAl$_4$O$_6$F	OF-B	1.872	2.12	3.13	1710	880	2945	190
MFG[*1]	OF-B	1.928	2.54	3.12	2050	420	4060	35
	OF-B	1.927	2.54	3.10	2050	405	4095	326
	OF-B	1.930	2.48	2.85	2000	260	4455	327
	OF-B	1.938	2.49	3.01	2010	375	4200	193
	OF-B	1.930	2.48	3.01	2000	380	4160	328
Na$_2$WO$_2$F$_4$	OF-A2	2.002	2.47	3.02	1995	680	3670	329
	OF-A2	2.002	2.42	2.88	1950	600	3855	34
Rb$_2$NbOF$_5$	OF-A1	1.992	2.39	2.79	1930	545	3945	330
Rb$_5$Nb$_3$OF$_{18}$	OF-A1	1.989	2.39	2.78	1930	540	3960	331
Sr$_2$ScO$_3$F	OF-B	1.810	2.03	2.73	1640	540	3490	195
BaNb(OH)$_{1.5}$F$_{5.5}$	HF (F2)	1.975	2.26	2.75	1825	640	3705	36
NaHF$_2$	AB (F2)	2.010	2.45	2.92	1975	605	3855	37

[*1] MFG = magnesium fluorogermanate.
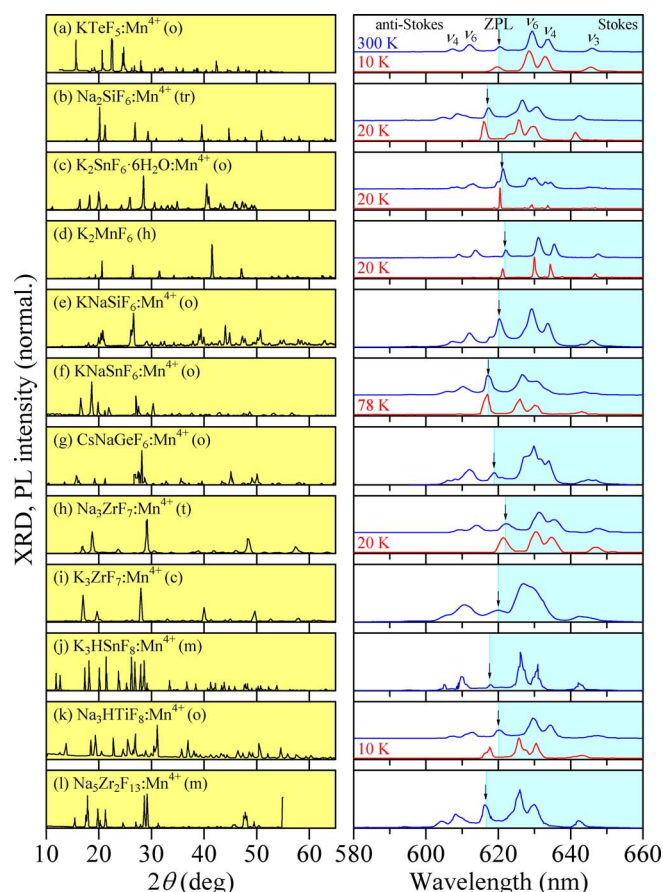
Figure 9. XRD patterns and PL spectra measured at 300 K of some fluoride phosphors of type F2 ($I_x-IV_y-F_{x+4y}$).[20,61−71] If cryogenic-temperature PL spectrum is available, its spectrum is also plotted in the lower part of each figure. The crystal class of each host material is given in the parenthesis following after the phosphor name (Table III). The vertical arrow on the right-hand side of each figure shows the position of the $E(^2E_g)_{ZPL}$ emission energy (ZPL).
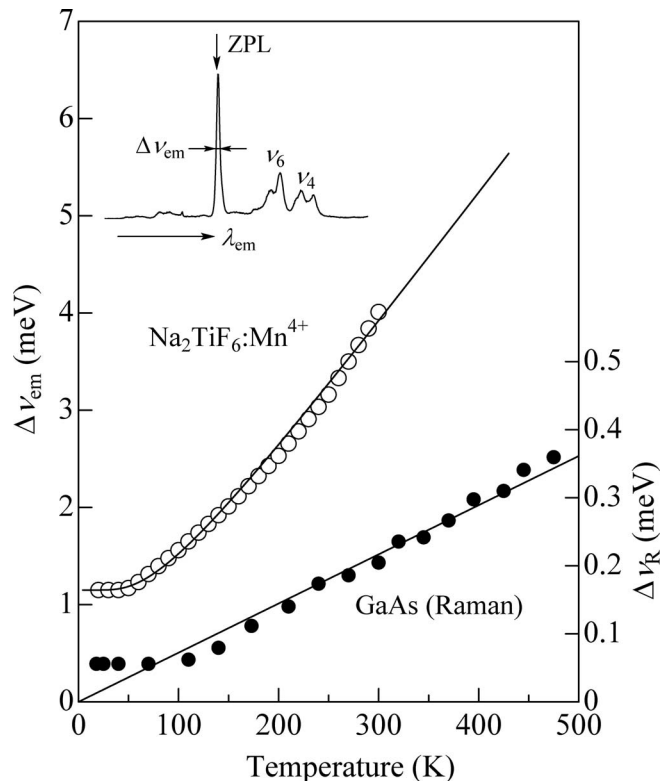

Figure 10. XRD patterns and PL spectra measured at 300 K of some fluoride phosphors of type F2 ($I_x-V_y-F_{x+5y}$, $II_x-III_y-F_{2x+3y}$, and $II_x-IV_y-F_{2x+4y}$).[72−76] The crystal class of each host material is given in the parenthesis following after the phosphor name (Table III). The vertical arrow on the right-hand side of each figure shows the position of the $E(^2E_g)_{ZPL}$ emission energy (ZPL).

Mn^{4+} are dipole forbidden. It is easy to expect a quick response of the core electrons in the allowed transitions, but not in the forbidden ones. As a result, the Ce^{3+} emission can be observed in a time scale of very fast, i.e., in the nanoseconds region, which is in direct contrast to the dipole-forbidden Mn^{2+} and Mn^{4+} transitions in a very slow time scale, i.e., in the milliseconds region in Fig. 25b.

The PL decay curve sometimes shows a non-exponential decay characteristic, which can be fitted to the following multiple-exponential expression:

$$I(t) = \sum_{i=1}^{n} a_i \exp\left(-\frac{t}{\tau_i}\right) \quad [33]$$

with $\sum a_i = 1.0$. The fit-determined decay parameters for the Ce^{3+} emission in CaCO$_3$:Ce^{3+}, Mn^{2+} in Fig. 25a are $a_1 = 0.84$, $\tau_1 = 1.8$ ns, $a_2 = 0.16$, and $\tau_2 = 20$ ns ($i = 1, 2$), while those for the Mn^{2+} emission in Fig. 25b are $a_1 = 0.80$, $\tau_1 = 5.0$ ms, $a_2 = 0.20$, and $\tau_2 = 28$ ms ($i = 1, 2$). The average decay time τ_{av} exhibiting such a multiple-exponential decay behavior can be defined by

$$\tau_{av} = \frac{\sum_i a_i \tau_i^2}{\sum_i a_i \tau_i} \quad [34]$$

The corresponding τ_{av} values for the Ce^{3+} and Mn^{2+} emissions in CaCO$_3$:Ce^{3+}, Mn^{2+} (Fig. 25) are, respectively, $\tau_{av} \sim 14$ ns and ~ 18 ms. Note that the Ce^{3+} emission in KCl:Ce^{3+} and the Mn^{4+} emission in BaSiF$_6$:Mn^{4+} can be reasonably well fitted with the single-

Figure 11. Spectral linewidth $\Delta\nu_{em}$ for the ZPL emission peak vs temperature T data in the Na$_2$TiF$_6$:Mn^{4+} fluoride phosphor. The experimental data are taken from Ref. 50. The solid line shows the result calculated using Eq. 24. For comparison, the Raman transverse-optical phonon linewidth ($\Delta\nu_R$) vs T data for GaAs reported by Chang et al.[77] are also plotted.
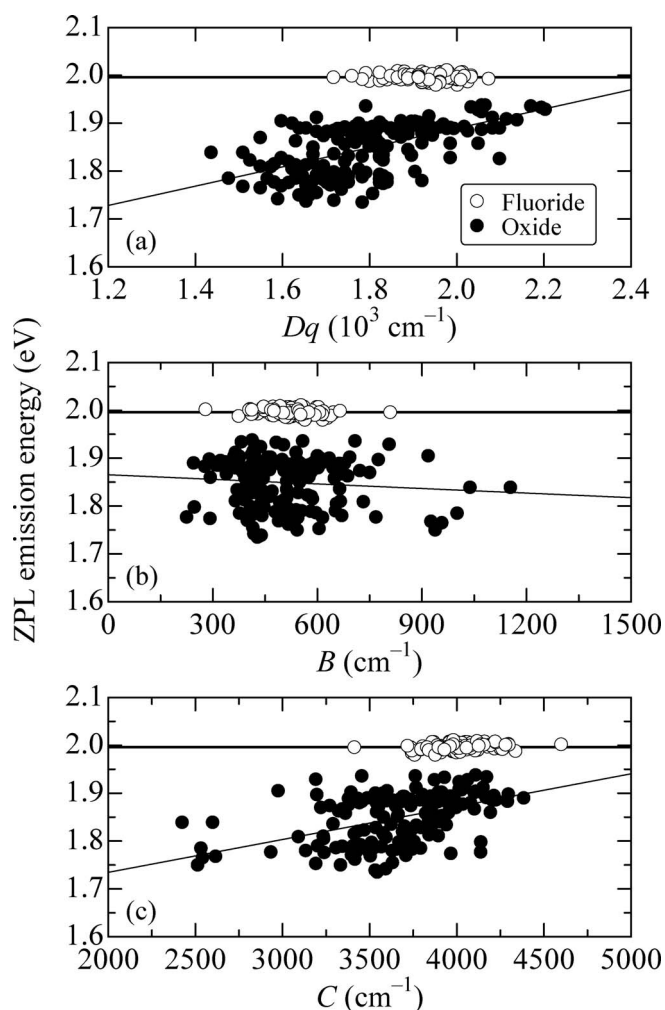
Figure 12. Room-temperature ZPL emission energy $[^2E_g = E(^2E_g)_{ZPL}]$ vs crystal-field (Dq) and Racah parameters (B and C) for various Mn^{4+}-activated fluoride and oxide phosphors. The numeric values are taken from lists in Tables II and IV. The heavy solid lines indicate no strong dependence of ^2E_g on Dq, B, or C, expressed by $^2E_g = 1.996 \pm 0.020$ eV (fluoride), whereas the thin solid lines in (a)–(c) show the least-squares fit results represented by Eqs. 25–27, respectively (oxide).

Figure 13. XRD patterns and PL spectra measured at 300 K of some oxide phosphors of type O-A1.[29,82–87] The crystal class of each host material is given in the parenthesis following after the phosphor name. The vertical arrow on the right-hand side of each figure shows the position of the $E(^2E_g)_{ZPL}$ emission energy (ZPL). Some important parameters of these phosphors are listed in Table IV. NZAO:$Mn^{4+} = Na_{1.57}Zn_{0.57}Al_{10.43}O_{17}$:$Mn^{4+}$.

exponential function by inputting $a_1 = 1.0$, $\tau_1 = 20$ ns (Ce^{3+} emission) and $a_1 = 1.0$, $\tau_1 = 6.5$ ms (Mn^{4+} emission) into Eq. 33 ($i = 1$ only).

Figure 26a shows the temperature evolution of the integrated PL intensity (I_{PL}) in K_2SiF_6:Mn^{4+} phosphor from $T = 20$ to 450 K.[20] The PL decay time τ vs T data for the same phosphor is also shown in Fig. 26b.[20] The solid line in Fig. 26a represents the theoretical I_{PL} vs T curve calculated using a modified version of Eq. 10 with considering the αT term in Eq. 32

$$I_{PL}(T) = \frac{I_0}{1 + \sum_i a_i \exp(-E_{qi}/k_BT)} \left(1 + \frac{2}{\exp(h\bar{\nu}/k_BT) - 1} + 2\alpha T\right)$$

[35]

The fit-determined parameters are $I_0 = 1.0$, $a_1 = 2.5 \times 10^{-1}$, $E_{q1} = 25$ meV, $a_2 = 5.0 \times 10^5$, $E_{q2} = 0.45$ eV, $h\bar{\nu} = 65$ meV, and $\alpha = 2.0 \times 10^{-4}$ K^{-1}.

The solid line in Fig. 26b shows the decay time τ vs T curve calculated using

$$\tau(T) = \frac{\tau_0}{1 + \sum_i b_i \exp(-E_{qi}/k_BT)}$$

[36]

Equation 36 assumes that the PL decay process is caused only by the thermal quenching mechanism. The fit-determined parameters in Fig. 26b are $\tau_0 = 15.5$ ms, $b_1 = 2.5$, $E_{q1} = 25$ meV, $b_2 = 1.0 \times 10^7$, and $E_{q2} = 0.45$ eV. The dashed line in Fig. 26b also shows the result calculated using Eq. 36 with $b_1 = 0$, i.e., neglecting the $i = 1$ term. The thermal quenching energies for $I_{PL}(T)$ are the same as those for $\tau(T)$, promising that both $I_{PL}(T)$ and $\tau(T)$ are influenced by the same thermal quenching process in the intra-d-shell (Mn^{4+}) transitions.

The dependence of decay lifetime τ on T can be well fitted using Eq. 36. The $^2E_g \rightarrow {}^4A_{2g}$ luminescence decay formula for Mn^{4+} can be theoretically written as[130]

$$\frac{1}{\tau} = \frac{1}{\tau_E} + \frac{1}{\tau_T} \exp\left(-\frac{\Delta E}{k_BT}\right)$$

[37]

where τ_E and τ_T represent the radiative lifetimes of ^2E_g and $^4T_{2g}$ states, respectively. τ_E is long in comparison to τ_T because the doublet–quartet transition is spin-forbidden. ΔE is the difference in energy between the $^4T_{2g}$ and ^2E_g excited states. From Eq. 37, we obtain

$$\tau = \frac{\tau_E}{1 + \left(\frac{\tau_E}{\tau_T}\right) \exp\left(-\frac{\Delta E}{k_BT}\right)}$$

[38]

Comparing Eq. 36 with Eq. 38, we obtain $\tau_0 = \tau_E$, $b_2 = \tau_E/\tau_T$, and $E_{q2} = \Delta E$ with $b_1 = 0$. From Fig. 26b, we obtain $\Delta E \sim 0.45$ eV. This value is in exact agreement with that determined in Fig. 26a ($E_{q2} = 0.45$ eV).
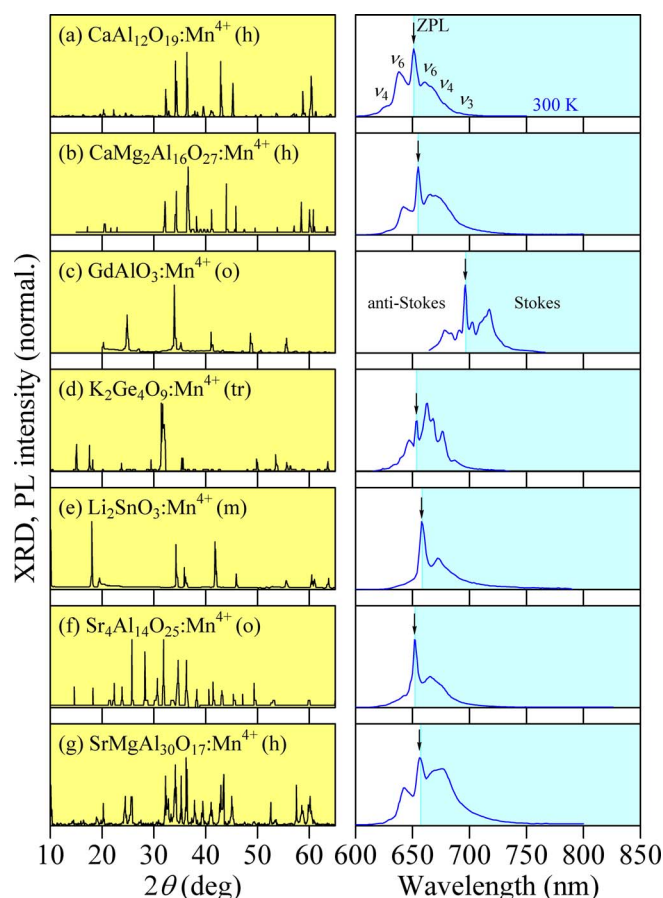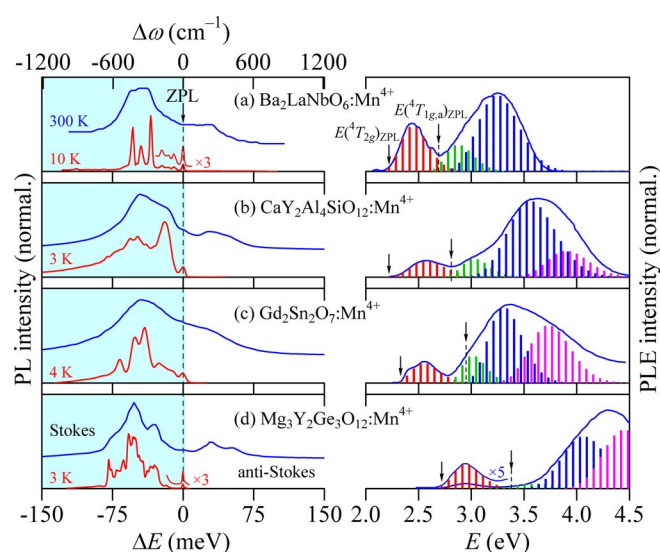
Figure 14. XRD patterns and PL spectra measured at 300 K of some oxide phosphors of type O-A2.[88–94] The crystal class of each host material is given in the parenthesis following after the phosphor name. The vertical arrow on the right-hand side of each figure shows the position of the $E(^2E_g)_{ZPL}$ emission energy (ZPL). Some important parameters of these phosphors are listed in Table IV.

Figure 16. Room- and cryogenic-temperature PL spectra, together with the room-temperature PLE spectra, of some oxide phosphors of type O-A2.[99–106] The vertical bars in each PLE spectrum show the theoretical fits using Eq. 4. The vertical arrows in each figure also show the positions of $E(^2E_g)_{ZPL}$ (PL), $E(^4T_{2g})_{ZPL}$, and $E(^4T_{1g,a})_{ZPL}$ (PLE). Some important parameters of these phosphors are listed in Table IV.

Figure 15. Room- and cryogenic-temperature PL spectra, together with the room-temperature PLE spectra, of some oxide phosphors of type O-A1.[95–98] The vertical bars in each PLE spectrum show the theoretical fits using Eq. 4. The vertical arrows in each figure also show the positions of $E(^2E_g)_{ZPL}$ (PL), $E(^4T_{2g})_{ZPL}$, and $E(^4T_{1g,a})_{ZPL}$ (PLE). Some important parameters of these phosphors are listed in Table IV.
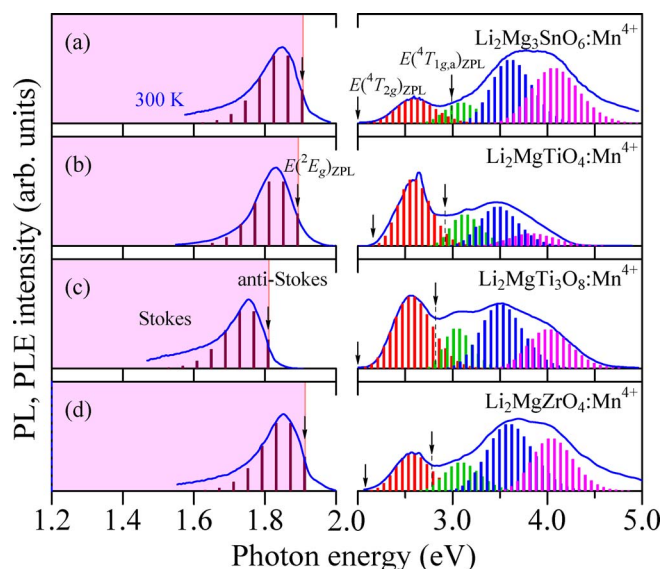
Figure 17. Room-temperature PL and PLE spectra of some oxide phosphors of type O-B.[107–110] The vertical bars in the PL and PLE spectra show the theoretical fits using Eqs. 6 and 4, respectively. The vertical arrows in each figure also show the positions of $E(^2E_g)_{ZPL}$ (PL), $E(^4T_{2g})_{ZPL}$, and $E(^4T_{1g,a})_{ZPL}$ (PLE). Some important parameters of these phosphors are listed in Table IV.
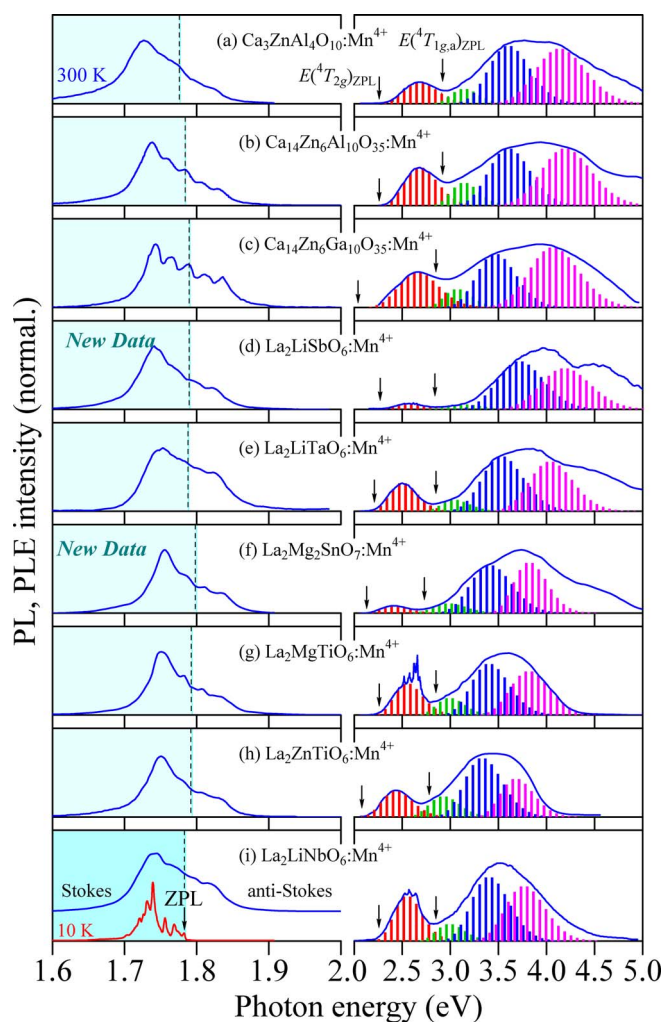
Figure 18. Room-temperature PL and PLE spectra of some oxide phosphors of type O-C.[38,111–118] The vertical bars in each PLE spectrum show the theoretical fits using Eq. 4. The vertical dashed lines in the left-hand side of each figure indicate the positions of $E(^2E_g)_{ZPL}$. The vertical arrows in the right-hand side of each figure also show the positions of $E(^4T_{2g})_{ZPL}$ and $E(^4T_{1g,a})_{ZPL}$. Some important parameters of these phosphors are listed in Table IV.

Figure 19. Room-temperature ZPL emission energy [$^2E_g = E(^2E_g)_{ZPL}$] vs crystal-field (Dq) and Racah parameters (B and C) for various Mn^{4+}-activated oxyfluoride phosphors together with those for $BaNb(OH)_{1.5}F_{5.5}:Mn^{4+}$ (type HF) and $NaHF_2:Mn^{4+}$ (type AB). The experimental data of types OF-A and OF-B are plotted by the open and solid circles, respectively. Since the PL spectral features of $BaNb(OH)_{1.5}F_{5.5}:Mn^{4+}$ and $NaHF_2:Mn^{4+}$ are very similar to those of type OF-A (or type F2), they are regarded as phosphors of type OF-A in the present plots. The numeric values are taken from a list in Table V. The heavy solid lines in (a) − (c) for the fluoride phosphors show a constant value of $E(^2E_g)_{ZPL}$ (Fig. 12), whereas the thin solid lines for the oxide phosphors in (a)–(c) represent the least-squares fit results given by Eqs. 25−27, respectively.
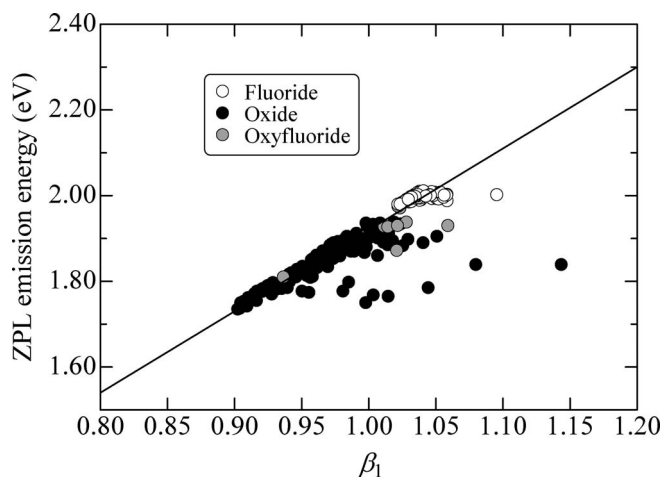
The experimental I_{PL} and τ vs T data for $K_2TiF_6:Mn^{4+}$ phosphor obtained by Senden et al.[131] are plotted in Figs. 26c and 26d. As in Figs. 26a and 26b, the I_{PL} data gradually increase with increasing T above ∼200 K, showing a peak at ∼400 K, and decrease with the further increase of T due to the usual thermal quenching phenomenon. An increase in I_{PL} at $T > 200$ K is caused by gaining of the spin-forbidden electron transitions in Mn^{4+}, expressed as Eq. 32. The solid lines in Figs. 26c and 26d are calculated using Eqs. 35 and 36 with $I_0 = 1.0$, $a_1 = 3.0 \times 10^{-1}$, $E_{q1} = 35$ meV, $a_2 = 9.0 \times 10^4$, $E_{q2} = 0.45$ eV, $h\bar{v} = 43$ meV, and $\alpha = 1.75 \times 10^{-4}$ K^{-1} (I_{PL}); $\tau_0 = 12.2$ ms, $b_1 = 4.5$, $E_{q1} = 35$ meV, $b_2 = 4.0 \times 10^5$, and $E_{q2} = 0.45$ eV (τ), respectively. The thermal quenching energies determined for $I_{PL}(T)$ are the same as those for $\tau(T)$. No clear difference in the PL decay characteristics can also be observed for phosphors of types F1 and F2.

Oxide phosphors.—$La_2LiNbO_6:Mn^{4+}$ is of type O-C. Figures 27a and 27b show the I_{PL} and τ vs T data for $La_2LiNbO_6:Mn^{4+}$ phosphor, respectively.[38] The solid lines are calculated using Eqs. 35 and 36 with $I_0 = 1.0$, $a_1 = 2.0 \times 10^{-1}$, $E_{q1} = 18$ meV, $a_2 = 1.0 \times 10^4$, $E_{q2} = 0.30$ eV, $h\bar{v} = 60$ meV, and $\alpha = 2.0 \times 10^{-4}$ K^{-1} (I_{PL}); $\tau_0 = 4.4$ ms, $b_1 = 2.0$, $E_{q1} = 18$ meV, $b_2 = 2.0 \times 10^4$, and $E_{q2} = 0.30$ eV (τ). Again, we obtain an agreement in the thermal quenching energies between

Figure 20. Room-temperature ZPL emission energy, $E(^2E_g)_{ZPL}$, vs β_1 for various fluoride, oxide, oxyfluoride, and some fluorine compound phosphors. The β_1 values are calculated using Eq. 28 with the numeric B and C values listed in Tables II, IV, and V. The solid line shows a tendency given by Eq. 29.
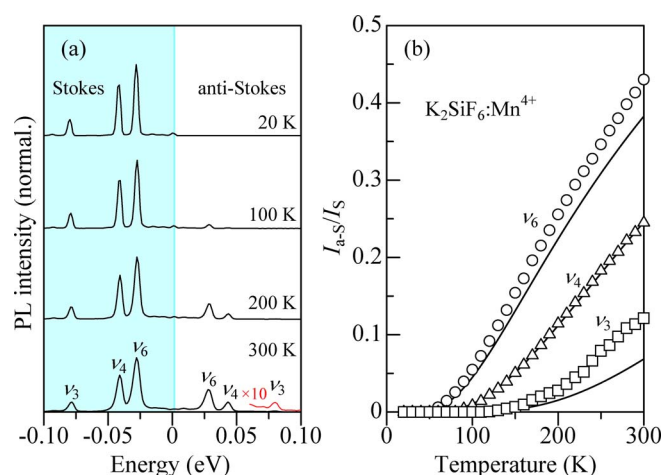
Figure 21. (a) Stokes and anti-Stokes PL lines in the $K_2SiF_6:Mn^{4+}$ fluoride phosphor at $T = 20$, 100, 200 and 300 K.[8] (b) Ratio of anti-Stokes/Stokes intensities vs temperature T data for $K_2SiF_6:Mn^{4+}$.[8] The solid lines in (b) represent the results calculated using Eq. 30.

those for $I_{PL}(T)$ and $\tau(T)$. The dashed line in Fig. 27b is calculated without considering the lower quenching energy term, i.e., assuming $b_1 = 0$. An importance of this quenching term is evident especially at temperatures below 300 K.

The same as in Figs. 27a and 27b, but those for type O-A phosphor $SrLaAlO_4:Mn^{4+}$ Ref. 126 are shown in Figs. 27c and 27d, respectively.
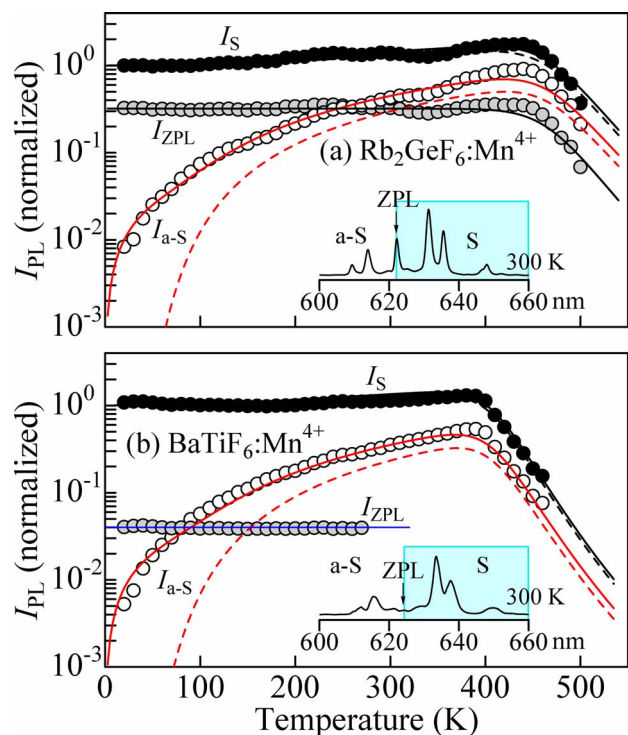
Figure 22. Integrated PL intensities for the Stokes (I_S), anti-Stokes ($I_{a\text{-}S}$), and ZPL emission components (I_{ZPL}) vs T plots for (a) the $Rb_2GeF_6:Mn^{4+}$ (type F2) and (b) $BaTiF_6:Mn^{4+}$ fluoride phosphors (type F1). The inset in each figure shows the PL spectrum measured at room temperature (S = Stokes; a-S = anti-Stokes). The experimental data in (a) and (b) are taken from Refs. 122 and 125, respectively. The solid and dashed lines represent the results calculated with (Eq. 32) and without considering the acoustic phonon contribution (Eq. 31), respectively. Note that the solid and dashed lines for the I_S component nearly completely coincide with each other.
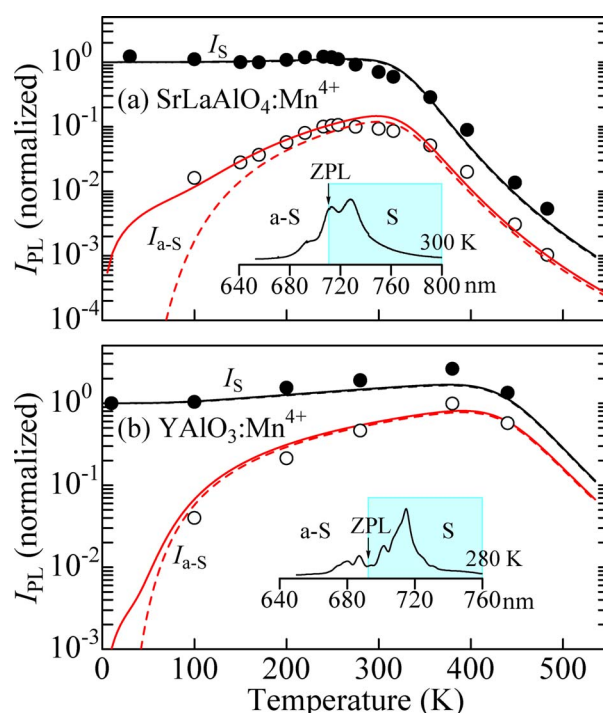
Figure 23. Integrated PL intensities for the Stokes (I_S) and anti-Stokes components ($I_{a\text{-}S}$) vs T plots for (a) the $SrLaAlO_4:Mn^{4+}$ (type O-A2) and (b) $YAlO_3:Mn^{4+}$ oxide phosphors (type O-A1). The inset in each figure shows the PL spectrum measured at room temperature (S = Stokes; a-S = anti-Stokes). The experimental data in (a) and (b) are taken from Refs. 126 and 127, respectively. The solid and dashed lines represent the results calculated with (Eq. 32) and without considering the acoustic phonon contribution (Eq. 31), respectively. Note that the solid and dashed lines for the I_S component nearly completely coincide with each other.

The gradual decreases in $\tau(T)$ at $T > 50$ K are observed in Fig. 27b. However, no such gradual decrease in $\tau(T)$ near 300 K has been observed in Fig. 27d. The best-fit parameters for $SrLaAlO_4:Mn^{4+}$ are $I_0 = 1.0$, $a_1 = 0$ ($E_{q1} = 0$ meV), $a_2 = 3.0 \times 10^8$, $E_{q2} = 0.55$ eV, $h\bar{v} = 55$ meV, and $\alpha = 1.0 \times 10^{-4}$ K^{-1} (I_{PL}); $\tau_0 = 0.84$ ms, $b_1 = 0$ ($E_{q1} = 0$ meV), $b_2 = 2.0 \times 10^7$, and $E_{q2} = 0.55$ eV (τ). An extremely large increase in I_{PL} was also observed in $YAlO_3:Mn^{4+}$ near 300 K (not shown).[127] This increase in I_{PL} was successfully explained using Eq. 35 with $I_0 = 1.0$, $a_1 = 1.0 \times 10^{-1}$, $E_{q1} = 25$ meV, $a_2 = 1.5 \times 10^5$, $E_{q2} = 0.70$ eV, $h\bar{v} = 25$ meV, and $\alpha = 1.0 \times 10^{-4}$ K^{-1}. The corresponding τ vs T plots were fitted very well with Eq. 36 by inputting $\tau_0 = 5.2$ ms, $b_1 = 2.0$, $E_{q1} = 25$ meV, $b_2 = 6.0 \times 10^8$, and $E_{q2} = 0.70$ eV.

Note that τ_0 in Eq. 36 is a decay time constant disturbed only by the temperature-independent events arising, e.g., from impurity/lattice defect scattering, but not from any scattering events with lattice vibrations or phonons. Because of the relatively small value of $\tau_0 = 0.84$ ms in $SrLaAlO_4:Mn^{4+}$, its PL decay process should be mainly due to lifetime broadening caused by the temperature-independent scattering events like impurity and/or lattice-defect scattering (i.e., a small energy quenching event of E_{q1} will be masked by a strong temperature-independent broadening at or near 300 K). At high temperatures well above 300 K, the thermal quenching becomes dominant and promises giving a large E_{q2} value of ~ 0.55 eV in Figs. 27c and 27d.

Further, we can understand that τ_0 values in the fluoride phosphors are usually larger than those in the oxide phosphors [cf. Figs. 26b and 26d (fluoride phosphors) and Figs. 27b and 27d (oxide phosphors)]. This fact may indicate that the former phosphors have more efficient "radiative" recombination pass of Mn^{4+} in the luminescence process.
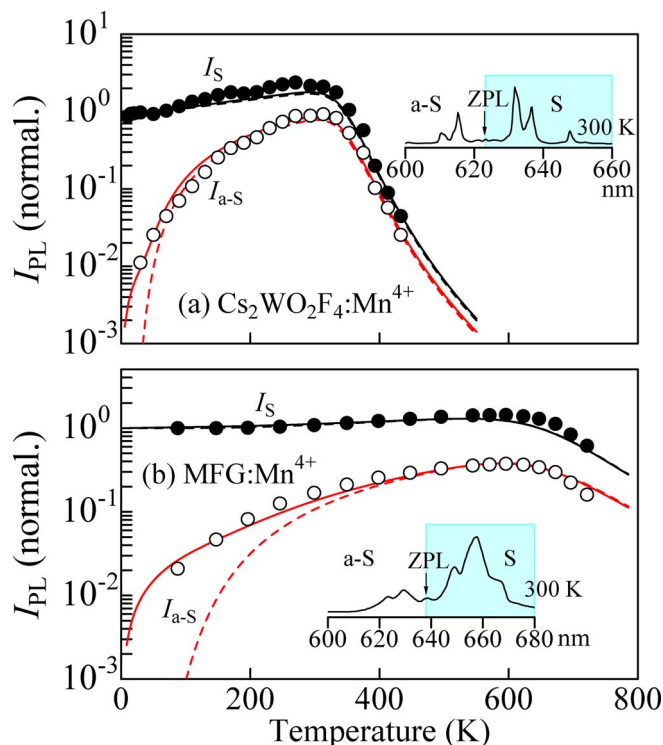
Figure 24. Integrated PL intensities for the Stokes (I_S) and anti-Stokes components (I_{a-S}) vs T plots for (a) the Cs$_2$WO$_2$F$_4$:Mn^{4+} (type OF-A1) and (b) MFG:Mn^{4+} oxyfluoride phosphors (type OF-B). The inset in each figure shows the PL spectrum measured at room temperature (S = Stokes; a-S = anti-Stokes). The experimental data in (a) and (b) are taken from Refs. 33 and 35, respectively. The solid and dashed lines represent the results calculated with (Eq. 32) and without considering the acoustic phonon contribution (Eq. 31), respectively. Note that the solid and dashed lines for the I_S component nearly completely coincide with each other.

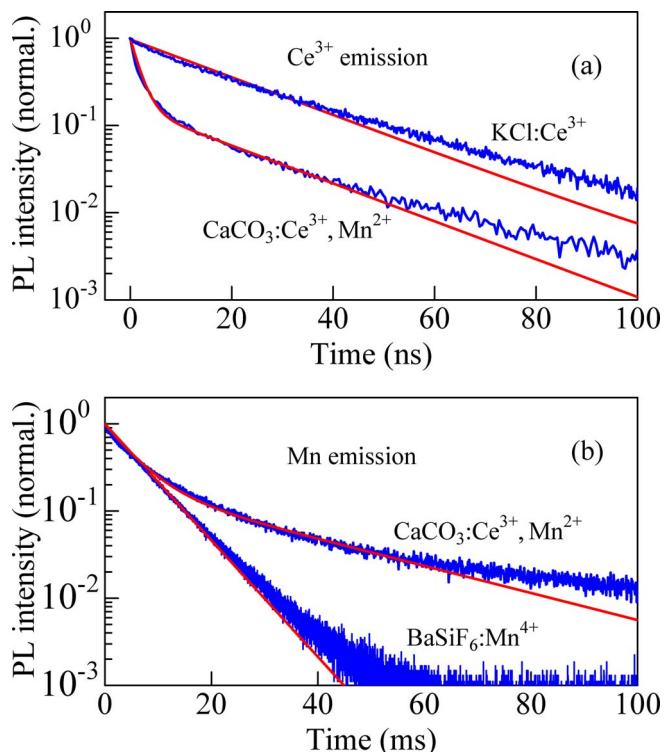**Figure 25.** (a) Room-temperature PL decay curves for the Ce^{3+} emission in (Ce^{3+}, Mn^{2+})-codoped CaCO$_3$ (Ref. 128) and that in KCl:Ce^{3+} (Ref. 129). (b) Room-temperature PL decay curves for the Mn^{2+} emission in (Ce^{3+}, Mn^{2+})-codoped CaCO$_3$ (Ref. 128) and that for the Mn^{4+} emission in BaSiF$_6$:Mn^{4+} (Ref. 52). The solid lines in (a) and (b) show the results calculated using Eq. 33. Note the difference in time scale on the horizontal axis "ns" in (a) and "ms" in (b).

Oxyfluoride phosphors.—Figure 28 shows the temperature dependences of I_{PL} and τ for oxyfluoride phosphors of types OF-A [Cs$_2$WO$_2$F$_4$:Mn^{4+} (Figs. 28a and 28b); Ref. 33] and OF-B [MFG:Mn^{4+} (Figs. 28c and 28d); Refs. 35 and 132]. The plots in these figures are very similar with each other. The decay times of the fluoride-like phosphor Cs$_2$WO$_2$F$_4$:Mn^{4+} (~ 8 ms) are larger than those of the oxide-like phosphor MFG:Mn^{4+} (~ 6 ms). This tendency is the same as those observed in Figs. 26 and 27. The fit-determined parameter values are $I_0 = 1.0$, $a_1 = 1.0 \times 10^{-2}$, $E_{q1} = 20$ meV, $a_2 = 1.5 \times 10^8$, $E_{q2} = 0.58$ eV, $h\bar{v} = 20$ meV, and $\alpha = 3.0 \times 10^{-4}$ K^{-1} (I_{PL}); $\tau_0 = 7.6$ ms, $b_1 = 1.6$, $E_{q1} = 20$ meV, $b_2 = 1.0 \times 10^9$, and $E_{q2} = 0.58$ eV (τ) for Cs$_2$WO$_2$F$_4$:Mn^{4+} (Figs. 28a and 28b) and $I_0 = 1.0$, $a_1 = 1.0 \times 10^{-2}$, $E_{q1} = 55$ meV, $a_2 = 2.0 \times 10^5$, $E_{q2} = 0.75$ eV, $h\bar{v} = 80$ meV, and $\alpha = 3.0 \times 10^{-4}$ K^{-1} (I_{PL}); $\tau_0 = 5.8$ ms, $b_1 = 4.5$, $E_{q1} = 55$ meV, $b_2 = 1.5 \times 10^5$, and $E_{q2} = 0.75$ eV (τ) for MFG:Mn^{4+} (Figs. 28c and 28d).

In conclusion of this Section, Eqs. 35 and 36 are found to be good formulations for the explanations of I_{PL} and τ vs T data over the wide temperature range from cryogenic to higher temperatures than 300 K, regardless of a kind of phosphors like fluorides, oxides, or oxyfluorides. Furthermore, there is a tendency that the PL decay times are larger in fluoride phosphors than in oxide or oxyfluoride phosphors.

Effects of Pressure on PL Spectral Feature

PL spectra.—*Fluoride phosphors.*—*Pressure-induced PL spectral change.*—The hydrostatic pressure effects of the red emission from Mn^{4+}-activated fluoride phosphors have been studied by several authors.[25,133,134] In Fig. 29, we show the hydrostatic pressure dependence of the Mn^{4+} emission energy for KNaSiF$_6$:Mn^{4+} (type F2),[25]

K$_2$SiF$_6$:Mn^{4+} (type F1),[133] and BaTiF$_6$:Mn^{4+} (type F1)[134] at room temperature, together with that of the excitation absorption transitions in KNaSiF$_6$:Mn^{4+}.[25] The pressure derivatives of these transition energies are listed in Table VI. In contrast to the PL energies, the PLE energies in Fig. 29a exhibited a blueshift with increasing pressure p. Their pressure derivatives are much larger than those for the PL energies (Table VI).

Jin et al.[25] observed in KNaSiF$_6$:Mn^{4+} that increasing p resulted in a decrease of the lattice constants, i.e., a linear decrease of a and c and a quadratic decrease of b. This fact indicates that the lattice distortion is more serious at higher pressures. As a result, they observed an enhancement in the ZPL emission peak with increasing p. KNaSiF$_6$:Mn^{4+} is of type F2 and thus still showed relatively strong ZPL emission even at room ambient.[61] The blue shifts in the PLE energies in Fig. 29a could be explained by an increase of the crystal field strength.[25] The red shifts in the PL energies could also be ascribed to hybridization of the orbital or an energy level split due to the decrease in the lattice parameters and resultant cell volume reduction with increasing p.

Because of its highly symmetric nature, no strong ZPL emission peak was observed in K$_2$SiF$_6$:Mn^{4+} at room ambient.[8] However, an application of the hydrostatic pressures can modify its crystal structure to a deformed one, resulting in a clear appearance of the ZPL emission peak in accord with increasing p. Lazarowska et al.[133] observed an intense ZPL emission peak even after decompressing the examined phosphor to ambient pressure. They attributed this phenomenon to pressure-induced change in the local structure of the MnF$_6^{2-}$ octahedron. In the case of BaTiF$_6$:Mn^{4+},[134] any enhancement in the pressure-induced ZPL emission intensity has not been observed for pressures up to $p \sim 21$ GPa. BaTiF$_6$:Mn^{4+} is of type F1 and thus did not show any strong ZPL emission peak at room ambient.[52]

Table VI. Pressure coefficients of the intra-*d*-shell Mn^{4+} transition energies in fluoride and oxide phosphors at 300 K.

Material	Host material	Transition	Mode	B_u (GPa)	dE_R/dp (meV/GPa)	a_R^0 (eV)	Ref.
Fluoride	BaTiF$_6$	$^2E_g \rightarrow {}^4A_{2g}$	ν_6		-1.96		134
			ν_4		-2.02		
	KNaSiF$_6$	$^4A_{2g} \rightarrow {}^4T_{2g}$	PLE		11.2		25
		$^4A_{2g} \rightarrow {}^4T_{1g}$	PLE		12.1		
		$^2E_g \rightarrow {}^4A_{2g}$	ZPL		-1.99		
	K$_2$SiF$_6$	$^2E_g \rightarrow {}^4A_{2g}$	ZPL	16.82[*1]	-2.47	0.042	133
			ν_6		-3.07	0.052	
			ν_4		-3.02	0.051	
Oxide	α-Al$_2$O$_3$	$^2E_g \rightarrow {}^4A_{2g}$	ZPL (R$_1$)	254[*2]	-1.05	0.27	142
			ZPL (R$_2$)		-1.06	0.27	
	Gd$_3$Ga$_5$O$_{12}$	$^2E_g \rightarrow {}^4A_{2g}$	ZPL (1)[*3]	270[*4]	-2.33	0.63	135
			ZPL (2)[*3]		-1.85	0.50	
	Sr$_4$Al$_{14}$O$_{25}$	$^2E_g \rightarrow {}^4A_{2g}$	ZPL		-2.65		143
	YAlO$_3$	$^2E_g \rightarrow {}^4A_{2g}$	ZPL	192[*5]	-1.49	0.29	127

[*1]Theoretical value (see Ref. 136).
[*2]See Ref. 150.
[*3]Emission lines from different Mn^{4+} sites in Gd$_3$Ga$_5$O$_{12}$.
[*4]See text.
[*5]See Ref. 157.

In Fig. 29b, the pressure derivatives of the vibronic sideband peaks are slightly larger than that of the ZPL emission peak. The tendency of increasing vibration frequencies with increasing *p* is in qualitative agreement with phonons in various semiconductors (see, e.g., Ref. 78). The pressure coefficients dE_R/dp listed in Table VI are of the order of 2 meV/GPa that are roughly about three times larger than that for Cr^{3+} ions,[135] where the electronic configuration of Cr^{3+} is the same as that of Mn^{4+} ($3d^3$).

The hydrostatic pressure dependence of the integrated PL intensity (I_{PL}) for BaTiF$_6$:Mn^{4+} has been measured by Wang et al.[134] We reproduce in Fig. 30 their measured I_{PL} vs *p* data with modifying an original graph from linear to semi-log plot. The inset shows a schematic illustration of the CC model used to explain the peculiar I_{PL} vs *p* data. This illustration can also be used to explain the thermal quenching phenomena of $I_{PL}(T)$ in Eq. 35 and decay lifetime phenomena of $\tau(T)$ in Eq. 36 by replacing E_p in Fig. 30 with E_q.

When the ground- and excited-state CC curves in the inset of Fig. 30 intersect at an arbitrary configurational coordinate, an electron in the excited state can reach the crossing point in the CC curve with assistance by thermal energy of k_BT and can then reach or return to the ground state nonradiatively. Therefore, the nonradiative transition probability N can be written using E_q as

$$N = N_0 \exp\left(-E_q/k_BT\right) \quad [39]$$

where N_0 is a product of the transition probability between the ground and excited states and frequency with which the excited state reached the crossing point (Fig. 30). N_0 can be regarded as a constant, since it is only weakly dependent on temperature T and may also only weakly
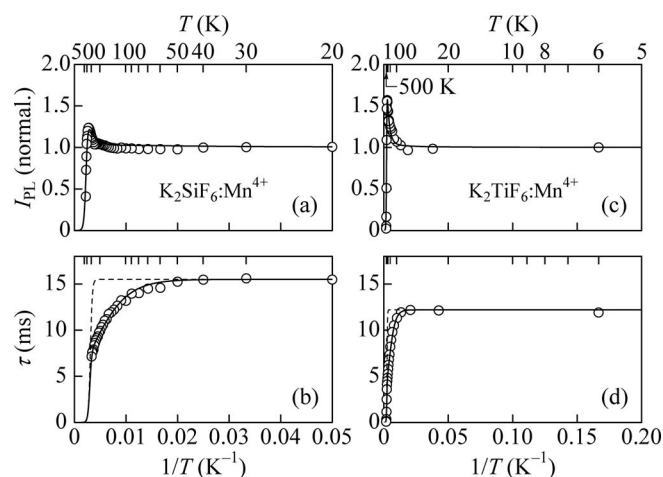
Figure 26. (a) Integrated PL intensity I_{PL} and (b) PL decay time τ vs reciprocal temperature $1/T$ for the K$_2$SiF$_6$:Mn^{4+} fluoride phosphor (type F1). The experimental data are taken from Ref. 20. The solid line in (a) shows the result calculated using Eq. 35, whereas the solid and dashed lines in (b) represent the results calculated using Eq. 36 with and without considering the $i = 1$ decay process term (i.e., a small activation-energy process term), respectively. The same plots as in (a) and (b), but those for the K$_2$TiF$_6$:Mn^{4+} fluoride phosphor (type F1) are shown in (c) and (d) with the experimental data taken from Ref. 131.
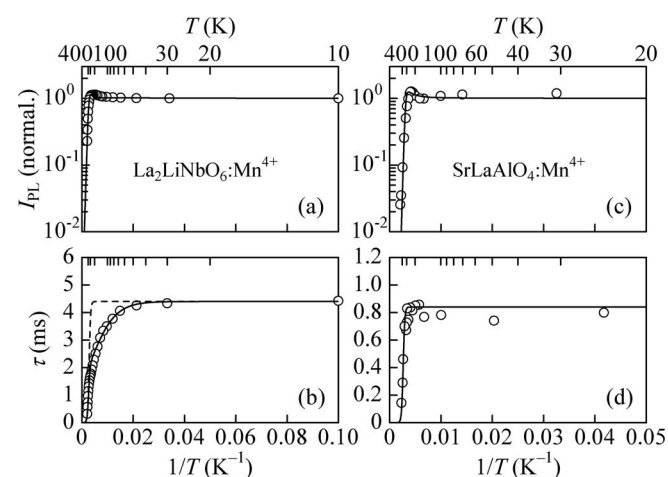
Figure 27. (a) Integrated PL intensity I_{PL} and (b) PL decay time τ vs reciprocal temperature $1/T$ for the La$_2$LiNbO$_6$:Mn^{4+} oxide phosphor (type O-C). The experimental data are taken from Ref. 38. The solid line in (a) shows the result calculated using Eq. 35, whereas the solid and dashed lines in (b) represent the results calculated using Eq. 36 with and without considering the $i = 1$ decay process term (i.e., a small activation-energy process term), respectively. The same plots as in (a) and (b), but those for the SrLaAlO$_4$:Mn^{4+} oxide phosphor (type O-A) are shown in (c) and (d) with the experimental data taken from Ref. 126 [no dashed line in (d)].
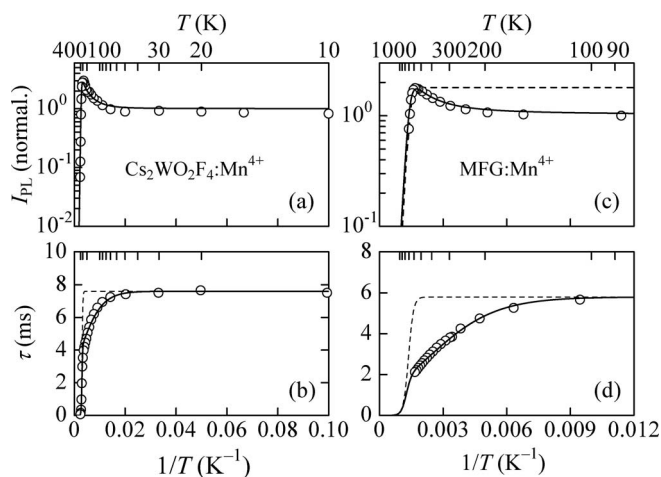
Figure 28. (a) Integrated PL intensity I_{PL} and (b) PL decay time τ vs reciprocal temperature $1/T$ for the $Cs_2WO_2F_4$:Mn^{4+} oxyfluoride phosphor (type OF-A). The experimental data are taken from Ref. 33. The solid line in (a) shows the result calculated using Eq. 35, whereas the solid and dashed lines in (b) represent the results calculated using Eq. 36 with and without considering the $i = 1$ decay process term (i.e., a small activation-energy process term), respectively. The same plots as in (a) and (b), but those for the MFG:Mn^{4+} oxyfluoride phosphor (type OF-B) are shown in (c) and (d) with the experimental data taken from Refs. 35 and 132. The dashed line in (c) also shows the result calculated using Eq. 35 without considering the $i = 1$ quenching process term (i.e., a small activation-energy process term).
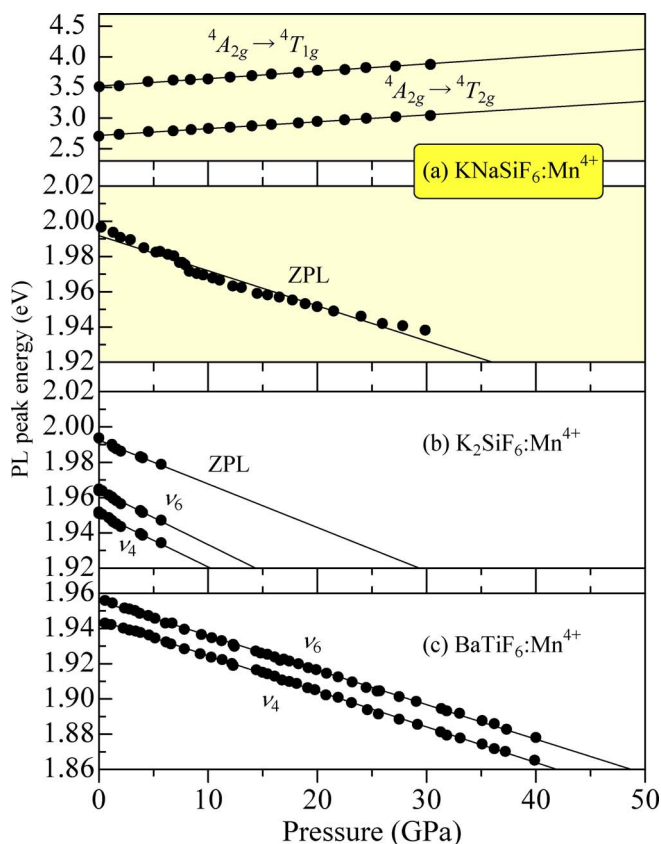
Figure 29. Hydrostatic pressure dependence of the Mn^{4+} emission energy for (a) the KNaSiF$_6$:Mn^{4+} (type F2),[25] (b) K$_2$SiF$_6$:Mn^{4+} (type F1),[133] and (c) BaTiF$_6$:Mn^{4+} (type F1) fluoride phosphors[134] measured at 300 K. Hydrostatic pressure dependence of the PLE transition energies in the KNaSiF$_6$:Mn^{4+} phosphor[25] is also shown in the upper part of (a). The pressure derivatives of these transition energies are listed in Table VI.
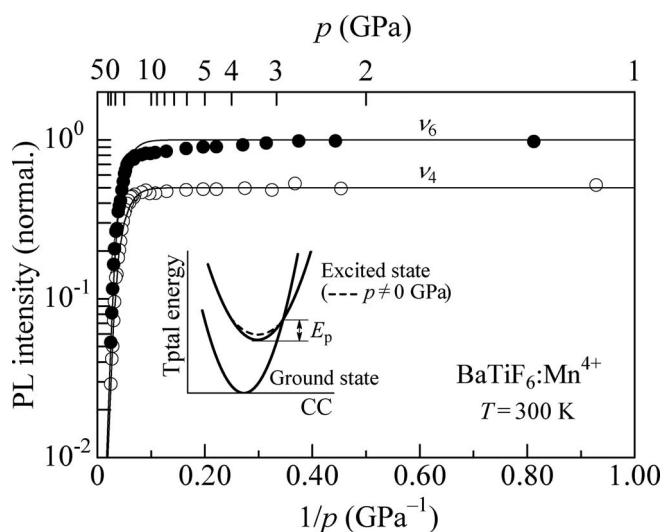

Figure 30. Hydrostatic pressure dependence of the integrated PL intensity (I_{PL}) for the BaTiF$_6$:Mn^{4+} (type F1) fluoride phosphor at 300 K.[134] The solid lines show the results calculated using Eq. 41. The inset also shows a schematic illustration of the CC model used to explain the I_{PL} vs pressure (p) data.

dependent on pressure p of particular interest here. This quantity is called the frequency factor and is typically of the order of 10^{13} s^{-1}.

Let R being the radiative or luminescence probability, the luminescence efficiency η can be written as

$$\eta = \frac{R}{R + N} = \frac{1}{1 + \frac{N_0}{R} \exp\left(-E_q/k_B T\right)} \quad [40]$$

This expression is essentially the same as the first term on the right-hand side of Eq. 35 and also that of Eq. 36.

An application of p will lead to lowering or widening of the gap energy between the ground and excited states E_p in Fig. 30. Assuming lowering of the gap energy by applying p, an electron in the excited state feels a decrease in the barrier height in reaching the crossing point in the CC curve and subsequently in returning more easily to the ground state nonradiatively. As a result, luminescence recombination probability will decrease with increasing p that is essentially the same as the case of thermal quenching, where an electron overcomes the crossing point and then returns to the ground state nonradiatively with an assist of the thermal energy of $k_B T$. Thus, we can write the pressure dependence of PL intensity $I_{PL}(p)$ as

$$I_{PL}(p) = \frac{I_0}{\sum_i c_i \exp\left(-E_{pi}/k_p p\right)} \quad [41]$$

where k_p is in units of eV/Pa. Like in the thermal quenching with an increase of $k_B T$, an increase of $k_p p$ reduces E_{pi} and makes easy to return the electrons to the ground state nonradiatively, resulting in a degreased I_{PL} at high p.

The solid lines in Fig. 30 show the results calculated using Eq. 41. The best-fit parameters are $I_0 = 1.0$, $c_1 = 20$, $E_{p1}/k_p = 70$ GPa, $c_2 = 5.0 \times 10^3$, and $E_{p2}/k_p = 2.3 \times 10^2$ GPa (ν_6); $I_0 = 0.5$, $c_1 = 20$, $E_{p1}/k_p = 70$ GPa, $c_2 = 4.0 \times 10^3$, and $E_{p2}/k_p = 2.3 \times 10^2$ GPa (ν_4). An excellent agreement between the theory and experiment can be found in Fig. 30.

Pressure-induced structural phase transition.—Some crystalline substances exhibit a change in the crystal structure at high pressures, known as the pressure-induced structural phase transition.[78] Jin et al.[25] observed on KNaTiF$_6$:Mn^{4+} no sign of the structural phase transition up to $p \sim 31$ GPa. For K$_2$SiF$_6$, ab initio calculations on the pressure dependence of structural properties have been performed by Brik and Srivastava.[136] They predicted no occurrence of the phase transition up to $p = 20$ GPa. Experimentally, Prinsloo et al.[137] reported the vibrational spectra of "hexagonal" K$_2$SiF$_6$ in this "cubic" stable material at

room ambient, but details were not reported in it. More recently, Gramaccioli and Campostrini[138] reported a new hexagonal polymorph of K_2SiF_6 in a colorless pyramidal form as the mineral, Demartinite. Lv et al.[139] also synthesized hexagonal K_2SiF_6 in the laboratory. However, no detailed study on the structural phase transition has been performed on K_2SiF_6 or K_2SiF_6:Mn^{4+} until now. No any theoretical or experimental study on the structural phase transition has also been reported on $KNaSiF_6$ or $KNaSiF_6$:Mn^{4+} until now.

Wang et al.[134] observed on $BaTiF_6$:Mn^{4+} the structural phase transition by means of XRD, PL, and Raman scattering measurements. The phase transition sequence was: trigonal at ambient pressure → monoclinic at $0.5 - 4.0$ GPa → triclinic above 14 GPa. However, no clear change in the PL spectral feature reflecting such pressure-induced phase transition has been observed before and after transition. Discussion in the early Section promises an observation of the intense ZPL emission peak from such highly anisotropic crystals of "monoclinic" and "triclinic" (Tables II and III); however, no strong ZPL emission peak was observed even at high pressures $p = 10.1$ and 20.7 GPa.[134]

Deformation potential for Mn^{4+} ion states.—A deformation potential (DP) is a quantity proportional to a matrix element of an operator belonging to a crystal deformation between a final and an initial electronic state.[78] It has the units of eV or eV/Å. Studies on the pressure effects of the Mn^{4+}-activated fluoride phosphors in Fig. 29 showed that the red emission energy E_R ($^2E_g \rightarrow {}^4A_{2g}$) changes in an isotropic manner with respect to hydrostatic pressure p, i.e., it shows a redshift with increasing p without introducing any splitting of the red emission peaks. Therefore, we simply define DP

$$H_R = \frac{\hbar^2 k^2}{2m} + a_R^0 \left(e_{xx} + e_{yy} + e_{zz} \right) \qquad [42]$$

where m is the intra-d-shell electron mass giving the dispersion relation between E and k, a_R^0 is the DP for the Mn^{4+} red emission, and e_{ij} is the strain tensor component ($i, j = x, y,$ or z).

The deformation potential a_R^0 can now be written, in a phenomenological form, as

$$a_R^0 = -B_u \frac{dE_R}{dp} = -\frac{1}{\kappa} \frac{dE_R}{dp} \qquad [43]$$

B_u and κ are the bulk modulus and compressibility, respectively, where the inverse of B_u gives a substance's compressibility κ, which can be defined by

$$\kappa = \frac{1}{B_u} \equiv -\frac{1}{V} \frac{dV}{dp} \qquad [44]$$

The pressure derivative in Eq. 43 represents the pressure-induced change in E_R. Equation 43 is written in a modified form as

$$a_R^0 = \frac{dE_R}{d \ln V} \qquad [45]$$

where $d\ln V = dV/V$ is the fractional volume change of the substance. Note that the Mn^{4+} red emission under an application of hydrostatic pressure comes from the locally deformed MnF_6^{2-} or MnO_6^{8-} octahedron. Therefore, it is possible to regard κ as a "local" compressibility of the Mn−ligand bond instead of the "bulk" compressibility.

Unfortunately, the compressibility of $KNaSiF_6$, K_2SiF_6, or $BaTiF_6$ host has not been experimentally determined until now. Therefore, we cannot determine the DPs for the Mn^{4+} red emission in such fluoride phosphors using Eq. 43. Theoretically, Brik and Srivastava[136] calculated bulk modulus of K_2SiF_6 to be $B_u = 16.82$ GPa [generalized gradient approximation (GGA)] and 42.28 GPa [local density approximation (LDA)]. Since the LDA value is very large, comparable to that of diamond (~ 44 GPa),[78] let us consider the GGA value of 16.82 GPa in our DP calculation for K_2SiF_6 using Eq. 43. The calculated DP values are 0.042 eV (ZPL), 0.052 eV (ν_6), and 0.051 eV (ν_4), which are one or two orders smaller than the hydrostatic Γ-valence-band DPs in various semiconductors.[78] Such smaller DPs of the Mn^{4+} red emission energies may come from the intra-d-shell transition nature, i.e., smaller dE_R/dp values, together with smaller B_u value of the fluoride host material.
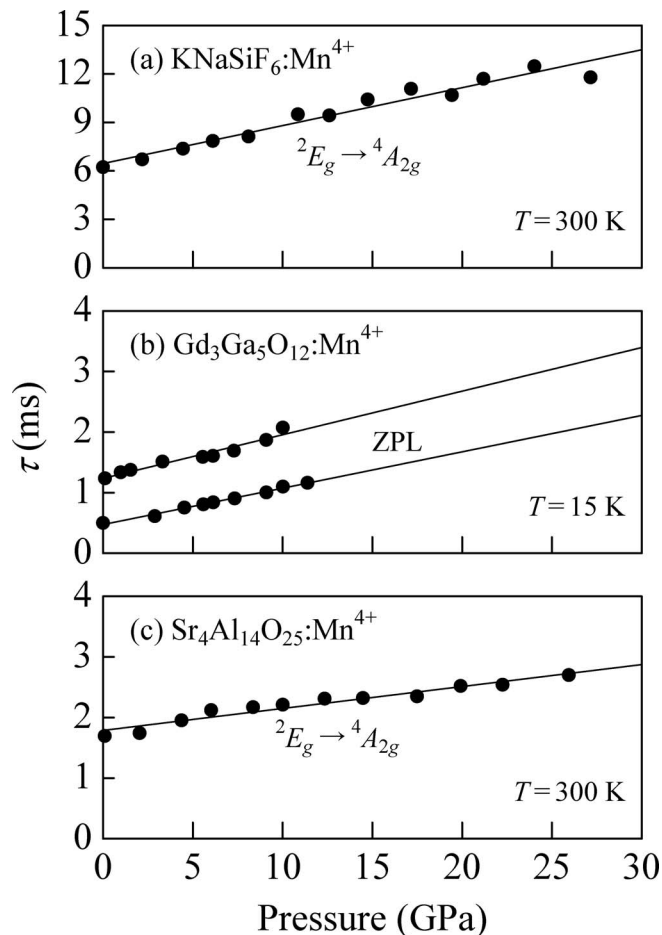

Figure 31. Hydrostatic pressure dependence of the PL decay lifetime for (a) the $KNaSiF_6$:Mn^{4+} (type F2),[25] (b) $Gd_3Ga_5O_{12}$:Mn^{4+} (type O-A),[135] and (c) $Sr_4Al_{14}O_{25}$:Mn^{4+} (type O-A) phosphors[143] measured at 300 or 15 K.

Effects of pressure on PL decay characteristics.—The PL decay characteristics of $KNaSiF_6$:Mn^{4+} have been studied by Jin et al.[25] up to $p \sim 31$ GPa. The observed decay curves were examined by a single-exponential function. The results of this study are shown in Fig. 31a. The decay lifetime increases almost linearly at a rate of $d\tau/dp \sim 2.3 \times 10^{-1}$ ms/GPa. No clear difference in τ has also been observed between the ZPL emission peak and its vibronic sideband peaks.

The effects of pressure on the energetic structure and related luminescence properties of some ions in the $3d^3$ configuration, like Cr^{3+} and Mn^{4+}, have been theoretically studied by some authors (see, e.g., Grinberg and Suchocki[17] and Eggert et al.).[140,141] The dominant pressure dependence of the $3d^3$ luminescence lifetime can then be formulated by

$$\tau = A \frac{(\Delta_{E-T})^2}{|< V_{ET} >|^2} \qquad [46]$$

where Δ_{E-T} is the energy difference between the ^4E_g ($^2T_{1g}$) and $^4T_{2g}$ states (Fig. 1b), $< V_{ET} >$ is the spin−orbit coupling constant that mixes the ^4E_g ($^2T_{1g}$) and $^4T_{2g}$ states, and A is a constant scaling factor.

Increased τ with increasing p for $KNaSiF_6$:Mn^{4+} observed in Fig. 31a can be well explained by Eq. 46.[25] An increasing rate for $KNaSiF_6$:Mn^{4+} is given by $d\tau/dp \sim 0.23$ ms/GPa. Decreased admixture of the $^4T_{2g}$ wave function to the ^2E_g wave function with the increase of p is the reason for an increase in τ of the $^2E_g \rightarrow {}^4A_{2g}$ transitions. However, a decrease in τ with application of compressive stress p and further with decompression has also been observed in K_2SiF_6:Mn^{4+} from $\tau \sim 9$ ms at room pressure to 6 ms after compression at $p \sim 6$ GPa and also decompression to room ambient, in
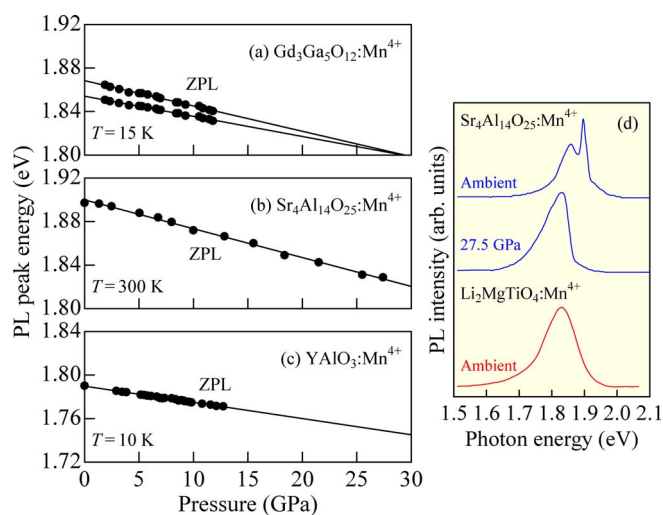
Figure 32. Hydrostatic pressure dependence of the Mn^{4+} emission energy for (a) the Gd$_3$Ga$_5$O$_{12}$:Mn^{4+} (type O-A),[135] (b) Sr$_4$Al$_{14}$O$_{25}$:Mn^{4+} (type O-A),[143] and (c) YAlO$_3$:Mn^{4+} (type O-A) oxide phosphors[127] measured at 15, 300, and 10 K, respectively. The pressure derivatives of these transition energies are listed in Table VI. (d) Room-temperature PL spectra for the Sr$_4$Al$_{14}$O$_{25}$:Mn^{4+} oxide phosphor[143] measured at ambient pressure and $p = 27.5$ GPa, together with that for the Li$_2$MgTiO$_4$:Mn^{4+} oxide phosphor at ambient pressure (Ref. 108). Similarity in the PL spectral shape for the Sr$_4$Al$_{14}$O$_{25}$:Mn^{4+} oxide phosphor (type O-A) measured at $p = 27.5$ GPa with that for the Li$_2$MgTiO$_4$:Mn^{4+} oxide phosphor (type O-B) at ambient pressure can be recognized in (d).

accord with an observation of the strong ZPL emission peak even after decompression to room ambient.[133] Therefore, it is evident that in the case of K$_2$SiF$_6$:Mn^{4+} an appearance of the strong ZPL emission peak due to the $^2E_g \rightarrow \, ^4A_{2g}$ transitions can simultaneously cause the shortening of luminescence decay lifetime.

*Oxide phosphors.—Pressure-induced PL spectral change.—*The hydrostatic pressure effects of the red emission from Mn^{4+}-activated oxide phosphors have been reported by several authors.[127,135,142,143] Figure 32 shows the pressure dependence of the Mn^{4+} emission energy for some oxide phosphors: (a) Gd$_3$Ga$_5$O$_{12}$:Mn^{4+},[135] (b) Sr$_4$Al$_{14}$O$_{25}$:Mn^{4+},[143] and (c) YAlO$_3$:Mn^{4+}.[127] The pressure derivatives of these emission energies are listed in Table VI. As in Fig. 29, the PL peak energies decreased almost linearly with increasing p. No large difference in the pressure derivatives can be found for phosphors of the fluoride and oxide hosts (Table VI). No drastic change in the PL spectral feature can also be found for Gd$_3$Ga$_5$O$_{12}$:Mn^{4+} and YAlO$_3$:Mn^{4+}. Note, however, that the PL spectra of Sr$_4$Al$_{14}$O$_{25}$:Mn^{4+} at high pressures become structureless, resulting in a striking similarity to those for type O-B oxide phosphors. Let us compare in Fig. 32d the PL spectra for Sr$_4$Al$_{14}$O$_{25}$:Mn^{4+} (type O-A2) measured at $p = 1$ atm and 27.5 GPa to that for Li$_2$MgTiO$_4$:Mn^{4+} (type O-B) at room pressure.[108] The results in Fig. 32d suggest that the unique PL features found in type O-B phosphors (Fig. 17) may come from a local microscopic distortion of the MnF$_6^{2-}$ octahedron induced during synthetic processes (or, in other words, the host crystals of type O-B phosphors may be easy to contain a local microscopic distortion in their lattices during synthetic processes).

Ruby crystal (α-Al$_2$O$_3$:Cr^{3+}) is popularly used as an element of pressure sensor. It is interesting to note that the red emission in the Mn^{4+}-activated fluoride and oxide phosphors is more sensitive to pressure than those of Cr^{3+} R$_1$ [$^2E_g \, (\overline{E}) \rightarrow \, ^4A_{2g}$] and R$_2$ [$^2E_g \, (2\overline{A}) \rightarrow \, ^4A_{2g}$] emissions in ruby,[142] suggesting superiority of the Mn^{4+}-activated phosphors for use in pressure sensor applications. Details of the Cr^{3+} R$_1$ and R$_2$ emission properties in an oxide crystal can be found in Ref. 144.

*Pressure-induced structural phase transition.—*The pressure-induced structural phase transition on α-Al$_2$O$_3$ has been studied theoretically by several authors. The results show that Al$_2$O$_3$ can transform from the corundum (α) to the as-yet unobserved Rh$_2$O$_3$ (II) structure at ~ 78 GPa, and can further transform to *Pbnm* perovskite structure at 223 GPa.[145] Relative stability of six alumina polymorphs, namely, corundum, Rh$_2$O$_3$ (II), *Pbnm* perovskite, $R\overline{3}c$ perovskite, *A*-type rare-earth sesquioxide, and *B*-type rare-earth sesquioxide has also been discussed by first-principles study.[146] Experimentally, the XRD measurements indicate that ruby crystal of α-Al$_2$O$_3$:Cr^{3+} transforms to the Rh$_2$O$_3$ (II) structure when heated to temperatures exceeding ~ 1000 K at pressures above ~ 100 GPa,[147] in agreement with some previous theoretical predictions.

To the best of our knowledge, no detailed pressure-induced structural phase transition has been reported theoretically or experimentally on Gd$_3$Ga$_5$O$_{12}$ and Sr$_4$Al$_{14}$O$_{25}$ of interest in the present study (Table VI). A phase transition in YAlO$_3$ from orthorhombic *Pbnm* (or *Pnma*) to tetragonal *I4/mcm* phase has been theoretically predicted to occur at 80 GPa.[148] The pressure dependence of the elastic constants and mechanical stability of the perovskite-type crystal YAlO$_3$ has also been examined by Hernańdez-Rodŕıguez et al.,[149] showing that its phase is mechanically stable until 92 GPa. In fact, the XRD and Raman scattering results together with theoretical calculation up to 30 GPa showed no evidence of any phase transition. Calculation by the same authors further supported possible phase transition from *Pnma* to tetragonal *I4/mcm* phase in YAlO$_3$ above 92 GPa.[149] However, no detailed theoretical or experimental study on the effects of hydrostatic pressure for any Mn^{4+}-activated oxide phosphors focused on the phase transition has been carried out until now.

*Deformation potential for Mn^{4+} ion states.—*The experimental bulk modulus of α-Al$_2$O$_3$ reported by Goto et al.[150] is 254 GPa at 300 K. The calculated DPs using Eq. 43 and bulk modulus of 254 GPa are 0.27 eV for the R$_1$ and R$_2$ red emissions. The experimental bulk modulus of Gd$_3$Ga$_5$O$_{12}$ garnet has also been reported to be 169 ± 15 GPa (Ref. 151) and 373 ± 5 GPa, (Ref. 152), giving an average value of $B_u \sim 270$ GPa. Using this average value, we obtain the DPs for Gd$_3$Ga$_5$O$_{12}$ (Table VI).

Bulk modulus has not been reported on Sr$_4$Al$_{14}$O$_{25}$. On the other hand, there have been reported bulk modulus values of YAlO$_3$ perovskite by a number of authors. Earlier experimental studies report $B_u \sim 185$–220 GPa.[153–156] More recently, Ross et al.[157] reported 192±2 GPa. Therefore, no large difference in these B_u values can be found for YAlO$_3$ perovskite. A value of $B_u \sim 192$ GPa was used in our calculation of the DPs for YAlO$_3$ in Table VI.

*Effects of pressure on PL decay characteristics.—*As in the case of KNaSiF$_6$:Mn^{4+} (Fig. 31a), we can see an increase in the decay lifetime with increasing p for some oxide phosphors, Gd$_3$Ga$_5$O$_{12}$:Mn^{4+} (Ref. 135) and Sr$_4$Al$_{14}$O$_{25}$:Mn^{4+} (Ref. 143) (Figs. 31b and 31c). Rate of the decay lifetime increase for Gd$_3$Ga$_5$O$_{12}$:Mn^{4+} with Mn^{4+} ions occupied in the two different octahedral sites can be given by $d\tau/dp \sim 0.072$ and ~ 0.060 ms/GPa and that for Sr$_4$Al$_{14}$O$_{25}$:Mn^{4+} by ~ 0.036 ms/GPa. The increased τ with increasing p can be explained by Eq. 46. No any data on the pressure effects of the Mn^{4+}-activated "oxyfluoride" phosphors has been reported until now.

Mn^{4+} Concentration Dependence of PL Spectral Feature

*Fluoride phosphors.—*Luminescence intensity usually increases almost linearly with the increase of activator dopant concentration n. To enhance the PL intensity from a phosphor, therefore, the activator concentration in the host should be as high as possible. However, the electrons excited in the high energy states will meet various nonradiative relaxation processes. Such processes should occur more drastically if phosphors were more highly doped with the activator ions, known as the concentration quenching. As a result, the PL intensity tends to saturate and shows a decrease with the further increase of n.

The concentration quenching might be caused by an energy transfer among the activator ions with eventually transferring to quenching sites or traps. The energy transfer among the Mn^{4+} ions occurs via
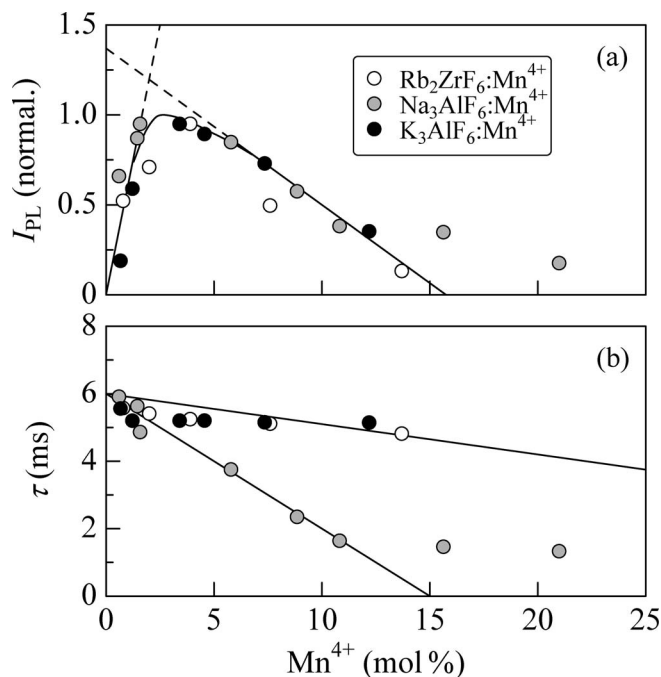
Figure 33. (a) Integrated PL intensity I_{PL} and (b) PL decay time τ vs Mn^{4+} concentration n for the Rb_2ZrF_6:Mn^{4+} (type F1),[159] Na_3AlF_6:Mn^{4+} (type F2),[57] and K_3AlF_6:Mn^{4+} (type F2) fluoride phosphors at 300 K.[56] The solid line in (a) represents a tendency of the I_{PL} vs n variation. The solid lines in (b) also show a linearly degreasing tendency of τ with increasing n.

Figure 34. (a) Integrated PL intensity I_{PL} and (b) PL decay time τ vs Mn^{4+} concentration n for (a) the $Ca_3La_2W_2O_{12}$:Mn^{4+} (type O-A),[166] (b) $CaAl_2O_4$:Mn^{4+} (type O-A),[167] (c) $SrAl_4O_7$:Mn^{4+} (type O-A),[168] and (d) Gd_2ZnTiO_6:Mn^{4+} (type O-A) oxide phosphors at 300 K.[103] The solid lines on the left-hand side of (a)–(d) represent a tendency of the I_{PL} vs n variation. The solid lines on the right-hand side of (a)–(d) also show a linearly degreasing tendency of τ with increasing n.

some different mechanisms, such as the exchange interaction, multipolar interaction, and radiation reabsorption. Based on the Dexter's energy transfer formula,[158] the nature of energy transfer can be understood from

$$\frac{I}{n} = K\big[1 + \beta(n)^{s/3}\big]^{-1} \qquad [47]$$

with $s = 3$, 6, 8, and 10 correspond to the exchange, dipole−dipole, dipole−quadrupole, and quadrupole−quadrupole interactions, respectively. In Eq. 47, I and n represent the integrated PL intensity and Mn^{4+} dopant concentration, respectively.

Figure 33 shows (a) the integrated PL intensity I_{PL} and (b) PL decay time τ vs Mn^{4+} concentration n for Rb_2ZrF_6:Mn^{4+},[159] Na_3AlF_6:Mn^{4+},[57] and K_3AlF_6:Mn^{4+}.[56] The solid line in Fig. 33a represents a tendency of the I_{PL} vs n variation. The I_{PL} vs n data for these fluoride phosphors exhibit a maximum at $n \sim 3$ mol %. The various fluoride phosphors also showed a maximum in I_{PL} at $n \sim 1 - 5$ mol %. This range of n for the fluoride phosphors is considerably larger than that of the oxide phosphors, $n \sim 0.5 - 1$ mol % (see "*Oxide phosphors*" below). The τ vs n plots in Fig. 33b show a linearly decreasing nature of τ with increasing n (solid line), which has been observed in many phosphors.

The concentration quenching of Mn^{4+} in the fluoride phosphors has been determined to be of the dipole−dipole interaction.[60,160−164] However, Liu et al.[165] has recently observed the quadrupole−quadrupole quenching interaction in Na_2TiF_6:Mn^{4+} phosphor. An energy transfer directly from Mn^{4+} ions to luminescence quenchers like crystal defects has also been reported to occur as the main concentration quenching mechanism in some fluoride phosphors like K_2TiF_6:Mn^{4+} (Ref. 131) and $CsNaGeF_6$:Mn^{4+} (Ref. 66). The nonradiative recombination probability in this case increases almost linearly with increasing n, i.e., occurring among the nearest-neighbor Mn^{4+} ions via the exchange interaction with $s = 3$ in Eq. 47.

Oxide phosphors.—The same as in Fig. 33, but those for the oxide phosphors are shown in Fig. 34. The phosphors presented here are (a) $Ca_3La_2W_2O_{12}$:Mn^{4+},[166] (b) $CaAl_2O_4$:Mn^{4+},[167] (c) $SrAl_4O_7$:Mn^{4+},[168]
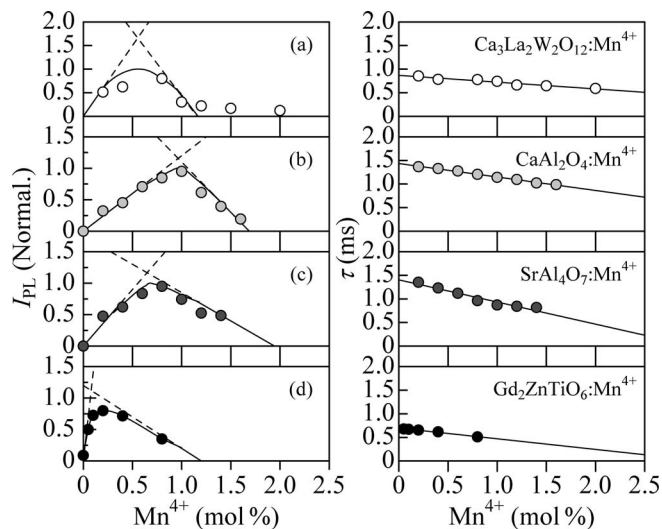
and (d) Gd_2ZnTiO_6:Mn^{4+}.[103] As in Fig. 33, the I_{PL} vs n plots for the oxide phosphors in Fig. 34 exhibit a maximum at $n \sim 0.1 - 1$ mol %. The various experimental data also suggested that the I_{PL} peaks in the oxide phosphors occur at $n \sim 0.1 - 2$ mol % and mostly fall in the range of $n \sim 0.5 - 1$ mol %. These optimum n values are considerably smaller than those for the fluoride oxides, $n \sim 1 - 5$ mol %, discussed in "*Fluoride phosphors*." As in the fluoride phosphors (Fig. 33), all the τ plots in Fig. 34 show a linearly decreasing tendency with increasing n.

Although the dipole−quadrupole and exchange interactions have been reported to occur (see, e.g., Refs. 169−172), the concentration quenching mechanism in many oxide phosphors is of the dipole−dipole interaction (see, e,g., Refs. 83, 99, 103, 119, 166, 173−189).

Oxyfluoride phosphors.—The effects of Mn^{4+} concentration n on the luminesce intensity and decay lifetime have been studied on $LiAl_4O_6F$:Mn^{4+} oxyfluoride phosphor.[190] The results of this study are shown in Fig. 35. The I_{PL} vs n plots in Fig. 35a show a maximum at $n \sim 0.2\%$. This optimum n value is close to the range of $n \sim 0.5 - 1$ mol % for the oxide phos012phors mentioned in "*Oxide phosphors*" rather than that of type OF-A (fluoride-like phosphor). The I_{PL} vs n data have also been measured for $Cs_2WO_2F_4$:Mn^{4+} (type OF-A1).[33] An optimum n giving a maximum in I_{PL} is ~ 15 mol %, which is much larger than those typically observed in the Mn^{4+}-activated fluoride phosphors, $n \sim 1 - 5$ mol %.

As in Figs. 33 and 34, the luminescence lifetime plots for $LiAl_4O_6F$:Mn^{4+} obtained in Fig. 35b show that τ gradually decreases with increasing n, typically observed in many phosphors. However, the same data but for $Cs_2WO_2F_4$:Mn^{4+} showed a small, but clear peak at $n \sim 10$ mol %.[33] The dependence of τ on n was also examined for $Na_2WO_2F_4$:Mn^{4+} (type OF-A2) at wavelength of self-luminescence from WO_2 group.[191] The result showed a gradual decrease of τ with increasing n. This result was used to proof an energy transfer from WO_2 group to Mn^{4+} ion in the $Na_2WO_2F_4$:Mn^{4+} phosphor.

The concentration quenching of Mn^{4+} in the oxyfluoride phosphors and also in a fluorine compound phosphor has been studied
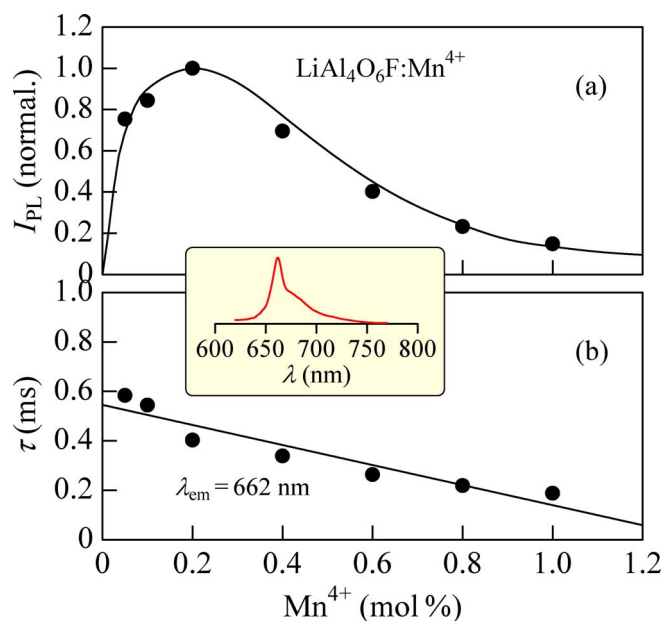
Figure 35. (a) Integrated PL intensity I_{PL} and (b) PL decay time τ vs Mn^{4+} concentration n for the $LiAl_4O_6F:Mn^{4+}$ (type OF-B) oxyfluoride phosphor at 300 K.[190] The solid line in (a) represents a tendency of the I_{PL} vs n variation. The solid line in (b) also shows a linearly degreasing tendency of τ with increasing n. The inset shows the PL spectrum measured at 300 K.

Figure 36. Room-temperature PL spectra for (a) some Mn^{4+}-activated fluoride, (b) oxide, and (c) oxyfluoride phosphors. Note that the phosphors selected here have the lowest and highest ZPL emission energies in each group of Tables II (fluoride),[71,125] IV (oxide),[83,193,194] and V (oxyfluoride).[34,195] The vertical arrows in each figure show the positions of the $E(^2E_g)_{ZPL}$ emission energy (ZPL). The dashed line in (c) indicates the sensitivity of the human eye, i.e., the photopic spectral luminous efficiency (PSLE).

and obtained to be of the dipole−dipole interaction [$Cs_2NbOF_6:Mn^{4+}$ (Ref. 192), $LiAl_4O_6F:Mn^{4+}$ (Ref. 190), and $NaHF_2:Mn^{4+}$ (Ref. 37)]. Therefore, almost all the Mn^{4+}-activated phosphors considered in this review article exhibit the dipole−dipole interaction as the main concentration quenching mechanism. $Na_2TiF_6:Mn^{4+}$ is an exception that exhibits the quadrupole−quadrupole interaction.[165] A resonant energy transfer from $[WO_2F_4]^{2−}$ to Mn^{4+} ion has also been observed in $Cs_2WO_2F_4:Mn^{4+}$.[33] The decay lifetime measurements of this phosphor showed that the resonant energy transfer is caused by the exchange interaction rather than any multipolar interaction like dipole−dipole or dipole−quadrupole interaction.

Displaying Device and Indoor Plant Cultivation Applications

Displaying device application.—We show in Fig. 36 the room-temperature PL spectra observed from (a) some Mn^{4+}-activated fluoride, (b) oxide, and (c) oxyfluoride phosphors. These phosphors were selected to have the lowest and highest ZPL emission energies in each group of Tables II (fluoride), IV (oxide), and V (oxyfluoride). As understood from Fig. 36a, the ZPL wavelength range for the "fluoride" phosphors is very narrow, from ∼ 615 nm ($Na_5Zr_2F_{13}:Mn^{4+}$)[71] to ∼ 625 nm ($BaTiF_6:Mn^{4+}$).[125] On the other hand, the range for the "oxide" phosphors in Fig. 36b is very wide, from ∼ 640 nm ($Mg_4GeO_6:Mn^{4+}$),[193] via ∼ 675 nm ($Ba_2YNbO_6:Mn^{4+}$),[83] to ∼ 715 nm ($LaAlO_3:Mn^{4+}$).[194] As expected, the range for the "oxyfluoride" phosphors falls between those for the fluoride and oxide phosphors, i.e., from ∼ 620 nm ($Na_2WO_2F_4:Mn^{4+}$)[34] to ∼ 685 nm ($Sr_2ScO_3F:Mn^{4+}$).[195] [Very recent study on $K_3HF_2WO_2F_4:Mn^{4+}$ (Ref. 196) observed the ZPL emission wavelength of ∼ 618 nm, which is slightly shorter than that of $Na_2WO_2F_4:Mn^{4+}$ (see Table V).]

The Mn^{4+}-activated phosphors exhibit efficient red emission under blue or UV excitation. Efficient sharp red emission with internal quantum efficiencies larger than 90% have been typically observed from many fluoride phosphors (see, e.g., Ref. 197). Such red-emitting phosphors can, therefore, be used in w-LED lamps, leading to a significant reduction in the efficacy gap between warm and cool w-LED lamps employing down-conversion red-emitting Mn^{4+}-activated phosphors.
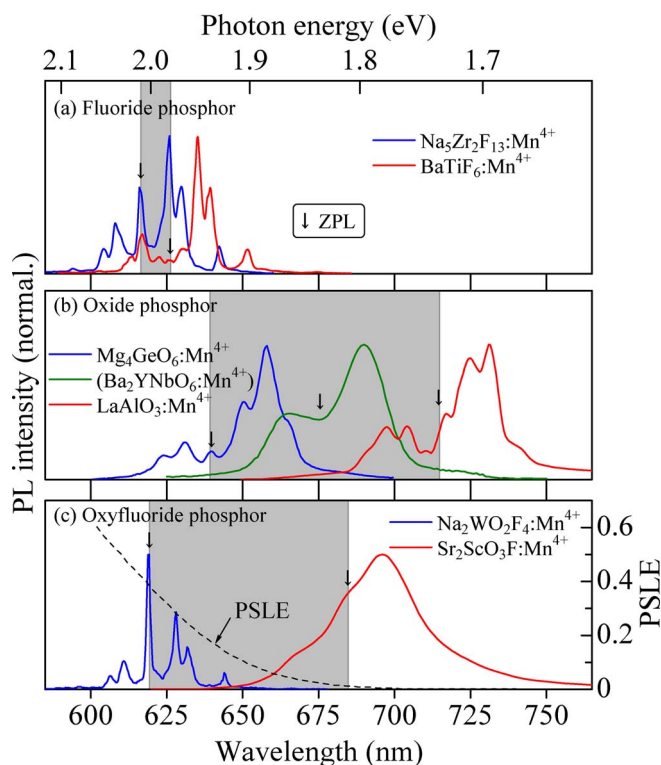
Because of its various applications as diverse as advertising signs, automotive headlamps, aviation lighting, camera flashes, lighted wallpaper, medical devices, room lighting, and traffic signals, a warm w-LED device becomes rapidly growing topic. Early w-LED device consists of an InGaN LED chip with blue light emission near 450 nm and a coating of yellow-emitting $YAG:Ce^{3+}$ phosphor with considerably broad emission band peaking at ∼ 580 nm (see Fig. 37b below). This type of w-LEDs suffers from a high CCT value (> 6000 K) with a low CRI (< 80). Recent advances with the use of red-emitting phosphors have yielded warm w-LEDs with CCT values ranging between 3000–4000 K and minimum CRI values of 80. If we use some Mn^{4+}-activated "oxide" phosphors, such warm w-LEDs are still less efficient than cool w-LEDs. This is because a large portion of the red emission from the oxide phosphors occurs above 700 nm, which is beyond the sensitivity of the human eye [i.e., the photopic spectral luminous efficiency (PSLE) in Fig. 36c]. From this view point, the Mn^{4+}-activated "fluoride" phosphors are more suitable than the "oxide" phosphors for use in warm w-LED applications (cf. Figs. 36a and 36b).

Figure 37 shows some typically observed luminescence and excitation transition (PLE) spectra at 300 K: (a) electroluminescence (EL) spectrum from InGaN blue-LED device, (b) PL and PLE spectra from $YAG:Ce^{3+}$ yellow-emitting phosphor, (c) PL and PLE spectra from $Rb_2SiF_6:Mn^{4+}$ red-emitting phosphor, (Ref. 197) and (d) EL spectrum from InGaN blue-LED device coated with yellow $YAG:Ce^{3+}$ and red $Rb_2SiF_6:Mn^{4+}$ phosphors. It is clear that the blue EL light from InGaN blue-LED can efficiently excite Ce^{3+} and Mn^{4+} activator ions, resulting in an overlapped spectrum of the broad yellow emission band and a series of the sharp red emission lines from the Ce^{3+}- and Mn^{4+}-activated phosphors, respectively. As a consequence, it is possible to obtain a warm w-LED device with greatly improved CCT and CRI values.
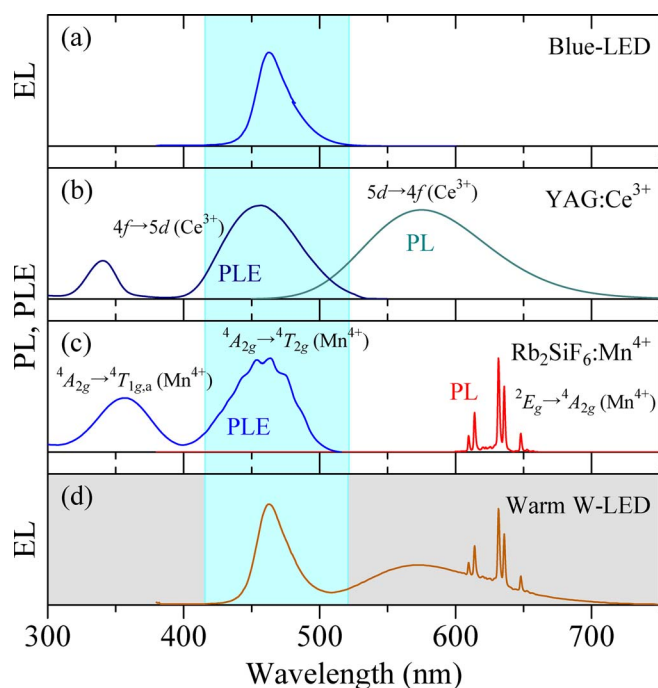
Figure 37. Some typically observed luminescence and excitation transition (PLE) spectra at 300 K: (a) EL spectrum from InGaN blue-LED device, (b) PL and PLE spectra from YAG:Ce^{3+} yellow-emitting phosphor, (c) PL and PLE spectra from Rb$_2$SiF$_6$:Mn^{4+} red-emitting phosphor, and (d) EL spectrum from InGaN blue-LED coated with yellow YAG:Ce^{3+} and red Rb$_2$SiF$_6$:Mn^{4+} phosphors. The PL and PLE spectra for the Rb$_2$SiF$_6$:Mn^{4+} fluoride phosphor (type F1) are taken from Ref. 197. The blue EL light emitted from the In-GaN blue-LED device can efficiently excite both the Ce^{3+} and Mn^{4+} ions in the yellow-emitting YAG:Ce^{3+} and red-emitting Rb$_2$SiF$_6$:Mn^{4+} phosphors, respectively, resulting in a warm white light available from this warm w-LED device.
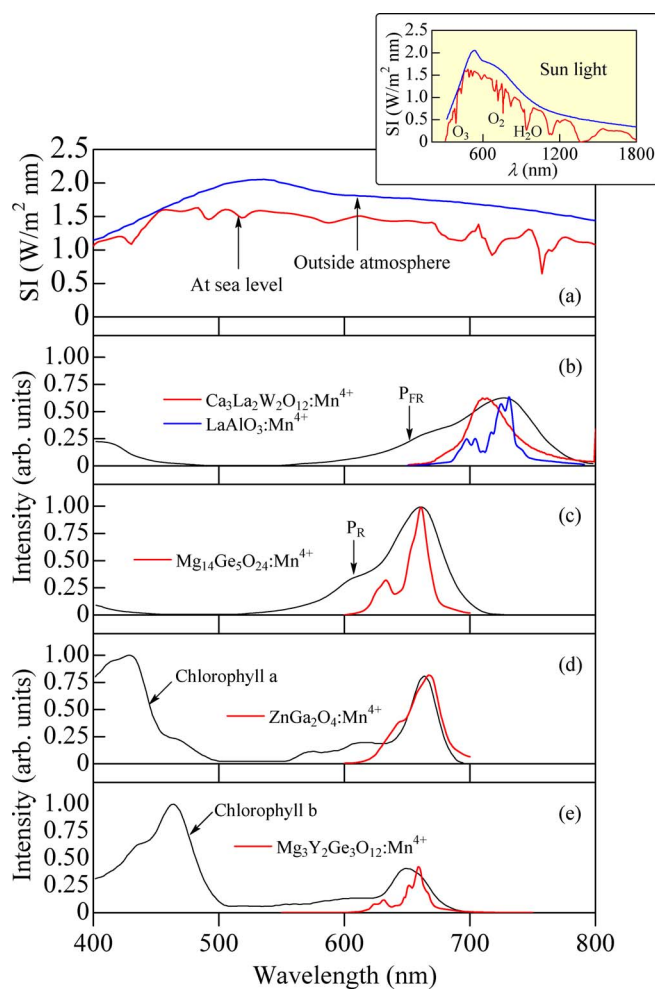

Figure 38. (a) Solar radiation spectra (SI = spectral irradiance) at both the top of the earth's atmosphere (AM0) and sea level (AM1.5), (b) PL spectra for the Ca$_3$La$_2$W$_2$O$_{12}$:Mn^{4+} (type O-A) (Ref. 166) and LaAlO$_3$:Mn^{4+} (type O-A) oxide phosphors (Ref. 194) along with phytochrome P$_{FR}$ absorption spectrum, (c) PL spectrum for the Mg$_{14}$Ge$_5$O$_{24}$:Mn^{4+} (type O-A) oxide phosphor[209] along with phytochrome P$_R$ absorption spectrum, (d) PL spectrum for the ZnGa$_2$O$_4$:Mn^{4+} (type O-A) oxide phosphor[211] along with chlorophyll a absorption spectrum, and (e) PL spectrum for the Mg$_3$Y$_2$Ge$_3$O$_{12}$:Mn^{4+} (type O-A) oxide phosphor[98] along with chlorophyll b absorption spectrum. All these PL spectra were measured at 300 K.

Indoor plant cultivation application.—There have been growing interest in use of a blue-emitting InGaN LED combined with a Mn^{4+}-activated "oxide" phosphor emitting a deep red light as plant photoreceptor. A blue light at ∼ 400–500 nm, a red light at ∼ 620–690 nm, and a deep red light at ∼ 700–740 nm are critical in the reactions of photosynthesis, phototropism, and photo-morphogenesis. Therefore, it is of great significance for fabricating suitable LED devices covering the spectral regions of blue, red, and deep red in order to offer an ideal lighting source for the plant factory and, as a result, the choice of phosphor holds the key to the success or failure of a plant factory.[117,166,182,198–206]

Figure 38a represents solar radiation spectra at both the top of the earth's atmosphere (AM0) and sea level (AM1.5). The energy flow within the sun results in a surface temperature of ∼ 5800 K, so the spectrum of the radiation from the sun is similar to that of a 5800 K blackbody with fine structures, namely, the Fraunhofer lines, due to absorption in the cool peripheral solar gas. Here, AM comes from "air mass." To a first approximation, the air mass is the secant of the solar zenith angle. Thus, AM1 indicates that the sun is directly overhead, and AM1.414 is a 45° zenith angle. As the sunlight passes through the atmosphere, some is absorbed by atomic and molecular gases, mainly O$_2$ and H$_2$O, with specific absorption lines and bands. There is the ozone layer, O$_3$, in the lower portion of the stratosphere from approximately 20 to 30 km above the earth's surface. The ozone layer absorbs ∼98% of the sun's UV radiation (200–320 nm), which otherwise would potentially damage exposed life forms on the earth. Additional light is redistributed by Rayleigh scattering given by $I_R \propto \lambda^{-4}$, which is responsible for the really red sunset and atmosphere's blue color.

Figures 38b and 38c show the absorption spectra of phytochrome P$_{FR}$ and P$_R$, respectively. Phytochromes are known to regulate the expression of many plant genes and may control plant development primarily through its role in regulating gene expression. They regulate the photoblasty, the synthesis of chlorophyll, the elongation of seedlings, the size, shape and number, and movement of leaves, and the timing of flowering in adult plants. Therefore, phytochromes are widely expressed across many tissues and developmental stages.

The phytochromes are reversibly photochromic proteins encoded in plants by a small nuclear gene family of 3 − 5 members.[207,208] They exist as red and far-red (or deep red) absorbing forms, P$_R$ and P$_{FR}$, with absorption of red light at ∼ 660 nm by P$_R$ triggering a conversion to the P$_{FR}$ form and absorption of far-red light at ∼ 730 nm converting P$_{FR}$ back to the P$_R$ form.[207] This photoconversion is mediated by the covalently-bound, linear tetrapyrrole chromophore, phytochromobilin, which is assembled in darkness to give the inactive P$_R$ form of phytochrome. Only following conversions to the active P$_{FR}$ form are responses such as promotion of germination and de-etiolation triggered. In addition to enabling the detection of light, the photoreversibility of phytochrome is the key to phytochrome's role in shade avoidance. Light reflected from a plant is depleted in red and blue wavelengths, but is rich in far-red light. As a consequence, the ma-

jority of the phytochrome pool is converted into the inactive P_R form. The loss of P_{FR} removes an inhibitor of elongation growth and triggers shade avoidance. The degree of shading is accurately reflected by the red / far-red ratio and this in turn determines the position of the P_R/P_{FR} equilibrium and the degree of elongation.[207]

In Figs. 38b and 38c, the PL spectra of some Mn^{4+}-activated oxide phosphors, $Ca_3La_2W_2O_{12}$:Mn^{4+} (P_{FR}),[166] $LaAlO_3$:Mn^{4+} (P_{FR}),[194] and $Mg_{14}Ge_5O_{24}$:Mn^{4+} (P_R)],[209] are plotted along with P_{FR} and P_R. From Fig. 5, one can understand that the maximum in the PL intensity $E_{PL,p}$ in many Mn^{4+}-activated phosphors occurs roughly at

$$E_{PL,p} \sim {}^2E_g - \frac{h\nu_4 + h\nu_6}{2} \qquad [48]$$

where ${}^2E_g = E({}^2E_g)_{ZPL}$ is the ZPL emission energy and $h\nu_4 \sim 44$ meV and $h\nu_6 \sim 30$ meV are the local vibronic energies of the Stokes mode (see "Vibration Frequencies of Mn^{4+} Ion in the Octahedron Molecule"). The ${}^2E_g$ values of the various Mn^{4+}-activated phosphors are listed in Tables II, IV, and V. The absorption peaks in P_{FR} and P_R of Figs. 38b and 38c occur at ~ 1.71 and ~ 1.92 eV, respectively. Thus, the values of ${}^2E_g$ required simply from Eq. 48 are ~ 1.75 eV (P_{FR}) and ~ 1.96 eV (P_R). These ${}^2E_g$ values for $Ca_3La_2W_2O_{12}$:Mn^{4+}, $LaAlO_3$:Mn^{4+}, and $Mg_{14}Ge_5O_{24}$:Mn^{4+} in Table IV are ~ 1.750, ~ 1.735, and ~ 1.924 eV, respectively. The experimental deep red and red emission spectra in Figs. 38b and 38c match very well with the absorption spectra of phytochromes P_{FR} and P_R. Therefore, the Mn^{4+}-activated "oxide" phosphors are very useful for future indoor plant cultivation and vegetable factory applications.

Chlorophyll has the second distinct absorption peak in the vicinity of 450 nm (blue light) other than the first peak in the vicinity of 660 nm (red light) in its light absorption spectrum.[210] They are roughly similar for different plants. Green plants can then be grown only by illuminating such blue and red monochromatic lights. Here, the blue light is indispensable to the morphologically healthy growth plant, whereas the red light contributes to the plant photosynthesis.

As shown in Fig. 38d, chlorophyll a absorbs energy from wavelengths of blue−violet light and orange−red light peaking at ~ 660 nm and reflects green light which gives "chlorophyll" its green appearance. It is very important in the energy phase of photosynthesis because chlorophyll a molecules are needed before photosynthesis can proceed. It is the primary photosynthetic pigment. Chlorophyll b complements chlorophyll a. Adding chlorophyll b to chlorophyll a increases the light absorption by increasing the range of wavelengths and broadening the absorbed light spectrum. If there is little light available, plants produce more chlorophyll b than chlorophyll a to increase its photosynthetic ability. This is required because chlorophyll a molecules capture a limited wavelength so accessory pigments like chlorophyll b are needed to aid in the capture of a wider range of light.

The red-emitting PL spectra in Figs. 38d and 38e are taken from $ZnGa_2O_4$:Mn^{4+} (Ref. 211) and $Mg_3Y_2Ge_3O_{12}$:Mn^{4+} phosphors, Ref. 98 respectively. The $E_{PL,p}$ (${}^2E_g$) values required in Eqs. 48 are ~ 1.87 eV (~ 1.91 eV) for chlorophyll a and ~ 1.91 eV (~ 1.95 eV) for chlorophyll b. It should be noted that the deep red emission color at $\lambda > 640$ nm is the spectral region possible from many "oxide" phosphors activated with Mn^{4+} ions (Table IV). The Mn^{4+}-activated oxide phosphors are, therefore, suitable for use in indoor plant cultivation applications. On the other hand, almost all the Mn^{4+}-activated "fluoride" phosphors emit very bright red light with wavelengths shorter than ~ 640 nm and can, therefore, be used for a variety of solid-state lighting systems fit well to the human eye responsibility.

Conclusions

The Mn^{4+}-activated phosphors have been the subject of considerable research and device development activity over the recent years. A number of important structural and luminescence properties of the Mn^{4+}-activated phosphors were reviewed. Firstly, the host materials of such phosphors were roughly classified into five groups simply from a materials kind of view: (i) fluorides, (ii) oxides, (iii) oxyfluorides, (iv)

hydroxy fluoride, and (v) alkali bifluoride. These five group phosphors were further classified into totally eleven subgroups from their different PL spectral features: (1) type F1, (2) type F2 (F = fluoride), (3) type O-A1, (4) type O-A2, (5) type O-B, (6) type O-C (O = oxide), (7) type OF-A1, (8) type OF-A2, (9) type OF-B (OF = oxyfluoride), (10) type HF [HF = hydroxy fluoride ($BaNb(OH)_{1.5}F_{5.5}$)], and (11) type AB [AB = alkali bifluoride ($NaHF_2$)]. The ZPL emission (${}^2E_g \rightarrow {}^4A_{2g}$) and absorption transition energies (${}^4T_{2g} \rightarrow {}^4A_{2g}$, ${}^4T_{1g,a} \rightarrow {}^4A_{2g}$, etc.) were determined from analyzing the PL and PLE spectra based on the Franck−Condon analysis method within the CC model for obtaining the crystal-field (Dq) and Racah parameters (B and C) of the Mn^{4+} ions in the host crystals. Temperature dependences of the PL intensity and luminescence lifetime were analyzed by considering the conventional thermal quenching model with taking into account the optical and acoustic phonon contributions in the intra-*d*-shell transition processes. The effects of hydrostatic pressure and Mn^{4+} dopant concentration on the PL properties were also discussed in detail. Finally, key properties of the Mn^{4+}-activated phosphors were considered for use of such red- and deep red-emitting phosphors in future warm w-LED and plant factory applications.

ORCID

Sadao Adachi https://orcid.org/0000-0002-2124-1757

References

1. S. Adachi, *J. Lumin.*, **197**, 119 (2018).
2. S. Adachi, *J. Lumin.*, **202**, 263 (2018).
3. Y. K. Xu and S. Adachi, *Phys. D: Appl. Phys.*, **39**, 4572 (2006).
4. S. Adachi and T. Kubota, *Electrochem. Solid-State Lett.*, **10**, H39 (2007).
5. Y. K. Xu and S. Adachi, *Appl. Phys.*, **101**, 103509 (2007).
6. S. Tomioka, T. Miyazaki, and S. Adachi, *Jpn. J. Appl. Phys.*, **46**, 5021 (2007).
7. S. Adachi and T. Takahashi, *J. Appl. Phys.*, **104**, 023512 (2008).
8. T. Takahashi and S. Adachi, *J. Electrochem. Soc.*, **155**, E183 (2008).
9. T. Arai and S. Adachi, *Jpn. J. Appl. Phys.*, **50**, 092401 (2011).
10. S. Shionoya and W. M. Yen, *Phosphor Handbook*, CRC Press, Boca Raton, FL (1999).
11. T. Nakamura, Z. Yuan, and S. Adachi, *Appl. Surf. Sci.*, **320**, 514 (2014).
12. S. Sugano, Y. Tanabe, and H. Kamimura, *Multiplets of Transition-Metal Ions in Crystals*, Academic Press, New York (1970).
13. M. Tamatani, in *Phosphor Handbook*, S. Shionoya and W. M. Yen, Editors, p. 153, CRC Press, Boca Raton, FL (1999).
14. A. M. Srivastava, M. G. Brik, H. A. Comanzo, W. W. Beers, W. E. Cohen, and T. Pocock, *ECS J. Solid State Sci. Technol.*, **7**, R3158 (2018).
15. D. B. Fitchen and W. B. Fowler, *Physics of Color Centers*, Academic Press, New York (1968).
16. H. Yamamoto, in *Phosphor Handbook*, S. Shionoya and W. M. Yen, Editors, p. 35, CRC Press, Boca Raton, FL (1999).
17. M. Grinberg and A. Suchocki, *J. Lumin.*, **125**, 97 (2007).
18. M. Tajima and M. Aoki, *Jpn. J. Appl. Phys.*, **13**, 812 (1974).
19. M. Tajima and M. Aoki, *Jpn. J. Appl. Phys.*, **14**, 1695 (1975).
20. R. Kasa and S. Adachi, *J. Electrochem. Soc.*, **159**, J89 (2012).
21. T. Arai and S. Adachi, *ECS J. Solid State Sci. Technol.*, **2**, R172 (2013).
22. H. F. Sijbom, R. Verstraete, J. J. Joos, D. Poelman, and P. F. Smet, *Opt. Mater. Express*, **7**, 3332 (2017).
23. M. G. Brik, S. J. Camardello, A. M. Srivastava, N. M. Avram, and A. Suchockic, *ECS J. Solid State Sci. Technol.*, **5**, R3067 (2016).
24. W.-L. Wu, M.-H. Fang, W. Zhou, T. Lesniewski, S. Mahlik, M. Grinberg, M. G. Brik, H.-S. Sheu, B.-M. Cheng, J. Wang, and R.-S. Liu, *Chem. Mater.*, **29**, 935 (2017).
25. Y. Jin, M.-H. Fang, M. Grinberg, S. Mahlik, T. Lesniewski, M. G. Brik, G.-Y. Luo, J. G. Lin, and R.-S. Liu, *ACS Appl. Mater. Interfaces*, **8**, 11194 (2016).
26. T. Sasaki, J. Fukushima, Y. Hayashi, and H. Takizawa, *J. Lumin.*, **188**, 101 (2017).
27. S. L. Chodos, A. M. Black, and C. D. Flint, *J. Chem. Phys.*, **65**, 4816 (1976).
28. M. D. Sturge, *Phys. Rev. B*, **1**, 1005 (1970).
29. Y. Takeda, H. Kato, M. Kobayashi, S. Nozawa, H. Kobayashi, and M. Kakihana, *J. Phys. Chem. C*, **121**, 18837 (2017).
30. T. Sasaki, J. Fukushima, Y. Hayashi, and H. Takizawa, *Ceram. Int.*, **43**, 7147 (2017).
31. Y. Jin, Y. Hu, H. Wu, H. Duan, L. Chen, Y. Fu, G. Ju, Z. Mu, and M. He, *Chem. Eng. J.*, **288**, 596 (2016).
32. J. Y. Park, J. S. Joo, H. K. Yang, and M. Kwak, *J. Alloys Compd.*, **714**, 390 (2017).
33. P. Cai, L. Qin, C. Chen, J. Wang, and H. J. Seo, *Dalton Trans.*, **46**, 14331 (2017).
34. P. Cai, X. Wang, and H. J. Seo, *Phys. Chem. Chem. Phys.*, **20**, 2028 (2018).
35. L. Thorington, *J. Opt. Soc. Am.*, **40**, 579 (1950).
36. Z. Yang, Q. Wei, N. Wang, Z. Yang, Q. Zhou, Z. Wang, and H. Liang, *ECS J. Solid State Sci. Technol.*, **6**, R139 (2017).
37. L. Xi, Y. Pan, M. Zhu, H. Lian, and J. Lin, *Dalton Trans.*, **46**, 13835 (2017).
38. L. Qin, S. Bi, P. Cai, C. Chen, J. Wang, S. I. Kim, Y. Huang, and H. J. Seo, *J. Alloys Compd.*, **755**, 61 (2018).

39. Y. Wu, Y. Zhuang, Y. Lv, K. Ruan, and R.-J. Xie, *J. Alloys Compd.*, **781**, 702 (2019).
40. G. Blasse and A. F. Corsmit, *J. Solid State Chem.*, **6**, 513 (1973).
41. K. Nakamoto, *Infrared and Raman Spectra of Inorganic and Coordination Compounds*, 6th ed., John Wiley & Sons, Hoboken (2009).
42. Y. K. Xu and S. Adachi, *J. Electrochem. Soc.*, **159**, E11 (2012).
43. S. Adachi, *Earth-Abundant Materials for Solar Cells: Cu2−II−IV−VI6 Semiconductors*, John Wiley & Sons, Chichester (2015).
44. R. Hoshino and S. Adachi, *J. Lumin.*, **162**, 63 (2015).
45. R. Hoshino and S. Adachi, *Opt. Mater.*, **48**, 36 (2015).
46. T. Hu, H. Lin, F. Lin, Y. Gao, Y. Cheng, J. Xua, and Y. Wang, *J. Mater. Chem. C*, **6**, 10845 (2018).
47. U. B. Humayoun, S. B. Kwon, S. K. Sami, and D.-H. Yoon, *J. Alloys Compd.*, **776**, 594 (2019).
48. L. Zhang, L. Xi, Y. Pan, Y. Jia, M. Wu, H. Lianc, and J. Lin, *Dalton Trans.*, **47**, 16516 (2018).
49. Y. Arai and S. Adachi, *J. Lumin.*, **131**, 2652 (2011).
50. Y. K. Xu and S. Adachi, *J. Electrochem. Soc.*, **158**, J58 (2011).
51. M. Kim, W. B. Park, B. Bang, C. H. Kim, and K.-S. Sohn, *J. Am. Ceram. Soc.*, **100**, 1044 (2017).
52. D. Sekiguchi, J. Nara, and S. Adachi, *J. Appl. Phys.*, **113**, 183516 (2013).
53. R. Hoshino and S. Adachi, *J. Appl. Phys.*, **114**, 213502 (2013).
54. M. Zhu, Y. Pan, M. Wu, H. Lian, and J. Lin, *Dalton Trans.*, **47**, 12944 (2018).
55. H. Zhu, C. C. Lin, W. Luo, S. Shu, Z. Liu, Y. Liu, J. Kong, E. Ma, Y. Cao, R.-S. Liu, and X. Chen, *Nat. Commun.*, **5**, 4312 (2014).
56. E. Song, J. Wang, J. Shi, T. Deng, S. Y., M. Peng, J. Wang, L. Wondraczek, and Q. Zhang, *ACS Appl. Mater. Interfaces*, **9**, 8805 (2017).
57. E. H. Song, J. Q. Wang, S. Ye, X. F. Jiang, M. Y. Peng, and Q. Y. Zhang, *J. Mater. Chem. C*, **4**, 2480 (2016).
58. T. T. Deng, E. H. Song, Y. Y. Zhou, L. Y. Wang, S. Ye, and Q. Y. Zhang, *J. Mater. Chem. C*, **5**, 9588 (2017).
59. Y. Zhu, L. Cao, M. G. Brik, X. Zhang, L. Huang, T. Xuan, and J. Wang, *J. Mater. Chem. C*, **5**, 6420 (2017).
60. M. Zhu, Y. Pan, L. Xi, H. Lian, and J. Lin, *J. Mater. Chem. C*, **5**, 10241 (2017).
61. T. T. Deng, E. H. Song, J. Su, Y. Y. Zhou, L. Y. Wang, S. Ye, and Q. Y. Zhang, *J. Mater. Chem. C*, **6**, 4418 (2018).
62. Y. K. Xu and S. Adachi, *J. Appl. Phys.*, **105**, 013525 (2009).
63. Y. Arai, T. Takahashi, and S. Adachi., *Opt. Mater.*, **32**, 1095 (2010). Note that this host material shows a structural phase transition or dehydration [see Y. Arai and S. Adachi, *J. Electrochem. Soc.*, **158**, J81 (2011)].
64. S. Adachi, H. Abe, R. Kasa, and T. Arai, *J. Electrochem. Soc.*, **159**, J34 (2012).
65. L. Xi, Y. Pan, M. Zhu, H. Lian, and J. Lin., *J. Mater. Chem. C*, **5**, 9255 (2017).
66. C. Jiang, M. Peng, A. M. Srivastava, L. Li, and M. G. Brik, *Inorg. Chem.*, **57**, 14705 (2018).
67. D. Chen, Y. Liu, J. Chen, H. Huang, J. Zhong, and Y. Zhu, *J. Mater. Chem. C*, **7**, 1321 (2019).
68. H. Tan, M. Rong, Y. Zhou, Z. Yang, Z. Wang, Q. Zhang, Q. Wang, and Q. Zhou, *Dalton Trans.*, **45**, 9654 (2016).
69. T. Jansen, J. Gorobez, and T. Jüstel, *ECS J. Solid State Sci. Technol.*, **7**, R111 (2018).
70. M.-H. Fang, T.-H. Yang, T. Lesniewski, C. Lee, S. Mahlik, M. Grinberg, V. K. Peterson, C. Didier, W. K. Pang, C. Su, and R.-S. Liu, *ACS Energy Lett.*, **4**, 527 (2019).
71. L. Xi, Y. Pan, S. Huang, H. Lian, and J. Lin, *Dalton Trans.*, **47**, 5614 (2018).
72. T. Jansen, F. Baur, and T. Jüstel, *J. Lumin.*, **192**, 644 (2017).
73. N. Kumada, S. Yanagida, T. Takei, and B. Hong, *Mater, Res, Bull.*, **115**, 170 (2019).
74. Z. Wang, N. Wang, Z. Yang, Z. Yang, Q. Wei, Q. Zhou, and H. Liang, *J. Lumin.*, **192**, 690 (2017).
75. L. Qin, P. Cai, C. Chen, J. Wang, and H. J. Seo, *RSC Adv.*, **7**, 49473 (2017).
76. M. Gu, Y. Tian, C. Cui, P. Huang, L. Wang, and Q. Shi, *Mater. Res. Bull.*, **107**, 242 (2018).
77. R. K. Chang, J. M. Ralston, and D. E. Keating, in *Light Scattering Spectra of Solids*, G. B. Wright, Editor, p. 369, Springer, Berlin (1969).
78. S. Adachi, *Properties of Group-IV, III−V and II−VI Semiconductors*, John Wiley & Sons, Chichester (2005).
79. P. H. M. Uylings, A. J. J. Raasen, and J. F. Wyart, *J. Phys. B*, **17**, 4103 (1984).
80. T. T. Deng, E. H. Song, Y. Y. Zhou, L. Y. Wang, and Q. Y. Zhang, *J. Mater. Chem. C*, **5**, 12422 (2017).
81. M. J. Reisfeld, N. A. Matwiyoff, and L. B. Asprey, *J. Mol. Spectrosc.*, **39**, 8 (1971).
82. Z. Lu, A. Fu, F. Gao, X. Zhang, and L. Zhou, *J. Lumin.*, **203**, 420 (2018).
83. A. Fu, Q. Pang, H. Yang, and L. Zhou, *Opt. Mater.*, **70**, 144 (2017).
84. A. M. Srivastava, S. J. Camardello, and M. G. Brik, *J. Lumin.*, **183**, 437 (2017).
85. F. Li, J. Cai, F. Chi, Y. Chen, C. Duan, and M. Yin, *Opt. Mater.*, **66**, 447 (2017).
86. F. Xue, Y. Hu., L. Chen, H. Wu, G. Ju, T. Wang, and L. Yang, *Ceram. Int.*, **43**, 15141 (2017).
87. R. Cao, Y. Ye, Q. Peng, T. Chen, H. Ao, F. Xiao, Z. Luo, and P. Liu, *J. Electron. Mater.*, **47**, 7537 (2018).
88. Y. Xu, Y. Zhang, L. Wang, M. Shi, L. Liu, and Y. Chen, *J. Mater. Sci.: Mater. Electron.*, **28**, 12032 (2017).
89. B. Wang, H. Lin, J. Xu, H. Chen, and Y. Wang, *ACS Appl. Mater. Interfaces*, **6**, 22905 (2014).
90. E. A. M. Srivastava and M. G. Brik, *Opt. Mater.*, **63**, 207 (2017).
91. P. Li, L. Wondraczek, M. Peng, and Q. Zhang, *J. Am. Ceram. Soc.*, **99**, 3376 (2016).
92. R. Cao, W. Wang, J. Zhang, S. Jiang, Z. Chen, W. Li, and X. Yu, *J. Alloy. Compd.*, **704**, 124 (2017).
93. M. Peng, X. Yin, P. A. Tanner, M. G. Brik, and P. Li, *Chem. Mater.*, **27**, 2938 (2015).
94. R. Cao, K. N. Sharafudeen, and J. Qiu, *Spectrochim. Acta A*, **117**, 402 (2014).
95. P. A. Tanner and Z. Pan, *Inorg. Chem.*, **48**, 11142 (2009).
96. T. Jansen, T. Jüstel, M. Kirm, S. Vielhauer, N. M. Khaidukov, and V. N. Makhov, *J. Lumin.*, **198**, 314 (2018).
97. T. Senden, F. T. H. Broers, and A. Meijerink, *Opt. Mater.*, **60**, 431 (2016).
98. T. Jansen, J. Gorobez, M. Kirm, M. G. Brik, S. Vielhauer, M. Oja, N. M. Khaidukov, V. N. Makhov, and T. Jüstel, *ECS J. Solid State Sci. Technol.*, **7**, R3086 (2018).
99. S. Zhang and Y. Hu, *J. Lumin.*, **177**, 394 (2016).
100. P. Li, M. Peng, X. Yin, Z. Ma, G. Dong, Q. Zhang, and J. Qiu, *Opt. Express*, **21**, 18943 (2013).
101. Y. X. Pan and G. K.Liu, *J. Lumin.*, **131**, 465 (2011) (PL spectra); see also Ref. 87 (PLE spectrum).
102. A. Brenier, A. Suchocki, C. Pedrini, G. Boulon, and C. Madej, *Phys. Rev. B*, **46**, 3219 (1992).
103. H. Chen, H. Lin, Q. Huang, F. Huang, J. Xu, B. Wang, Z. Lin, J. Zhou, and Y. Wang, *J. Mater. Chem. C*, **4**, 2374 (2016).
104. S. Zhang, Y. Hu, H. Duan, L. Chen, Y. Fu, G. Ju, T. Wang, and M. He, *RSC Adv.*, **5**, 90499 (2015).
105. L. Chen, X. Deng, E. Zhao, X. Chen, S. Xue, W. Zhang, S. Chen, Z. Zhao, W. Zhang, and T.-S. Chan, *J. Alloys Compd.*, **613**, 312 (2014).
106. T. Jansen and T. Jüstel, *J. Phys. Chem. Solids*, **110**, 180 (2017).
107. R. Cao, J. Zhang, W. Wang, Z. Hu, T. Chen, Y. Ye, and X. Yu, *Mater. Res. Bull.*, **87**, 109 (2017).
108. T. Chen, X. Yang, W. Xia, W. Li, and S. Xiao, *Ceram. Int.*, **43**, 6949 (2017).
109. S. Zhang, Y. Hu, H. Duan, Y. Fu, and M. He, *J. Alloys Compd.*, **693**, 315 (2017).
110. R. Cao, Z. Shi, G. Quan, T. Chen, S. Guo, Z. Hu, and P. Liu, *J. Lumin.*, **188**, 577 (2017).
111. R. Cao, J. Zhang, W. Wang, T. Chen, Q. Gou, Y. Wen, F. Xiao, and Z. Luo, *Opt. Mater.*, **66**, 293 (2017).
112. T. Hasegawa, S. W. Kim, T. Abe, S. Kumagai, R. Yamanashi, K. Seki, K. Uematsu, K. Toda, and M. Sato, *Chem. Lett.*, **45**, 1096 (2016).
113. C. Yang, Z. Zhang, G. Hu, R. Cao, X. Liang, and W. Xiang, *J. Alloys Compd.*, **694**, 1201 (2017).
114. R. Cao, F. Zhang, H. Xiao, T. Chen, S. Guo, G. Zheng, X. Yu, and T. Chen, *Inorg. Chim. Acta*, **483**, 593 (2018).
115. L. Wang, L. Yuan, Y. Xu, R. Zhou, B. Y. Qu, N. Ding, M. Shi, B. Zhang, Y. Chen, Y. Jiang, D. Wang, and J. Shi, *Appl. Phys. A*, **117**, 1777 (2014).
116. R. Cao, X. Cheng, L. Su, T. Chen, S. Guo, G. Zheng, H. Ao, and W. Li, *Mater. Res. Bull.*, **108**, 32 (2018).
117. Z. Zhou, J. Zheng, R. Shi, N. Zhang, J. Chen, R. Zhang, H. Suo, E. M. Goldys, and C. Guo, *ACS Appl. Mater. Interfaces*, **9**, 6177 (2017).
118. Y. Takeda, H. Kato, M. Kobayashi, H. Kobayashi, and M. Kakihana, *Chem. Lett.*, **44**, 1541 (2015).
119. F. B. Xiong, L. X. Lin, H. F. Lin, X. G. Meng, S. Y. Lian, and W. Z. Zhu, *Opt. Laser Technol.*, **117**, 299 (2019).
120. M. G. Brik, A. M. Srivastava, N. M. Avram, and A. Suchocki, *J. Lumin.*, **148**, 338 (2014).
121. M. G. Brik and A. M. Srivastava, *ECS J. Solid State Sci. Technol.*, **2**, R148 (2013).
122. S. Sakurai, T. Nakamura, and S. Adachi, *Jpn. J. Appl. Phys.*, **57**, 022601 (2018).
123. S. Adachi and C. Hamaguchi, *Phys. Rev. B*, **19**, 938 (1979).
124. S. Adachi and T. Takahashi, *J. Appl. Phys.*, **106**, 013516 (2009).
125. D. Sekiguchi and S. Adachi, *ECS J. Solid State Sci. Technol.*, **3**, R60 (2014).
126. Y. Zhydachevskii, A. Suchocki, A. Pajączkowska, A. Kłos, A. Szysiak, and A. Reszka, *Opt. Mater.*, **35**, 1664 (2013).
127. Y. Zhydachevskii, D. Galanciak, S. Kobyakov, M. Berkowski, A. Kamińska, A. Suchocki, Y. Zakharko, and A. Durygin, *J. Phys.: Condens. Matter*, **18**, 11385 (2006).
128. J. Nara and S. Adachi, *J. Appl. Phys.*, **113**, 033519 (2013).
129. Y. Tosaka and S. Adachi, *ECS J. Solid State Sci. Technol.*, **3**, R14 (2014).
130. M. Grinberg, *J. Lumin.*, **54**, 369 (1993).
131. T. Senden, R. J. A. van Dijk-Moes, and A. Meijerink, *Light: Sci. Appl.*, **7**, 8 (2018).
132. W. W. Beers, D. Smith, W. E. Cohen, and A. M. Srivastava, *Opt. Mater.*, **84**, 614 (2018).
133. A. Lazarowska, S. Mahlik, M. Grinberg, C. C. Lin, and R.-S. Liu, *J. Chem. Phys.*, **143**, 134704 (2015).
134. Y. Wang, T. Wen, L. Tang, L. Yang, W. Yang, and Y. Zhao, *Dalton Trans.*, **44**, 7578 (2015).
135. D. Galanciak, M. Grinberg, W. Gryk, S. Kobyakov, A. Suchocki, G. Boulon, and A. Brenier, *J. Phys.: Condens. Matter*, **17**, 7185 (2005).
136. M. G. Brik and A. M. Srivastava, *J. Electrochem. Soc.*, **159**, J212 (2012).
137. L. C. Prinsloo, A. M. Heyns, R. Ehrl, and K.-J. Range, *Eur. J. Solid State Inorg. Chem.*, **34**, 881 (1997).
138. C. M. Gramaccioli and I. Campostrini, *Can. Mineral.*, **45**, 1275 (2007).
139. L. Lv, X. Jiang, S. Huang, X. Chen, and Y. Pan, *J. Mater. Chem. C*, **2**, 3879 (2014).
140. J. H. Eggert, K. A. Goettel, and I. F. Silvera, *Phys. Rev. B*, **40**, 5724 (1989).
141. J. H. Eggert, K. A. Goettel, and I. F. Silvera, *Phys. Rev. B*, **40**, 5733 (1989).
142. B. R. Jovanić, *J. Lumin.*, **75**, 171 (1997).
143. N. Zhang, Y.-T. Tsai, M.-H. Fang, C.-G. Ma, A. Lazarowska, S. Mahlik, M. Grinberg, C.-Y. Chiang, W. Zhou, J. G. Lin, J.-F. Lee, J. Zheng, C. Guo, and R.-S. Liu, *ACS Appl. Mater. Interfaces*, **9**, 23995 (2017).
144. Y. Tokida and S. Adachi, *J. Appl. Phys.*, **112**, 063522 (2012).
145. K. T. Thomson, R. M. Wentzcovitch, and M. S. T. Bukowinski, *Science*, **274**, 1880 (1996).
146. W. Duan, R. M. Wentzcovitch, and K. T. Thomson, *Phys. Rev. B*, **57**, 10363 (1998).
147. N. Funamori and R. Jeanloz, *Science*, **278**, 1109 (1997).
148. X. Wu, S. Qin, and Z. Wu, *J. Phys.: Condens. Matter*, **18**, 3907 (2006).

149. M. A. Hernańdez-Rodríguez, V. Monteseguro, A. D. Lozano-Gorrín, F. J. Manjoń, J. Gonzaĺez-Platas, P. Rodríguez-Hernańdez, A. Munõz, V. Lavín, I. R. Martín, and U. R. Rodríguez-Mendoza, *J. Phys. Chem. C*, **121**, 15353 (2017).
150. T. Goto, O. L. Anderson, I. Ohono, and S. Yamamoto, *J. Geophys. Res.*, **94**, 7588 (1989).
151. A. Durygin, V. Drozd, W. Paszkowicz, E. Werner-Malento, R. Buczko, A. Kaminska, S. Saxena, and A. Suchocki, *Appl. Phys. Lett.*, **95**, 141902 (2009).
152. Z. Mao, S. M. Dorfman, S. R. Shieh, J. F. Lin, V. B. Prakapenka, Y. Meng, and T. S. Duffy, *Phys. Rev. B*, **83**, 054114 (2011).
153. W. J. Alton and A. J. Barlow, *J. Appl. Phys.*, **38**, 3023 (1967).
154. A. M. Hofmeister and K. R. Campbell, *J. Appl. Phys.*, **72**, 638 (1992).
155. P. R. Stoddart, P. E. Ngoepe, P. M. Mjwara, J. D. Comins, and G. A. Saunders, *J. Appl. Phys.*, **73**, 7298 (1993).
156. N. L. Ross, *Phase Transitions*, **58**, 27 (1996).
157. N. L. Ross, J. Zhao, and R. J. Angel, *J. Solid State Chem.*, **177**, 1276 (2004).
158. D. L. Dexter, *J. Chem. Phys.*, **21**, 836 (1953).
159. L. Y. Wang, E. H. Song, Y. Y. Zhou, T. T. Deng, S. Ye, and Q. Y. Zhang, *J. Mater. Chem. C*, **5**, 7253 (2017).
160. M. Kim, W. B. Park, B. Bang, C. H. Kim, and K.-S. Sohn, *J. Mater. Chem. C*, **3**, 5484 (2015).
161. C. Jiang, M. G. Brik, L. Li, L. Li, J. Peng, J. Wu, M. S. Molokeev, K.-L. Wong, and M. Peng, *J. Mater. Chem. C*, **6**, 3016 (2018).
162. H. Ming, S. Liu, L. Liu, J. Peng, J. Fu, F. Du, and X. Ye, *ACS Appl. Mater. Interfaces*, **10**, 19783 (2018).
163. F. Hong, H. Cheng, G. Liu, X. Dong, W. Yu, and J. Wang, *Inorg. Chem.*, **57**, 9892 (2018).
164. F. Hong, H. Cheng, C. Song, G. Liu, W. Yu, J. Wang, and X. Dong, *Dalton Trans.*, **48**, 1376 (2019).
165. Y. Liu, T. Wang, Z. Tan, J. Meng, W. Huang, Y. Huang, S. Liao, and H. Zhang, *Ceram. Int.*, **45**, 6243 (2019).
166. X. Huang and H. Guo, *Dyes Pigm.*, **152**, 36 (2018).
167. R. Cao, F. Zhang, C. Caoa, X. Yu, A. Liang, S. Guo, and H. Xue, *Opt. Mater.*, **38**, 53 (2014).
168. R. Cao, Q. Xiong, W. Luo, D. Wu, F. Xiao, and X. Yu, *Ceram. Int.*, **41**, 7191 (2015).
169. K. Li and R. Van Deun, *Dyes Pigm.*, **162**, 990 (2019).
170. Q. Sun, S. Wang, B. Devakumar, L. Sun, J. Liang, and X. Huang, *RSC Adv.*, **9**, 3303 (2019).
171. S. Wang, Q. Sun, B. Devakumar, J. Liang, L. Sun, and X. Huang, *RSC Adv.*, **9**, 3429 (2019).
172. L. Shi, Y. Han, Y. Zhao, M. Li, X. Geng, Z. Zhang, and L. Wang, *Opt. Mater.*, **89**, 609 (2019).
173. X. Ding, G. Zhu, W. Geng, Q. Wang, and Y. Wang, *Inorg. Chem.*, **55**, 154 (2016).
174. A. Fu, C. Zhou, Q. Chen, Z. Lu, T. Huang, H. Wang, and L. Zhou, *Ceram. Int.*, **43**, 6353 (2017).
175. X. Ding and Y. Wang, *Opt. Mater.*, **64**, 445 (2017).
176. K. Li, H. Lian, and R. Van Deun, *J. Lumin.*, **198**, 155 (2018).
177. A. Fu, L. Zhou, S. Wang, and Y. Li, *Dyes Pigm.*, **148**, 9 (2018).
178. F. Mo, Z. Lu, and L. Zhou, *J. Lumin.*, **205**, 393 (2019).
179. J. Zhong, X. Chen, D. Chen, M. Liu, Y. Zhu, X. Li, and Z. Ji, *J. Alloys Compd.*, **773**, 413 (2019).
180. L. Shi, Y. Han, Z. Zhang, Z. Ji, D. Shi, X. Geng, H. Zhang, M. Li, and Z. Zhang, *Ceram. Int.*, **45**, 4739 (2019).
181. R. Cao, T. Chen, Y. Ren, T. Chen, H. Ao, W. Li, and G. Zheng, *J. Alloys Compd.*, **780**, 749 (2019).
182. X. Li, Z. Chen, B. Wang, R. Liang, Y. Li, L. Kang, and P. Liu, *Materials*, **12**, 86 (2019).
183. K. Li, H. Lian, R. Van Deun, and M. G. Brik, *Dyes Pigm.*, **162**, 214 (2019).
184. L. Shi, J. Li, Y. Han, W. Li, and Z. Zhang, *J. Lumin.*, **208**, 201 (2019).
185. C. Jiang, X. Zhang, J. Wang, Q. Zhao, K.-L. Wong, and M. Peng, *J. Am. Ceram. Soc.*, **102**, 1269 (2019).
186. L. Shi, Y. Han, Z. Ji, and Z. Zhang, *J. Mater. Sci.: Mater. Electron.*, **30**, 3107 (2019).
187. K. Li, D. Mara, and R. Van Deun, *Dalton Trans.*, **48**, 3187 (2019).
188. J. Liang, B. Devakumar, L. Sun, Q. Sun, S. Wang, and X. Huang, *J. Am. Ceram. Soc.*, **102**, 4730 (2019).
189. R. Cao, X. Ouyang, Y. Jiao, X. Wang, Q. Hu, T. Chen, C. Liao, and Y. Li, *J. Alloys Compd.*, **795**, 134 (2019).
190. Q. Wang, J. Liao, L. Kong, B. Qiu, J. Li, H. Huang, and H. Wen, *J. Alloys Compd.*, **772**, 499 (2019).
191. T. Hu, H. Lin, Y. Gao, J. Xu, J. Wang, X. Xiang, and Y. Wang, *J. Am. Ceram. Soc.*, **101**, 3437 (2018).
192. H. Ming, J. Zhang, L. Liu, J. Peng, F. Du, X. Ye, Y. Yang, and H. Nie, *Dalton Trans.*, **47**, 16048 (2018).
193. A. Ali, L. S. Khanzada, A. Hashemi, C. Polzer, A. Osvet, C. Brabec, and M. Batentschuk, *J. Alloys Comdl.*, **734**, 29 (2018).
194. Y. Li, Y.-Y. Li, K. Sharafudeen, G.-P. Dong, S.-F. Zhou, Z.-J. Ma, M.-Y. Peng, and J.-R. Qiu, *J. Mater. Chem. C*, **2**, 2019 (2014).
195. H. Kato, Y. Takeda, M. Kobayashi, H. Kobayashi, and M. Kakihana, *Front. Chem.*, **6**, 467 (2018).
196. T. Jansen, L. M. Funke, J. Gorobez, D. Böhnisch, R.-D. Hoffmann, L. Heletta, R. Pöttgen, M. R. Hansen, T. Jüstel, and H. Eckert, *Dalton Trans.*, **48**, 5361 (2019).
197. S. Sakurai, T. Nakamura, and S. Adachi, *ECS J. Solid State Sci. Technol.*, **5**, R206 (2016).
198. Z. Zhou, B. Wang, Y. Zhong, W. Zhang, Y. Zhang, P. Gao, and N. Zhou, *Ceram. Int.*, **44**, 19779 (2018).
199. J. Deng, H. Zhang, X. Zhang, Y. Zheng, J. Yuan, H. Liu, Y. Liu, B. Lei, and J. Qiu, *J. Mater. Chem. C*, **6**, 1738 (2018).
200. Y. Zhu, Z. Qiu, B. Ai, Y. Lin, W. Zhou, J. Zhang, L. Yu, Q. Mi, and S. Lian, *J. Lumin.*, **201**, 314 (2018).
201. Q. Sun, S. Wang, B. Li, H. Guo, and X. Huang, *J. Lumin.*, **203**, 371 (2018).
202. J. Xiang, J. Chen, N. Zhang, H. Yao, and C. Guo, *Dyes Pigm.*, **154**, 257 (2018).
203. J. Long, X. Yuan, C. Ma, M. Du, X. Ma, Z. Wen, R. Ma, Y. Wang, and Y. Cao, *RSC Adv.*, **8**, 1469 (2018).
204. S. Wang, Q. Sun, B. Devakumar, L. Sun, J. Liang, and X. Huang, *RSC Adv.*, **8**, 30191 (2018).
205. J. Liang, L. Sun, B. Devakumar, S. Wang, Q. Sun, H. Guo, B. Li, and X. Huang, *RSC Adv.*, **8**, 31666 (2018).
206. L. Shi, Y. Han, H. Wang, D. Shi, X. Geng, and Z. Zhang, *J. Lumin.*, **208**, 307 (2019).
207. P. F. Devlin, J. M. Christie, and M. J. Terry, *J. Exp. Bot.*, **58**, 3071 (2007).
208. G. D. Massa, H.-H. Kim, R. M. Wheeler, and C. A. Mitchell, *HortScience*, **43**, 1951 (2008).
209. S. J. Lee, J. Jung, J. Y. Park, H. M. Jang, Y.-R. Kim, and J. K. Park, *Mater. Lett.*, **111**, 108 (2013).
210. K. Okamoto, T. Yanagi, S. Takita, M. Tanaka, T. Higuchi, Y. Ushida, and H. Watanabe, *Acta Hortic.*, **440**, 111 (1996).
211. C. F. Yu and P. Lin, *J. Appl. Phys.*, **79**, 7191 (1996).
212. M. Zhu, Y. Pan, M. Wu, H. Lian, and J. Lin, *J. Alloys Compd.*, **774**, 331 (2019).
213. T. T. Deng, E. H. Song, J. Sun, L. Y. Wang, Y. Deng, S. Ye, J. Wang, and Q. Y. Zhang, *J. Mater. Chem. C*, **5**, 2910 (2017).
214. T. Deng, E. Song, Y. Zhou, and J. Yuan, *J. Alloys Compd.*, **795**, 453 (2019).
215. H. Ming, J. Zhang, L. Liu, J. Peng, F. Du, and X. Ye, *ECS J. Solid State Sci. Technol.*, **7**, R149 (2018).
216. M. Zhu, Y. Pan, Y. Huang, H. Lian, and J. Lin, *J. Mater. Chem. C*, **6**, 491 (2018).
217. Y. Zhu, L. Huang, R. Zou, J. Zhang, J. Yu, M. Wu, J. Wang, and Q. Su, *J. Mater. Chem. C*, **4**, 5690 (2016).
218. Y. Zhu, J. Yu, Y. Liu, M. G. Brik, L. Huang, T. Xuan, and J. Wang, *RSC Adv.*, **7**, 30588 (2017).
219. H. Cheng, F. Hong, G. Liu, D. Li, Q. Ma, X. Dong, and W. Yu, *J. Lumin.*, **210**, 146 (2019).
220. C. Stoll, J. Bandemehr, F. Kraus, M. Seibald, D. Baumann, M. J. Schmidberger, and H. Huppertz, *Inorg. Chem.*, **58**, 5518 (2019).
221. Z. Wang, Y. Liu, Y. Zhou, Q. Zhou, H. Tan, Q. Zhang, and J. Peng, *RSC Adv.*, **5**, 58136 (2015); see also Ref. 62.
222. R. Kasa and S. Adachi, *J. Appl. Phys.*, **112**, 013506 (2012).
223. R. Kasa, Y. Arai, T. Takahashi, and S. Adachi, *J. Appl. Phys.*, **108**, 113503 (2010).
224. C. Jiang, M. G. Brik, A. M. Srivastava, L. Li, and M. Peng, *J. Mater. Chem. C*, **7**, 247 (2019).
225. Z. Yang, Q. Wei, M. Rong, Z. Yang, Z. Wang, Q. Zhou, and Q. Wang, *Dalton Trans.*, **46**, 9451 (2017).
226. Y. Arai and S. Adachi, *J. Electrochem. Soc.*, **158**, J179 (2011).
227. Q. Zhou, H. Tan, Y. Zhou, Q. Zhang, Z. Wang, J. Yan, and M. Wu, *J. Mater. Chem. C*, **4**, 7443 (2016).
228. M. Zhu, Y. Pan, X. Chen, H. Lian, and J. Lin, *J. Am. Ceram. Soc.*, **101**, 4983 (2018).
229. L. Xi, Y. Pan, M. Zhu, H. Lian, and J. Lin, *J. Mater. Chem. C*, **5**, 9255 (2017).
230. M.-H. Fang, W.-L. Wu, Y. Jin, T. Lesniewski, S. Mahlik, M. Grinberg, M. G. Brik, A. M. Srivastava, C.-Y. Chiang, W. Zhou, D. Jeong, S. H. Kim, G. Leniec, S. M. Kaczmarek, H.-S. Sheu, and R.-S. Liu, *Angew. Chem. Int. Ed.*, **57**, 1797 (2018) ($x = 0.5$). Note that Na_2SiF_6, Na_2GeF_6, and Na_2TiF_6 crystallize in the trigonal structure with the space group *P*321 (150). Their mixed alkali-metal hexafluorides exhibited the XRD patterns almost the same as those for the end-point complex materials (Na_2SiF_6, Na_2GeF_6, and Na_2TiF_6). Therefore, it is possible to conclude that such mixed alkali-metal hexafluorides can also crystalize in the trigonal structure with the space group *P*321 (150).
231. Y. Jin, R. Liu, G. Chen, Y. Liu, X. Ma, L. Shao, and L. Wang, *J. Rare Earths*, **34**, 1173 (2016).
232. Q. Wei, Z. Yang, Z. Yang, Q. Zhou, and Z. Wang, *ECS J. Solid State Sci. Technol.*, **7**, R39 (2018).
233. M. Kim, W. B. Park, J.-W. Lee, J. Lee, C. H. Kim, S. P. Singh, and K.-S. Sohn, *Chem. Mater.*, **30**, 6936 (2018).
234. D. Sekiguchi and S. Adachi, *Opt. Mater.*, **42**, 417 (2015).
235. R. Hoshino, T. Nakamura, and S. Adachi, *ECS J. Solid State Sci. Technol.*, **5**, R37 (2016).
236. R. Hoshino, S. Sakurai, T. Nakamura, and S. Adachi, *J. Lumin.*, **184**, 160 (2017).
237. S. Geschwind, P. Kisliuk, M. P. Klein, J. P. Remeika, and D. L. Wood, *Phys. Rev.*, **126**, 1684 (1962) [$T = 77$ K (PL)].
238. Y. Xu, L. Wang, B. Qu, D. Li, J. Lu, and R. Zhou, *J. Am. Ceram. Soc.*, **102**, 2737 (2019).
239. S. Fu and L. Tian, *Optik*, **183**, 635 (2019).
240. J. Zhong, S. Zhou, D. hen, J. Li, Y. Zhu, X. Li, L Chen, and Z. Ji, *Dalton Trans.*, **47**, 8248 (2018).
241. S. Liang, M. Shang, H. Lian, K. Li, Y. Zhang, and J. Lin, *J. Mater. Chem. C*, **4**, 6409 (2016).
242. R. Cao, W. Luo, Q. Xiong, S. Jiang, Z. Luo, and J. Fu,, *Chem. Lett.*, **44**, 1422 (2015).
243. B. Wang, H. Lin, F. Huang, J. Xu, H. Chen, Z. Lin, and Y. Wang, *Chem. Mater.*, **28**, 3515 (2016).
244. Q. Peng, R. Cao, Y. Ye, S. Guo, Z. Hu, T. Chen, and G. Zheng, *J. Alloys Compd.*, **725**, 139 (2017).
245. Q. Sun, S. Wang, B. Devakumar, B. Li, L. Sun, J. Liang, and X. Huang, *RSC Adv.*, **8**, 28538 (2018).
246. T. Sasaki, J. Fukushima, Y. Hayashi, and H. Takizawa, *Chem. Lett.*, **43**, 1061 (2014).
247. R. Cao, Y. Ye, Q. Peng, G. Zheng, H. Ao, J. Fu, Y. Guo, and B. Guo, *Dyes Pigm.*, **146**, 14 (2017).

248. J. Zhong, D. Chen, S. Yuan, M. Liu, Y. Yuan, Y. Zhu, X. Li, and Z. Ji, *Inorg. Chem.*, **57**, 8978 (2018).
249. R. Cao, C. An, and L. Tian, *J. Lumin.*, **210**, 66 (2019).
250. J. Hu, Y. Zhao, B. Chen, H. Xia, Y. Zhang, and H. Ye, *Ceram. Int.*, **44**, 20220 (2018).
251. J. Park, G. Kim, and Y. J. Kim, *Ceram. Int.*, **39**, S623 (2013).
252. T. Murata, T. Tanoue, M. Iwasaki, K. Morinaga, and T. Hase, *J. Lumin.*, **114**, 207 (2005).
253. K. Luo, Y. Zhang, J. Xu, J. Yuan, L. Huang, and D. Xiang, *J. Mater. Sci.: Mater. Electron.*, **30**, 9903 (2019).
254. Z. Lu, T. Huang, R. Deng, H. Wang, L. Wen, M. Huang, L. Zhou, and C. Yao, *Superlattices Microstruct.*, **117**, 476 (2018).
255. Z. Lu, H. Wang, D. Yu, T. Huang, L. Wen, M. Huang, L. Zhou, and Q. Wang, *Opt. Laser Technol.*, **108**, 116 (2018) ($\lambda_{ex} = 355$ nm).
256. G. Jiang, B. Yang, G. Zhao, Y. Liu, J. Zou, H. Sun, H. Ou, Y. Fang, and J. Hou, *Opt. Mater.*, **83**, 93 (2018).
257. T. Jansen, T. Jüstel, M. Kirm, J. Kozlova, H. Mändar, S. Vielhauer, N. M. Khaidukovc, and V. N. Makhov, *Opt. Mater.*, **84**, 600 (2018) ($T = 3$ K).
258. V. Đorđević, M. G. Brik, A. M. Srivastava, M. Medić, P. Vulić, E. Glais, B. Viana, and M. D. Dramićanin, *Opt. Mater.*, **74**, 46 (2017).
259. Y. Chen, M. Wang, J. Wang, M. Wu, and C. Wang, *J. Solid State Light.*, **1**, 15 (2014).
260. Q. Sun, B. Li, S. Wang, H. Guo, and X. Huang, *J. Mater. Sci.: Mater. Electron.*, **29**, 12972 (2018).
261. J. Zhong, D. Chen, X. Chen, K. Wang, X. Li, Y. Zhu, and Z. Ji, *Dalton Trans.*, **47**, 6528 (2018).
262. G. Blasse and P. H. M. de Korte, *J. Inorg. Nucl. Chem.*, **43**, 1505 (1981) ($T = 77$ K).
263. S. V. Bulyarskii, A. V. Zhukov, and V. V. Prikhod'ko, *Tech. Phys. Lett.*, **28**, 475 (2002).
264. W. Xu, D. Chen, S. Yuan, Y. Zhou, and S. Li, *Chem. Eng. J.*, **317**, 854 (2017).
265. A. M. Srivastava and W. W. Beers, *J. Electrochem. Soc.*, **143**, L203 (1996) ($T = 10$ K).
266. K. Li, D. Zhu, and R. Van Deun, *Dyes Pigm.*, **142**, 69 (2017).
267. F. Baur and T. Jüstel, *J. Lumin.*, **177**, 354 (2016).
268. R. Cao, D. Ceng, X. Yu, S. Guo, Y. Wen, and G. Zheng, *Funct. Mater. Lett.*, **8**, 1550046 (2015).
269. K. Li, H. Lian, and R. Van Deun, *Dalton Trans.*, **47**, 2501 (2018).
270. J. Liang, B. Devakumar, L. Sun, Q. Sun, S. Wang, B. Li, D. Chen, and X. Huang, *Ceram. Int.*, **45**, 4564 (2019).
271. A. M. Srivastava and M. G. Brik, *Opt. Mater.*, **35**, 1544 (2013) ($T = 4.2$ K).
272. A. M. Srivastava, H. A. Comanzo, D. J. Smith, J. W. Choi, M. G. Brik, W. W. Beerse, and S. A. Payne, *J. Lumin.*, **206**, 398 (2019) ($T = 13$ K).
273. K. Seki, K. Uematsu, T. Ishigaki, K. Toda, and M. Sato, *J. Ceram. Proc. Res.*, **12**, s286 (2011).
274. X. Zhang, J. Nie, S. Liu, Y. Li, and J. Qiu, *J. Am. Ceram. Soc.*, **101**, 1576 (2018).
275. M. Aoyama, Y. Amano, K. Inoue, S. Honda, S. Hashimoto, and Y. Iwamoto, *J. Lumin.*, **136**, 411 (2013).
276. R. Cao, W. Luo, Q. Xiong, A. Liang, S. Jiang, and Y. Xu, *J. Alloys Compd.*, **648**, 937 (2015).
277. R. J. M. da Fonseca and T. Abritta, *Physica B*, **190**, 327 (1993) [$T = 77$ K (PL); $T = 15$ K (PLE)].
278. R. Cao, Z. Huang, X. Ceng, Z. Luo, W. Ruan, and Q. Hu, *Ceram. Int.*, **42**, 13296 (2016).
279. Y. Odawara, Y. Takahashi, Y. Yamazaki, N. Terakado, and T. Fujiwara, *J. Ceram. Soc. Jpn.*, **125**, 378 (2017).
280. J. Liang, L. Sun, B. Devakumar, S. Wang, Q. Sun, H. Guo, B. Li, and X. Huang, *RSC Adv.*, **8**, 27144 (2018).
281. R. Cao, Z. Shi, G. Quan, Z. Luo, P. Tang, H. Ao, and X. Yu, *Opt. Mater.*, **57**, 212 (2016).
282. R. Suzuki, J. Kunitomo, Y. Takahashi, K. Nakamura, M. Osada, N. Terakado, and T. Fujiwara, *J. Ceram. Soc. Jpn.*, **123**, 888 (2015).
283. P. Li, L. Tan, L. Wang, J. Zheng, M. Peng, and Y. Wang, *J. Am. Ceram. Soc.*, **99**, 2029 (2016).
284. S. P. Singh, M. Kim, W. B. Park, J.-W. Lee, and K.-S. Sohn, *Inorg. Chem.*, **55**, 10310 (2016).
285. K. Seki, S. Kamei, K. Uematsu, T. Ishigaki, K. Toda, and M. Sato, *J. Ceram. Process. Res.*, **14**, s67 (2013).
286. R. Cao, X. Liu, K. Bai, T. Chen, S. Guo, Z. Hu, F. Xiao, and Z. Luo, *J. Lumin.*, **197**, 169 (2018).
287. J. Long, Y. Wang, R. Ma, C. Ma, X. Yuan, Z. Wen, M. Du, and Y. Cao, *Inorg. Chem.*, **56**, 3269 (2017).
288. L.-L. Peng, S.-X. Cao, C. Zhao, B.-T. Liu, T. Han, F. Li, and X.-M. Li, *Acta Phys. Sin.*, **67**, 187801 (2018).
289. T. Sasaki, J. Fukushima, Y. Hayashi, and H. Takizawa, *J. Lumin.*, **187**, 540 (2017).
290. M. Travniçek et al., *Physica*, **18**, 33 (1952).
291. C. Wu, J. Li, H. Xu, J. Wu, J. Zhang, Z. Ci, L. Feng, C. Cao, Z. Zhang, and Y. Wang, *J. Alloys Compd.*, **646**, 734 (2015).
292. A. V. Shamshurin, N. P. Efryushina, and A. V. Repin, *Inorg. Mater.*, **36**, 629 (2000).
293. Q. Huang, W. Ye, G. Hu, X. Jiao, and X. Liu, *J. Lumin.*, **194**, 557 (2018).
294. L. Lv, S. Wang, X. Wang, and L. Han, *J. Alloys Compd.*, **750**, 543 (2018).
295. Z. Qiu, T. Luo, J. Zhang, W. Zhou, L. Yu, and S. Lian, *J. Lumin.*, **158**, 130 (2015).
296. G. Hu, X. Hu, W. Chen, Y. Cheng, Z. Liu, Y. Zhang, X. Liang, and W. Xiang, *Mater. Res. Bull.*, **95**, 277 (2017).
297. P. Cai, L. Qin, C. Chen, J. Wang, S. Bi, S. I. Kim, Y. Huang, and H. J. Seo, *Inorg. Chem.*, **57**, 3073 (2018).
298. A. M. Srivastava, M. G. Brik, S. J. Camardello, H. A. Comanzo, and F. Garcia-Santamaria, *Z. Naturforsch. B*, **69**, 141 (2014) ($T = 10$ K).
299. X. Huang, J. Liang, B. Li, L. Sun, and J. Lin, *Opt. Lett.*, **43**, 3305 (2018).
300. L. Wang, Y. Xu, D. Wang, R. Zhou, N. Ding, M. Shi, Y. Chen, Y. Jiang, and Y. Wang, *Phys. Status Solidi A*, **210**, 1433 (2013).
301. T. Sasaki, J. Fukushima, Y. Hayashi, and H. Takizawa, *J. Lumin.*, **194**, 446 (2018).
302. Y. D. Xu, D. Wang, L. Wang, N. Ding, M. Shi, J. G. Zhong, and S. Qi, *J. Alloys Compd.*, **550**, 226 (2013).
303. W. Shen, Y. Liu, and Z. Wang, *Mater. Lett.*, **161**, 140 (2015).
304. R. Suzuki, Y. Takahashi, K. Iwasaki, N. Terakado, and T. Fujiwara, *Appl. Phys. Express*, **8**, 072603 (2015).
305. S. J. Kim, H. S. Jang, S. Unithrattil, Y. H. Kim, and W. B. Im, *J. Lumin.*, **172**, 99 (2016).
306. Y. Jin, Y. Fu, Y. Hu, L. Chen, H. Wu, G. Ju, M. He, and T. Wang, *Powder Technol.*, **292**, 74 (2016).
307. A. Fu, A. Guan, D. Yu, S. Xia, F. Gao, X. Zhang, L. Zhou, Y. Li, and R. Li, *Mater. Res. Bull.*, **88**, 258 (2017).
308. U. B. Humayoun, S. N. Tiruneh, and D.-H. Yoon, *Dyes Pigm.*, **152**, 127 (2018).
309. L. Meng, L. Liang, and Y. Wen, *J. Mater. Sci.: Mater. Electron.*, **25**, 2676 (2014).
310. R. Cao, M. Peng, E. Song, and J. Qiu, *ECS J. Solid State Sci. Technol.*, **1**, R123 (2012).
311. H. Zhang, H. Zhang, J. Zhuang, H. Dong, Y. Zhu, X. Ye, Y. Liu, and B. Lei, *Ceram. Int.*, **42**, 13011 (2016).
312. W. Chen, Y. Cheng, L. Shen, C. Shen, X. Liang, and W. Xiang, *J. Alloys Compd.*, **762**, 688 (2018).
313. X. Gu, Z. He, and X.-Y. Sun, *Chem. Phys. Lett.*, **707**, 129 (2018).
314. D. Kim, S. Park, B. C. Choi, S. H. Park, J. H. Jeong, and J. H. Kim, *Mater. Res. Bull.*, **97**, 115 (2018).
315. Z. Bryknar, V. Trepakov, Z. Potůček, and L. Jastrabík, *J. Lumin.*, **87−89**, 605 (2000) [$T = 13$ K (PL); $T = 77$ K (PLE)].
316. Z. Lu, X. Zhang, M. Huang, L. Wen, H. Wang, T. Huang, and L. Zhou, *J. Mater. Sci.: Mater. Electron.*, **29**, 17931 (2018).
317. R. Cao, X. Ceng, J. Huang, H. Ao, G. Zheng, X. Yu, and X. Zhang, *Opt. Mater.*, **62**, 706 (2016).
318. R. Cao, X. Ceng, J. Huang, X. Xia, S. Guo, and J. Fu, *Ceram. Int.*, **42**, 16817 (2016).
319. M. G. Brik, A. M. Srivastava, and N. M. Avram, *Opt. Mater.*, **33**, 1671 (2011) ($T = 10$ K).
320. R. Cao, W. Luo, H. Xu, Z. Luo, Q. Hu, T. Fu, and D. Peng, *Opt. Mater.*, **53**, 169 (2016).
321. R. Dittmann and D. Hahn, *Z. Phys.*, **207**, 484 (1967); R. Dittmann, *Z. Phys.*, **216**, 183 (1968) ($T = 4.2$ K).
322. X. Dong, Y. Pan, D. Li, H. Lian, and J. Lin, *CrystEngComm*, **20**, 5641 (2018).
323. Z. Liang, Z. Yang, H. Tang, J. Guo, Z. Yang, Q. Zhou, S. Tang, and Z. Wang, *Opt. Mater.*, **90**, 89 (2019).
324. Q. Wang, Z. Yang, H. Wang, Z. Chen, H. Yang, J. Yang, and Z. Wang, *Opt. Mater.*, **85**, 96 (2018).
325. Y. Zhou, S. Zhang, X. Wang, and H. Jiao, *Inorg. Chem.*, **58**, 4412 (2019).
326. T.-G. Kim, T. Kim, Y.-S. Kim, and S.-J. Im, *J. Electrochem. Soc.*, **157**, J397 (2010).
327. Q. Shao, H. Lin, J. Hu, Y. Dong, and J. Jiang, *J. Alloys Compd.*, **552**, 370 (2013).
328. Commercial phosphor [A. M. Srivastava, *Opt. Mater.*, **79**, 206 (2018)].
329. T. Hu, H. Lin, Y. Cheng, Q. Huang, J. Xu, Y. Gao, J. Wang, and Y. Wang, *J. Mater. Chem. C*, **5**, 10524 (2017).
330. Z. Wang, Z. Yang, Z. Yang, Q. Wei, Q. Zhou, L. Ma, and X. Wang, *Inorg. Chem.*, **58**, 456 (2019).
331. Z. Yang, Z. Yang, Q. Wei, Q. Zhou, and Z. Wang, *J. Lumin.*, **210**, 408 (2019).